EFFECT OF CASTING CONDITIONS AND CLOGGING ON FLUID FLOW IN METAL DELIVERY SYSTEM AND THERMO-MECHANICAL BEHAVIOR OF SOLIDIFYING SHELL IN CONTINUOUS CASTING OF STEEL

by

Hamed Olia

A thesis submitted to the Faculty and the Board of Trustees of the Colorado School of Mines in partial fulfillment of the requirements for the degree of Doctor of Philosophy (Mechanical Engineering).

Golden, Colorado

Date ______________________

Signed: ______________________

Hamed Olia

Signed: ______________________

Dr. Brian G. Thomas
Thesis Advisor

Golden, Colorado

Date ______________________

Signed: ______________________

Dr. Carl Frick
Professor and Department Head
Department of Mechanical Engineering

ABSTRACT

In continuous casting of steel, it is very important to quantify the pressure distribution and flow rate in the metal delivery system, which starts from the tundish, then into the Upper Tundish Nozzel (UTN), Submerged Entry Nozzle (SEN), and finally to the mold. It is, also, crucial to understand the effect of turbulent flow on thermo-mechanical characteristics of the solidifying shell inside the mold, since both can directly affect the quality of the final product.

To that end, two MATLAB-based state-of-the-art one-dimensional pressure energy models are developed and applied in this work to calculate pressure distribution and flow rate in slide-gate, PFSG, and stopper-rod nozzle systems, PFSR, for argon-molten steel flow systems by solving a 1D system of Bernoulli equations which can be used in commercial steel casters and water models. Both models are validated and verified with experimental plant measurements and computational fluid dynamics simulations with errors of less than 8 pct. Additionally, PFSG is used to investigate the effect of different casting conditions on the flow rate and pressure distribution. It is shown that increasing some casting conditions such as tundish height and nozzle bore diameter can decrease minimum pressure in the system, which in turn increases the possibility of air aspiration. As for the PFSR, it is concluded that two more phenomena, cavitation and non-primed flow, are needed to capture the real physics existing in the plant.

Finally, a transient thermo-mechanical model is developed to understand the strength of the turbulent flow on the solidifying shell inside the mold in continuous casting of steel using ABAQUS. The model is able to account for the superheat flux, which is the heat transfer across the interface near the solidification front between the turbulent flowing liquid and the solidifying steel shell. The predictions of the model include temperature distribution, shell growth, stress, and strain (including elastic, inelastic, thermal, and fluid components) distribution for temperature-varying thermo-mechanical and composition-based properties. It is, then, verified with existing models, CON1D and analytical solutions, and validated with experiments. Ultimately, a case study is conducted to investigate the effect of the turbulent flow caused by the asymmetric clogging inside one of the ports on the thermo-mechanical behavior of the solidifying shell inside the mold. It is shown that the effect of mold heat flux is far more important than the superheat flux.

TABLE OF CONTENTS

ABSTRACT . . . iii

LIST OF FIGURES . . . ix

LIST OF TABLES . . . xiii

ACKNOWLEDGMENTS . . . xiv

DEDICATION . . . xv

CHAPTER 1 INTRODUCTION . . . 1

CHAPTER 2 RESEARCH BACKGROUND . . . 3

2.1 Continuous Casting of Steel . . . 3

2.2 Clogging . . . 4

2.3 Solutions to Clogging . . . 5

2.4 Project Objectives . . . 5

CHAPTER 3 PRESSURE DISTRIBUTION AND FLOW RATE BEHAVIOR IN CONTINUOUS-CASTING SLIDE-GATE SYSTEMS: PFSG . . . 7

3.1 Introduction . . . 7

3.2 Model Description . . . 9

3.2.1 Pressure-Energy Model Equations . . . 10

3.2.2 Velocity and Area Calculations . . . 12

3.2.2.1 Effective Area Calculations . . . 12

3.2.2.2 Gap Area Calculation . . . 13

3.2.3 Pressure Losses . . . 13

3.2.3.1 Tundish Liquid Level to Tundish Floor (Points 1 to 2) . . . 14

3.2.3.2 Tundish Floor to UTN Region (Points 2 to 3) . . . 14

3.2.3.3 UTN Region (Points 3 to 4) . . . 15

3.2.3.4 Slide-gate Region (Points 4 to 5) . . . 16

3.2.3.5 Slide-gate to Upper SEN Region (Points 5 to 6) . . . 17

3.2.3.6 Lower SEN Tapered Region (Points 6 to 7) 18
3.2.3.7 Lower SEN To Port Region (Points 7 to 8) 18
3.2.3.8 Port Region (Points 8 to 9) 19
3.2.4 Incorporation of Clogging 19
3.2.5 Slide-gate Opening Definitions/Relations 20
3.2.5.1 Linear Slide-gate Opening 20
3.2.5.2 Plant (Offset) Linear Opening Fraction 21
3.2.5.3 Area Fraction 21
3.2.5.4 Center To Center Distance 21
3.2.5.5 Implementation 22
3.2.6 Model Solution Procedure 22
3.2.7 PFSG Inputs and Outputs 23
3.3 Model Verification and Validation 27
3.3.1 Verification of PFSG with CFD Simulations 27
3.3.2 Validation of PFSG with Inland Steel Plant Data 28
3.3.3 Verification and Validation of PFSG with Plant 2 Data 29
3.3.4 Verification and Validation of PFSG with Plant 3 Data 31
3.3.5 Verification and Validation of PFSG with Plant 4 Water Model Experimental Data . . . 31
3.4 Parametric Studies 32
3.4.1 Effect of Casting Conditions and Nozzle Geometry on Flow Rate 33
3.4.1.1 Effect of Slide-gate Opening 33
3.4.1.2 Effect of Argon Gas Injection 34
3.4.1.3 Effect of Diameter of Lower SEN 34
3.4.1.4 Effect of Tundish Height 35
3.4.1.5 Effect of Submergence Depth 36
3.4.2 Minimum Pressure Results 36
3.4.2.1 Effects of Tundish Height and Casting Speed 37

3.4.2.2 Effects of Submergence Depth and Casting Speed . . . 39
3.4.2.3 Effect of Nozzle Bore Diameter . . . 40
3.5 Conclusion . . . 41
CHAPTER 4 PRESSURE DISTRIBUTION AND FLOW RATE BEHAVIOR IN CONTINUOUS-CASTING STOPPER-ROD SYSTEMS: PFSR . . . 43
4.1 Introduction . . . 43
4.2 Model Description . . . 45
4.2.1 Pressure-Energy Model Equations . . . 46
4.2.2 Velocity and Area Calculations . . . 48
4.2.2.1 Effective Area Calculations . . . 48
4.2.2.2 Gap Area Calculation . . . 49
4.2.3 Pressure Losses . . . 53
4.2.3.1 Tundish Liquid Level to Tundish Floor (Points 1 to 2) . . . 53
4.2.3.2 Tundish Floor to Gap Region (Points 2 to 3) . . . 53
4.2.3.3 Gap Expansion Region (Points 3 to 4) . . . 54
4.2.3.4 UTN Region (Points 4 to 5) . . . 54
4.2.3.5 Upper SEN Region (Points 5 to 6) . . . 55
4.2.3.6 Lower SEN Tapered Region (Points 6 to 7) . . . 55
4.2.3.7 Lower SEN to Port Region (Points 7 to 8) . . . 56
4.2.3.8 Port Region (Points 8 to 9) . . . 56
4.2.4 Incorporation of Clogging . . . 57
4.2.5 Model Solution Procedure . . . 57
4.2.6 PFSR Inputs and Outputs . . . 57
4.3 Model Verification and Validation . . . 60
4.3.1 Verification of PFSR with CFD Simulations . . . 60
4.3.2 Verification and Validation of PFSR with Water Model 1 Data . . . 61
4.3.3 Validation of PFSR with Water Model 2 Data . . . 62
4.3.4 Verification of PFSR with Water Model 3 and Plant 3 Data . . . 63

4.4 Other Phenomena in Stopper-rod Flow . . . 66
4.4.1 Primed vs Non-Primed Flow . . . 66
4.4.2 Cavitation . . . 68
4.4.2.1 Solubility of Gases in Liquid Steel . . . 68
4.4.2.2 Variation of Gas/Steel Flow Rate with Pressure at Different Gas Contents . . 69
4.4.3 Non-primed Flow/Cavitation Methodology . . . 71
4.4.4 Solution procedure . . . 73
4.4.5 Application of Non-primed Flow/Cavitation Model . . . 73
4.5 Conclusion . . . 77
CHAPTER 5 THERMO-MECHANICAL BEHAVIOR OF SOLIDIFYING SHELL INSIDE THE MOLD AND THE EFFECT OF TURBULENT FLOW ON THE GROWTH . . . 79
5.1 Introduction . . . 79
5.2 Model Description . . . 81
5.2.1 Heat Transfer Model . . . 82
5.2.1.1 Specific Enthalpy and Heat Capacity . . . 82
5.2.1.2 Thermal Conductivity . . . 83
5.2.1.3 Density . . . 84
5.2.1.4 Thermal Linear Expansion . . . 85
5.2.2 Enhanced Latent Heat Method . . . 86
5.2.2.1 Latent Heat of Fusion Calculation . . . 87
5.2.2.2 Superheat Flux Calculation . . . 88
5.2.3 Fluid Flow Model . . . 88
5.2.3.1 Velocity and Temperature Contours . . . 89
5.2.3.2 Mold Interface and Superheat Flux . . . 90
5.2.4 Phase Fraction . . . 90
5.2.5 Stress Model . . . 91
5.2.5.1 Young's Modulus . . . 91
5.2.5.2 Constitutive Equations . . . 91

5.2.6 Solution Procedure 93

5.3 Model Verification and Validation 94

5.3.1 Weiner and Boley Verification Case 94

5.3.2 Verification Case 1 96

5.3.3 Verification Case 2 97

5.3.4 Validation Case 3 99

5.4 Case Study Investigating the Effect of Jet Impingement on Thermo-mechanical Behavior of the Shell 101

5.5 Conclusion 107

CHAPTER 6 SUMMARY AND FUTURE WORK 108

REFERENCES 110

APPENDIX A WALL FRICTION CALCULATION FOR TAPERED PIPE 117

APPENDIX B COPYRIGHT PERMISSIONS 119

LIST OF FIGURES

Figure 2.1 Schematic of continuous casting of steel 3

Figure 2.2 Two controlling system in continuous casting of steel (a) slide-gate (b) stopper-rod. 4

Figure 3.1 Example pressure distribution for all 10 points in a slide-gate metal delivery system (Nozzle 1 conditions). 11

Figure 3.2 PFSG V.3.2 user interface showing input data for Standard nozzle conditions. 23

Figure 3.3 Results for Standard nozzle (PFSG V.3.2) (a) pressure distribution (b) flow rate for different definitions of gate opening. 25

Figure 3.4 (a) Relationship between f_p, f_L, and f_A (b) geometrical relationship between parameters in calculating f_L and f_p for Standard nozzle ($D_{slide} = D_{USENa}$). 26

Figure 3.5 PFSG model validation with Inland Steel caster data for Standard nozzle casting conditions (a) flow rate (b) pressure distribution. 29

Figure 3.6 Pressure distributions verification of PFSG with CFD simulation for Nozzle 2 conditions at 57.85 pct f_L. 30

Figure 3.7 PFSG V.3.2 validation with Plant 2 data for Nozzle 2 casting conditions. 30

Figure 3.8 PFSG verification with Plant 3 Nozzle 3 using CFD simulations. 31

Figure 3.9 PFSG model validation with Plant 4 water model data for Nozzle 4 conditions (l_1: center line, l_2: line down front, l_3: line down side of nozzle bore). 32

Figure 3.10 Relation between tundish height, flow rate (casting speed), and slide-gate opening for Nozzle 1 conditions plotted for (a) different slide-gate openings (b) different casting speeds. 33

Figure 3.11 Effect of casting speed (flow rate) on argon injection rate relation with slide-gate opening for Nozzle 1 conditions. 34

Figure 3.12 Effect of diameter of lower SEN on flow rate (casting speed) relation with tundish height for Nozzle 1 conditions (constant 40 pct slide-gate opening). 35

Figure 3.13 Effect of tundish height on system flow rate relation with slide-gate opening for Nozzle 1 conditions, with (a) 6 SLPM argon gas injection (b) 0 argon gas injection. 36

Figure 3.14 Effect of nozzle submergence depth on relation between flow rate and slide-gate opening, for Nozzle 1 conditions. 37

Figure 3.15 Effect of tundish height on casting speed relation with (a) minimum gauge pressure and (b) slide-gate opening (Standard Nozzle conditions but with 75mm nozzle bore). 38

Figure 3.16 Effect of tundish height on casting speed relation with (a) minimum gauge pressure and (b) slide-gate opening (Standard Nozzle conditions but with 85mm nozzle bore). 38

Figure 3.17 Effect of tundish height on casting speed relation with (a) minimum gauge pressure and (b) slide-gate opening (Standard Nozzle conditions but with 90mm nozzle bore). . . . 39

Figure 3.18 Effect of nozzle submergence depth on variation of minimum pressure with (a) casting speed and (b) slide-gate opening. (Standard Nozzle conditions). 39

Figure 3.19 Effect of lower SEN diameter on slide-gate opening fraction at minimum pressure for Standard nozzle at various casting speeds, tundish heights, and submergence depths. . . . 40

Figure 3.20 Effect of diameter of lower SEN on minimum pressure (Standard nozzle). 41

Figure 4.1 Example pressure distribution for all 10 points in a stopper-rod metal delivery system (Nozzle 1 conditions). 47

Figure 4.2 Stopper-rod schematic showing parameters associated with general nozzle tip defined with 3 radii. 49

Figure 4.3 Geometrical relationship between stopper-rod and tundish floor circular segment at (a) fully closed (b) partially open position. 51

Figure 4.4 Stopper geometry showing minimum gap. 52

Figure 4.5 PFSR V.2.1 user interface showing input data for Nozzle 2 conditions. 59

Figure 4.6 Results for Nozzle 2 (PFSR V.2.1) (a) pressure distribution (b) flow rate. 60

Figure 4.7 Pressure distributions verification of PFSR with CFD simulation for Nozzle 1 conditions at 2.8 mm. 61

Figure 4.8 Pressure distribution validation of PFSR with measurements for Nozzle 1 conditions. . . . 62

Figure 4.9 Pressure distributions validation of PFSR with experimental measurements for Nozzle 2 conditions. 63

Figure 4.10 PFSR verification and validation with Nozzle 3 water model conditions. 64

Figure 4.11 PFSR verification with Nozzle 3 plant conditions (10 mm stopper opening). 65

Figure 4.12 PFSR flow prediction comparison with Plant 3, CFD simulation, and water model 3 measurements. 66

Figure 4.13 Schematic of (a) primed and (b) non-primed flow in stopper-rod systems. 67

Figure 4.14 Gas solubility in molten steel at different temperatures of (a) Nitrogen (b) Hydrogen . . . 69

Figure 4.15 Variation of the cavitated gas flow rate with the pressure at different total gas contents at 1550^{o}C for (a)nitrogen (b)hydrogen. 71

Figure 4.16 Schematic of the non-primed flow methodology. 72

Figure 4.17 Pressure distribution for different openings using non-primed flow/cavitation methodology (PFSR V.3.0 Nozzle 3 conditions). 74

Figure 4.18 Flow rate-stopper-rod relation prediction of non-primed/cavitation methodology -Nozzle 3. 75

Figure 4.19 Pressure distribution comparison of different solutions for [1 mm stopper-rod opening, 0.28 tonne/min flow rate] using non-primed/cavitation flow methodology (PFSR V.3.0) -Nozzle 4 conditions. 75

Figure 4.20 Pressure distribution comparison for different stopper-rod openings using non-primed/cavitation Flow methodology (PFSR V.3.0) -Nozzle 4. 76

Figure 4.21 Flow rate-stopper-rod relation validation non-primed/cavitation methodology (PFSR V.3.0) -Nozzle 4. 76

Figure 5.1 Thin slice of solidifying steel representing the simulation domain. 81

Figure 5.2 Variation of the specific enthalpy with temperature for low carbon (0.045 pct) steel. . . . 83

Figure 5.3 Variation of the thermal conductivity with temperature for low carbon (0.045 pct) steel. . 84

Figure 5.4 Variation of the steel density with temperature for low carbon (0.045 pct) steel. 85

Figure 5.5 Variation of the steel TLE with temperature for low carbon (0.045 pct) steel. 86

Figure 5.6 CFD simulation results, contours of a) velocity and b) temperature 89

Figure 5.7 Prescribed a) interface heat flux and b) superheat flux for case study 90

Figure 5.8 Variation of the phase fraction with temperature for low carbon (0.045 pct) steel. 90

Figure 5.9 Variation of Young's modulus with temperature for steel. 91

Figure 5.10 Stress-inelastic strain relation with temperature for low carbon content (0.045 pct) steel. . 92

Figure 5.11 Verification domain with thermal and mechanical BC's 95

Figure 5.12 Verification of the model with analytical solution at different times of solidification for (a) Temperature (b) Hoop Stress. 95

Figure 5.13 Verification case 1 meshed domain. 96

Figure 5.14 Temperature distribution comparison for verification case 1. 97

Figure 5.15 Verification case 2 meshed domain. 97

Figure 5.16 Verification case 2 prescribed mold heat flux and superheat flux variation with distance below meniscus. 98

Figure 5.17 Shell thickness comparison for verification case 2. 98

Figure 5.18 Temperature and hoop stress distribution comparison for verification case 2. 99

Figure 5.19 Validation case 3 meshed domain. 99

Figure 5.20 Validation case 3 prescribed heat flux and superheat flux variation with distance below meniscus. 100

Figure 5.21 Validation case 3 temperature distribution comparison. 100

Figure 5.22 Validation case 3 hoop stress distribution comparison. 101

Figure 5.23 Comparison of shell thickness prediction of CON1D with ELH method for the case study. 102

Figure 5.24 Temperature distributions at different times (before, during and after maximum jet impact). 103

Figure 5.25 Hoop stress distributions at different times (before, during and after maximum jet impact). 104

Figure 5.26 Hoop stress contours of the solidifying shell for different cases. 105

Figure 5.27 Surface profile of hoop stress and inelastic strain through time below meniscus. 106

Figure 5.28 Surface profile of elastic and thermal strain through time below meniscus. 107

Figure A.1 Schematic of tapered length of nozzle (pipe). 117

Figure B.1 Permission obtained for PFSG paper. 119

LIST OF TABLES

Table 3.1 Nozzle dimensions and plant casting conditions studied in this chapter 24

Table 4.1 Nozzle dimensions and plant casting conditions studied in this chapter 58

Table 5.1 Simulation conditions and material properties for the verification and validation cases . . . 94

Table 5.2 Conditions and material properties for the verification and validation cases 102

Table 5.3 Four possible cases to study the combined effect of mold and superheat flux 104

ACKNOWLEDGMENTS

First and foremost, I would like to thank my advisor Prof. Brian Thomas, for trusting me and giving me the opportunity and supporting me in all the possible ways, even the times I was wrong, and letting me to not only make mistakes but also learn from them through this amazing journey.

Additionally, I want to graciously acknowledge the financial and technical support I received from the members of the Continuous Casting Center, CCC, at the Colorado School of Mines, which have included: AK Steel, ANSYS-Fluent, Baosteel, Nucor, RHI Magnesita Refractories, ArcelorMittal, SSAB, POSTECH/POSCO, and TATA Steel. I would also like to thank the Department of Mechanical Engineering at Colorado School of Mines for financial support in the form of graduate teaching fellowships. Over the years, this work was additionally supported by the grants provided from the National Science Foundation GOALI Program (Grant Number: CMMI 18-08731), at Colorado School of Mines.

Through my PhD, I have had the honor and the privilege to work and collaborate with many brilliant researchers, scientists, and engineers around the world: Dr. Hyunjin Yang of SWERIM AB, Dirk van der Plas of TATA Steel Europe, Richard Gass and Dr. Rui Liu of ArcelorMittal, Dr. Ken Morales and Alexandre Dolabella Resende of RHI Magnesita, Dr. Xiaoming Ruan of Baosteel, and Dr. Shin-Eon Kang of POSCO. All of the support, discussion, code testings, and experimental data you have kindly provided allowed me to complete the work I needed to.

Research is truly a team effort and I would like to thank some of the other students, visiting scholars, and researchers of the CCC that I have had the pleasure to work with over the past few years: Mingyi Liang, Lipsa Das, Ghavam Azizi, Dylan Palmer, Ehsan Jebellat, Dr. Zhelin Chen, Prof. Guoming Zhu, and Carly Blaes. I would like to especially thank Dr. Matthew Zappulla and Dr. Seong-Mook Cho, for many shared meals, pints of advice, code testing, and mentorship to my project.

Last but not least, tremendous thanks are due to my beloved wife, Romina Fasihi Dolatabadi, parents, and family for constant support and help in making this experience as comfortable as possible in the last few years.

To my best friend, companion, and wife, Romina.

CHAPTER 1

INTRODUCTION

This work is divided into three modeling chapters (3 through 5), preceded by this introduction and the following background chapter (2), and succeeded by a summary and future work chapter (6). Chapter 2 generally deals with a brief background on the continuous casting process, relevant phenomena, and further motivation for this research topic.

Chapter 3 provides a thorough description of the first model developed by the author and used in this work including verification, validation, and parametric studies. This chapter includes the content of the article published online by Metallurgical and Materials Transactions B Journal in March 2022. The journal paper first introduces the model calculating pressure distribution and flow rate in slide-gate flow delivery systems in continuous casting of steel. Afterward, it is validated against experimental flow rate and pressure measurements for the different plant data. The measurements used in this work were taken at ArcelorMittal, Baosteel, and POSCO steel companies and compiled by Dr. Tatha Bhattacharya, Dr. Xiaoming Ruan, and Dr. Shin-Eon Kang, respectively. The model is, also, verified using CFD simulations conducted by Mingyi Liang, Lipsa Das, and Dr. Seong-Mook Cho (all advised by Prof. Brian Thomas). Finally, parametric studies are conducted to study the effect of different casting conditions on the flow rate and pressure distribution.

Chapter 4 explores description of the second model developed by the author and used in this work including its verification and validation. This chapter contains the content of the article to be submitted to Metallurgical and Materials Transactions B Journal in July 2022. Similar to the previous chapter, a model is introduced to calculate pressure distribution and flow rate in stopper-rod flow delivery systems in continuous casting of steel. Additionally, it is validated against experimental flow rate and pressure measurements for the different plant data. The measurements used in this work were taken at ArcelorMittal and TATA steel companies as well as at Colorado School of Mines water model and were given to the author by Mingyi Liang, Dr. Rui Liu, Dirk van der Plas, and Dustin Salley. The model is verified using CFD simulations conducted by Mingyi Liang and Dr. Rui Liu.

Chapter 5 addresses the third model developed by the author, dealing with the thermo-mechanical behavior of the solidifying shell inside the mold in continuous casting of steel, containing the content of the article to be submitted to Journal of Materials Processing Technology in July 2022. In this chapter, a transient model is developed, which is able to include the effect of low and high-velocity jet of the turbulent flow on thermo-mechanical behavior of solidifying shell inside the mold in the continuous casting of steel. After developing the model, it is verified with CON1D and the existing analytical solutions of thermo-mechanical behavior of solidifying shell, and validated by plant experiments. Finally, a case study is conducted to investigate the effect of the turbulent flow passing through both clogged and non-clogged ports on the thermo-mechanical behavior of the solidifying shell inside the mold. The plant experiments of asymmetrical clogging used in this chapter were conducted at POSCO and include the mold heat flux measurements. Then, a calibration study was conducted using CON1D by Dr. Seong-Mook Cho to calculate the corresponding cold and hot heat fluxes that match with the measurements of the plant. Using this information, and applying CFD (done in ANSYS Fluent), Dr. Seong-Mook Cho calculated the superheat flux which is the heat transfer across the interface near the solidification front between the turbulent flowing liquid and the solidifying steel shell. Both clogged and non-clogged hot mold heat flux and superheat flux were input to the thermo-mechanical model.

The three models developed in this work are connected as follows: Chapters 3 and 4 provide tools to predict the effect of different casting conditions (as well as possible clogging) on pressure and flow, and Chapter 5 shows the effect of the flow, caused by the extreme case of clogging, on thermo-mechanical behavior of the solidifying shell inside the mold.

Finally, Chapter 6 provides a summary and conclusions of the thesis as well as the future work and improvements to existing models.

CHAPTER 2

RESEARCH BACKGROUND

In this chapter, an introduction to continuous casting of steel and its associated phenomena as well as the project objectives and the structure of each chapter are discussed.

2.1 Continuous Casting of Steel

Continuous casting of steel is the most popular way of steel mass production in steel industry. In fact, most of the steel produced in the US (96%) and the world (95%) is made by continuous casting [1]. In the continuous casting as shown in Figure 2.1, steel from the ladle flows through the tundish, exits to the Upper Tundish Nozzle (UTN), goes down through a ceramic Submerged Entry Nozzle (SEN), and through the ports flows into the mold. Inside the mold, the steel freezes against the water-cooled copper walls to form a thin solid shell which is continuously withdrawn from the bottom of the mold at a fixed casting speed after which it is quenched down using cool water spray until it is completely solidified and cut to slabs at the end of the process.

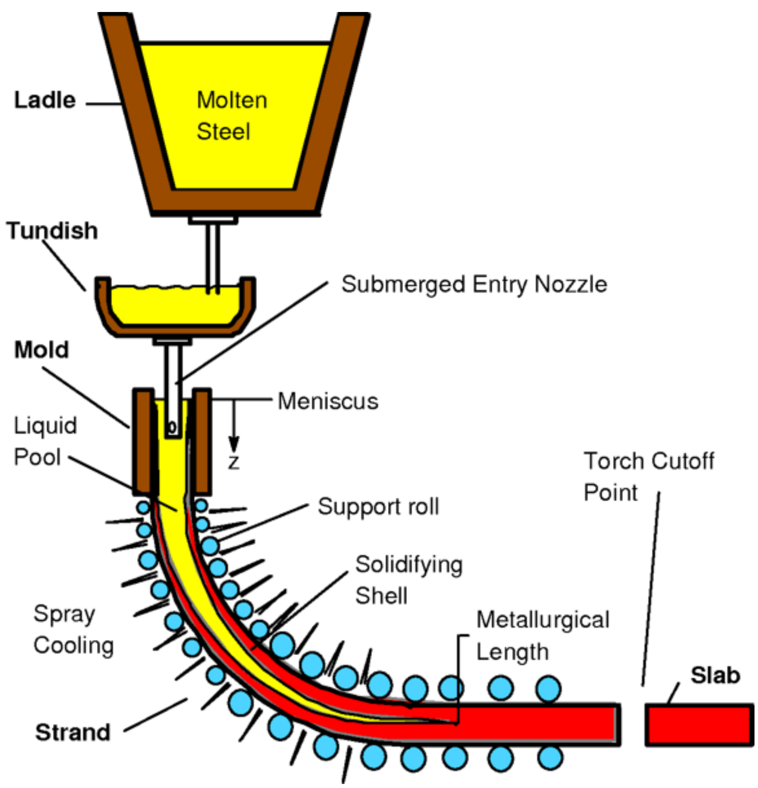

Figure 2.1 Schematic of continuous casting of steel [2].

According to Figure 2.2, the flow inside the nozzle is gravity driven. The flow rate is also controlled by one of two different controlling mechanisms. It is restricted by either a slide-gate in which a sliding plate connecting the UTN to SEN moves, Figure 2.2(a), or is controlled by the vertical displacement of a rod extending from the bottom of the tundish floor up to the UTN, Figure 2.2(b).

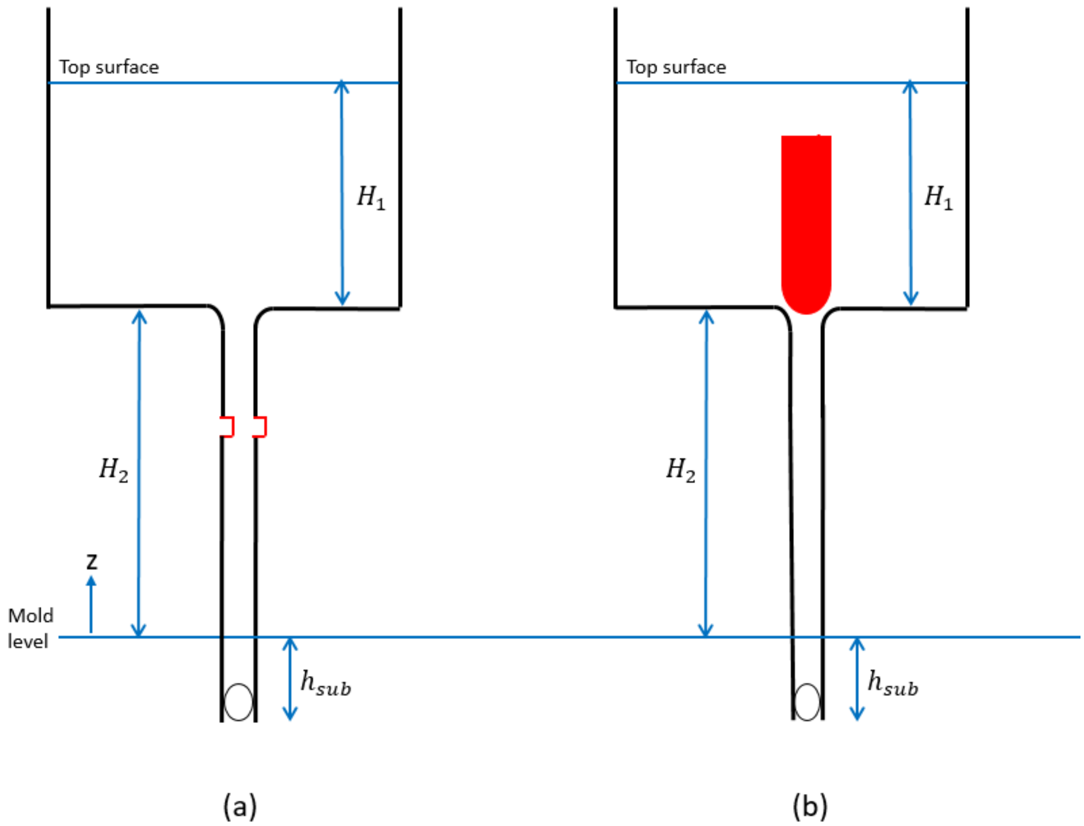

Figure 2.2 Two controlling system in continuous casting of steel (a) slide-gate (b) stopper-rod.

2.2 Clogging

One of the important functions of SEN is protecting the molten steel against air exposure and the further re-oxidation leading to inclusion formation. In spite that, it is always possible the air is sucked into the system by air aspiration [3]. If the pressure decreases to the values lower than atmospheric pressure through the porous refractory, cracks, joints, or possible leakage, it might cause the formation of the build up called clogging [3–6]. The susceptible location through which air aspiration might happen are near joints and/or cracks, the entrance of UTN, or the top of the port outlet [3–5]. The clogging specifically can alter the geometry of the nozzle walls through the reaction of oxygen and nitrogen with the dissolved alloy elements in molten steel and forming inclusions adhered to nozzle wall. It can also change the flow pattern, especially inside mold causing level fluctuation, slag entrapment, hooks, and shell thinning [7]. More specifically clogging in the port can lead to lower surface velocity, causing the temperature decrease which ultimately can cause the meniscus to freeze [8] or excessive surface velocity, causing level fluctuations and slag entrainment. Furthermore, it is important to note that flow while passing through clogging experience sudden contraction and expansion which is related to the geometry of the clogging [3]. This intensifies the importance of the clogging shape, meaning that even if the clogging shape is changed very little, it takes longer for the flow control system to adjust itself, during which the clogging also has changed and the control system has failed to adjust itself further [3]. This means that the flow control system lags behind the flow rate changes, resulting in flow rate variations which cause transient level fluctuations in the mold without the control system is able to adjust the opening to keep it fixed. Also, clogging could make the control system sticker (not move smoothly), which is more important in slide-gate control system rather than stopper-rod. Additionally, it is very important to know that clogging could be detrimental to the system maintenance, since it increases the frequency of the nozzle change [6, 9]. Finally, it can cause even larger particle formation leading to lower quality product by being entrapped in the final steel as inclusion defects [10–12].

2.3 Solutions to Clogging

There are a couple of ways to reduce the possibility of clogging formation in the system such as modifying the nozzle geometry by improving joint sealing [13], using oversized nozzle bores to enable longer casting even while clogging builds up on the nozzle walls [14, 15], or nozzle with varying diameter [16, 17], or employing calcium treatment to reduce alumina-type clogging [18–22]. Last but not least and probably the most common practice is to add argon into the system through stopper-rod tip, UTN, or other places inside the nozzle to be aspired instead of air and reduce clogging which is discussed elsewhere [3, 4, 6]. All of these ways to mitigate clogging also have a strong effect themselves on the flow and pressure. Therefore, it is of high importance to quantify the pressure distribution, specifically the minimum pressure, and the system flow rate to predict when and where the clogging happens to avoid it. Also, it is very crucial to know what happens to the solidifying shell when clogging happens in the system especially in the port.

2.4 Project Objectives

According to what is introduced above, the objectives of this thesis are as follows:

- Develop, verify, and validate simple models/computer programs to calculate pressure distribution and flow rate in slide-gate control system, PFSG, and stopper-rod control system, PFSR (discussed in chapters 3 and 4).

- Develop, verify, and validate a model to calculate the effect of superheat flux for a real steel alloy, including properties that depend on temperature and composition, on thermo-mechanical behavior of solidifying shell inside the mold (discussed in chapter 5).
- Finally, apply these models to investigate the effect of different casting conditions and clogging on pressure distribution and flow rate in metal delivery systems, and thermo-mechanical behavior of solidifying shell inside a mold (discussed in chapters 3, 4, and 5).

CHAPTER 3

PRESSURE DISTRIBUTION AND FLOW RATE BEHAVIOR IN CONTINUOUS-CASTING SLIDE-GATE SYSTEMS: PFSG

Modified from a paper published in The Journal of Metallurgical and Materials Transactions B[1].

Hamed Olia[2,3], Hyunjin Yang[4,5], Seong-Mook Cho[6,5],Mingyi Liang[2,5],Lipsa Das[2,5], B. G. Thomas[7,8]

Quantifying the pressure distribution and flow rate in the metal delivery system from the tundish to the mold is important to understand nozzle clogging due to air aspiration, argon bubble size, and other important phenomena in continuous casting of steel. A one-dimensional pressure energy model, PFSG, is presented here to calculate pressure distribution and flow rate in slide-gate nozzle systems for argon-molten steel flow systems including argon gas expansion by solving a system of Bernoulli equations. PFSG is a user-friendly MATLAB-based software package with an intuitive Graphical User Interface capable of inverse solutions that enables users to conduct parametric studies in seconds. The model predictions are verified with computational fluid dynamics simulations and validated with plant measurements and water model measurements, with errors of less than 6 pct. The verified and validated PFSG model is then applied to investigate the effect of different casting conditions on the flow rate and pressure distribution. For a given slide gate opening, the flow rate increases with increasing distance from the tundish level to the mold level, increasing SEN diameter, and decreasing argon gas injection rate. The slide-gate opening fraction that produces the minimum pressure is almost independent of casting conditions, except for SEN bore diameter. This critical opening fraction, which is most detrimental for air aspiration, increases from 50 to 70 pct with increasing SEN diameter by 13 pct for the system studied. The minimum pressure worsens (decreases) with increasing tundish height and/or nozzle bore diameter.

3.1 Introduction

Pressure distribution in continuous casting flow control systems from the tundish into the upper tundish nozzle (UTN), past the slide-gate flow control, into the submerged entry nozzle (SEN), through the ports and finally up to the top surface in the mold is important for many reasons. Firstly, it governs the

[1]Reprinted with permission of J. of Metallurgical and Materials Transactions B, 53, 1661–1680.
[2]Graduate student at the Colorado School of Mines
[3]Primary researcher and author
[4]Researcher in Process Metallurgy Department, SWERIM AB
[5]Author
[6]Assistant Professor at Department of Metallurgical Engineering, Pukyong National University
[7]Full Professor at the Colorado School of Mines
[8]Author for correspondence

flow rate (and corresponding casting speed) in this gravity-driven process. Secondly, it is crucial to the minimum pressure beneath the slide-gate, where air aspiration, re-oxidation, and nozzle clogging may occur [3, 4]. When pressure inside the nozzle drops below atmospheric pressure, air may be drawn into the nozzle through any cracks, leaks at joints, or permeable gas flow through the porous refractory. [3–5]. The oxygen and nitrogen can react with dissolved alloy elements in the molten steel to form oxide and nitride inclusions, which may adhere to the nozzle walls as clogging, or become entrained into the final product as inclusion defects [6, 9].

Clogging may occur at different places inside the nozzle, depending on the formation mechanism [3, 5, 6]. Air aspiration tends to cause clogging near joints or cracks in the refractory walls, while flow separation leads to clogging due to exogenous inclusion buildup below the slide-gate and top of the port outlets [3–5]. Clogging is detrimental because 1) it alters the effective nozzle geometry, decreasing the cross-sectional area, thus requiring more frequent nozzle replacement [6, 9] 2) it agglomerates inclusions into larger, more detrimental particles if the clog partially breaks away, and 3) it causes flow variations, leading to more severe level fluctuations in the mold, and 4) it causes flow variations, leading to more severe level fluctuations in the mold [7], which ultimately increases sliver defects in the final product [10–12].

For these reasons, it is beneficial to minimize pressure drops below atmospheric pressure inside the nozzle. An alternative suggestion to reduce air aspiration is to surround the slide-gate with a vacuum chamber [23], but this is not feasible in practice. A common commercial practice is to introduce argon into the slide-gate region, in order to encourage the aspiration of argon instead of air or to actively inject argon gas. Argon may act in several ways to lessen clogging, which are reviewed elsewhere. [3, 4, 6]. Finally, the most important and least expensive method to minimize re-oxidation from pressure drops is to optimize the nozzle geometry [9] according to the casting conditions, such as tundish height, casting speed, slide-gate opening, and argon gas injection rate.

Only a few previous studies using validated models have been undertaken to understand the pressure distribution in a slide-gate flow control system as a function of the system geometry and casting conditions. These models employed a Bernoulli energy-balance approach [6, 24, 25], computational fluid dynamics (CFD) models [26, 27] or a curve fit of polynomial functions [3]. The results indicated that the combined effects of fluid control systems (slide-gate opening or stopper-rod opening), casting speed, nozzle geometry (nozzle length and diameter), argon gas injection, tundish height (depth or level of molten steel inside tundish) are required to calculate the pressure distribution as well as system flow rate. Bai et al. [3] found that a near-vacuum situation might appear in the slide-gate region for small slide-gate opening. They found that injection of argon gas can alleviate the negative pressure problem, and quantified how much argon is needed for different nozzle diameters and casting conditions. For most conditions, the required argon is unfeasibly high.

Liu and Thomas proposed a 1D analytical model, based on the Bernoulli energy-balance approach, to relate stopper-rod position and flow rate [25]. Their parametric studies quantify how system flow rate changes with increasing clogging and eventually requires the to open further to maintain the flow rate. Recently, Yang et al. [4] improved this analytical approach to quantify pressure distribution and flow rate in slide-gate metal delivery system. Pressure distributions were shown for different SEN diameters for a typical slab casting operation, assuming in-compressible flow. Decreasing SEN diameter was shown to lessen the problem of negative pressure for a given casting speed and argon gas flow rate. Many previous computational models of multi-phase flow in continuous casting of steel have been developed and applied to investigate fluid flow in the nozzle [27, 28] and/or mold/strand [29–31], including the effect of argon gas injection, which are reviewed elsewhere [32, 33]. The few that show pressure distributions [3, 4, 26, 27, 34–36] confirm that pressure in the gap region in both slide-gate [3, 4, 27, 34–36] and stopper-rod [26, 36] flow control systems can easily drop below atmospheric pressure. However, parametric studies are limited and no previous model has considered the effect of compressibility of the argon gas on flow and pressure inside the nozzle even though this effect has been shown to be very important in closely-related systems [37, 38].

The present chapter introduces a new computationally-efficient modeling package for calculating Pressure distribution and Flow rate within slide-gate flow delivery systems: PFSG. This software package improves on the model developed by Yang et al. [4], and features a user-friendly Graphical User Interface (GUI) with other enhancements, such as inverse-modeling capabilities, non-circular nozzle cross sections, and clogging resistances which vary with location. PFSG also includes the effect of gas compressibility, which varies the argon flow rate locally, due to pressure variations in the flow system. Parametric studies are conducted with PFSG to investigate the combined effects of tundish height, SEN submergence depth, casting speed, gas injection rate, and nozzle geometry on slide-gate opening, flow rate, and pressure distribution in the nozzle.

3.2 Model Description

A new model based on the Bernoulli energy-balance approach, PFSG, has been developed to calculate pressure distribution and flow rate in slide-gate flow-control systems for continuous casting of steel slabs. The program features a user-friendly graphical interface and is already in use at several steel plants. The PFSG model calculates flow and pressure, starting in the tundish, through the UTN, slide-gate plates, SEN, and ending at the top surface level in the mold. Pressure is calculated at different points in the metal delivery system as a function of geometry and process conditions, including the flow rate, slide-gate opening, argon gas injection rate, fluid density, UTN and SEN absolute roughness, and possible clogging. The model equations are solved with MATLAB [39] and are presented in the next section, followed by a description of the inputs and outputs.

3.2.1 Pressure-Energy Model Equations

The PFSG model solves a one-dimensional system of pressure-energy balance equations for fluid flow, including kinetic energy, potential energy, and turbulent dissipation pressure/energy losses, based on a Bernoulli approach [4]. General analytical expressions are obtained for the pressure/energy loss between 10 selected points distributed vertically in the slide-gate system (Figure 3.1 in page 11), which follow the main streamline of molten steel flow from the tundish top surface through the UTN, slide-gate, SEN, ports, and to the mold level [4]. Pressure is calculated at each point in the system by:

$$P_x = P_{x+1} + \rho_m g h_{x+1} - \rho_m g h_x + \frac{1}{2}\rho_m V_{x+1}^2 - \frac{1}{2}\rho_m V_x^2 + \sum \Delta P_L \tag{3.1}$$

where P_x is gauge pressure of point x $[Pa]$,ρ_m is mixture fluid density $[\frac{kg}{m^3}]$, V_x is velocity at point $x[\frac{m}{s}]$, h_x is the height associated with point x $[m]$, and g is gravitational acceleration $[9.81\frac{m}{s^2}]$. With this form of the equation, the velocities must be calculated first from the system flow rate. Boundary conditions of 1 atm pressure are applied at the top surfaces of the tundish and the mold level, Finally, the pressure energy loss terms,$\sum \Delta P_L$, $[Pa]$ are explained in section 3.2.3, and depend on the geometric details between each pair of points.

Applying Equation 3.1 to the ten points in the continuous casting system shown in Figure 3.1 yields to the following ten equations:

$$P_1 = P_2 - \rho_L g h_{1-2} \tag{3.2}$$

$$P_2 = P_3 + \frac{1}{2}\rho_m V_{UTNa}^2 + \Delta P_{L,tun} + \Delta P_{L,two} \tag{3.3}$$

$$P_3 = P_4 - \rho_m g h_{3-4} - \frac{1}{2}\rho_m V_{UTNa}^2 + \frac{1}{2}\rho_m V_p^2 + \Delta P_{Lf,3-4} + \Delta P_{L,UTN} + \Delta P_{L,up} \tag{3.4}$$

$$P_4 = P_5 - \rho_m g h_{4-5} - \frac{1}{2}\rho_m V_p^2 + \frac{1}{2}\rho_m (\gamma V_{gap})^2 + \Delta P_{Lf,4-5} + \Delta P_{C,sg} + \Delta P_{L,sg} + \Delta P_{L,gate1} \tag{3.5}$$

$$P_5 = P_6 - \rho_m g h_{5-6} - \frac{1}{2}\rho_m (\gamma V_{gap})^2 + \frac{1}{2}\rho_m (\chi V_6)^2 + \Delta P_{Lf,5-6} + \Delta P_{L,USEN} + \Delta P_{L,gate2} + \Delta P_{L,P_2} \tag{3.6}$$

$$P_6 = P_7 - \rho_m g h_{6-7} - \frac{1}{2}\rho_m(\chi V_6)^2 + \frac{1}{2}\rho_m V_{SEN}^2 + \Delta P_{Lf,6-7} + \Delta P_{L,tap} \tag{3.7}$$

$$P_7 = P_8 - \rho_m g h_{7-8} + \Delta P_{Lf,7-8} \tag{3.8}$$

$$P_8 = P_9 - \frac{1}{2}\rho_m V_{SEN}^2 + \frac{1}{2}\rho_m V_{port}^2 + \Delta P_{L,port} + \Delta P_{L,tee} + \Delta P_{C,port} \tag{3.9}$$

$$P_9 = \rho_L g h_{sub} \tag{3.10}$$

$$P_{10} = P_{atm} = 0 \tag{3.11}$$

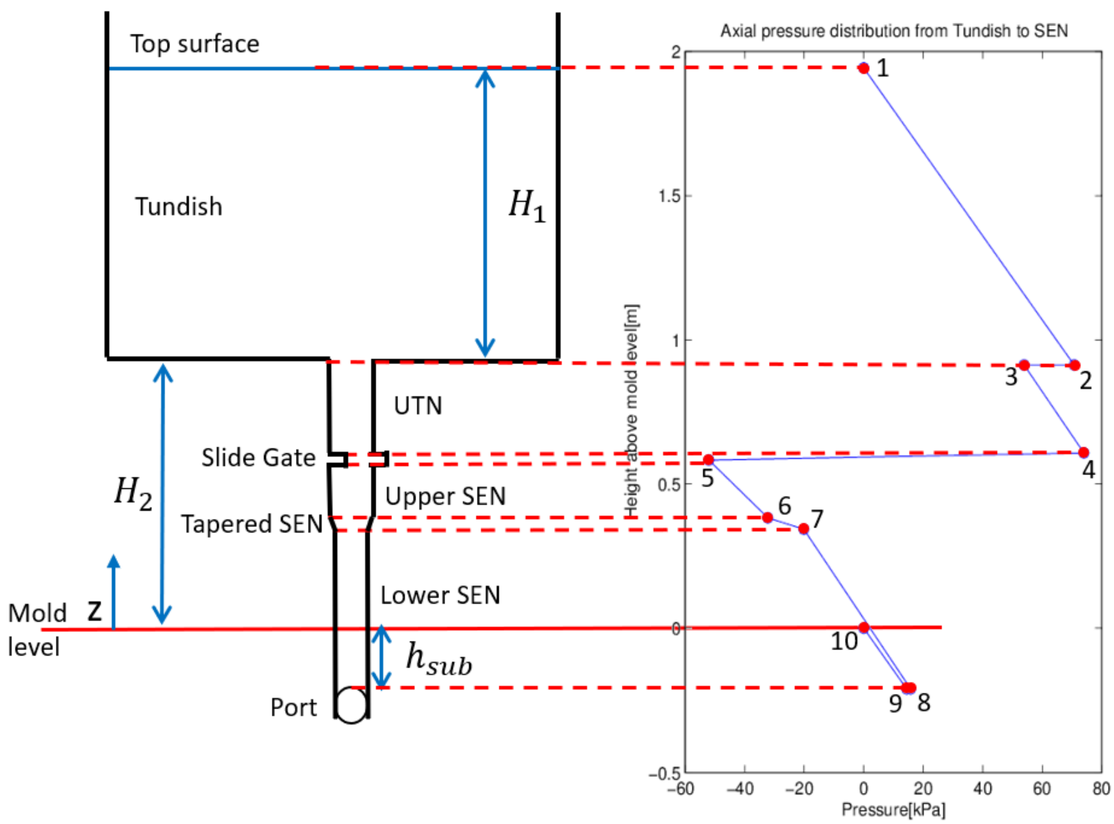

Figure 3.1 Example pressure distribution for all 10 points in a slide-gate metal delivery system (Nozzle 1 conditions).

Most of these equations are given by Yang et al.[4], but several terms include new improvements.

3.2.2 Velocity and Area Calculations

Velocity at each point in the PFSG model, V_x, $[\frac{m}{s}]$ is calculated from the system flow rate as follows:

$$V_x = \frac{Q}{A_{eff,x}} \tag{3.12}$$

where Q is the liquid (water or steel) flow rate $[\frac{m^3}{s}]$, and $A_{eff,x}$ is the effective area of the local cross section $[m^2]$ considering air or argon gas injection, as discussed in the next section.

3.2.2.1 Effective Area Calculations

With no argon gas injection, A_x is the area of the cross section of the nozzle at any given point (x) in the model $[m^2]$. However, if argon gas is injected, then it will limit the effective area for molten steel flow according to its volume fraction, α_x, which varies with vertical position in the model system according to:

$$\alpha_x = 1 - \frac{Q}{Q_{gas,x} + Q} \tag{3.13}$$

where $Q_{gas,x}$ is the flow rate of the "hot" (i.e. at molten steel temperature, $T_{hot} = 1823K$) argon gas at point $x[\frac{m^3}{s}]$ and is calculated as follows:

$$Q_{gas,x} = SLPM \times \frac{P_{atm}}{P_{atm} + (\frac{P_{x+1}+P_x}{2})} \times \frac{T_{hot}}{T_\infty} \times \frac{0.001}{60} \tag{3.14}$$

where $SLPM$ is the flow rate of the "cold" (i.e. at ambient temperature $T_\infty = 298K$) argon gas injected in standard liters per minute, P_{atm} is the standard (atmospheric) pressure 101 kPa, and P_{x+1} is gauge pressure at point $x+1[kPa]$ (previously calculated downstream pressure). Therefore, the effective cross-section area for steel flow, $A_{eff,x}$, and the mixture density between two points are expressed as:

$$A_{eff,x} = A_x \times (1 - \alpha_x) \tag{3.15}$$

$$\rho_m = \rho_L \times (1 - \alpha_x) \tag{3.16}$$

where A_x is the cross-section area at point x, according to the nozzle geometry $[m^2]$ and ρ_L is liquid density x $[\frac{kg}{m^3}]$.

For the UTN entry, UTN exit, upper plate, middle plate, and lower plate, the cross section is considered to be circular, which can be calculated as follows:

$$A_x = \frac{\pi}{4} D_x^2 \tag{3.17}$$

where D_x is the diameter of that portion of the nozzle, x $[m]$. At other vertical locations down the nozzle system, the area and perimeter are required inputs to define the geometry for more generality, and are used to calculate the equivalent hydraulic diameter, $D_{h,x}$, $[m]$ as follows:

$$D_{h,x} = \frac{4A_x}{p_x} \tag{3.18}$$

where p_x is the perimeter of portion x $[m]$. Furthermore, for a bifurcated port, if the port area is greater than half of the SEN area, it is set back down to half of the SEN area, because the jet exiting the port cannot expand fast enough to change its area significantly, so the rest of the area, in the upper port, typically has negligible net outward flow [3, 4].

3.2.2.2 Gap Area Calculation

The minimum cross-section area of the gap formed in the slide-gate region, A_{gap}, $[m^2]$ is calculated as follows [40]:

$$A_{gap} = R_1^2 \arccos(\frac{R_1^2 - R_2^2 + d^2}{2R_1 d}) + R_2^2 \arccos(\frac{R_2^2 - R_1^2 + d^2}{2R_2 d}) - d\sqrt{\frac{4R_1^2 d^2 - (R_1^2 - R_2^2 + d^2)^2}{4d^2}} \tag{3.19}$$

In which:

$$D = min(D_{slide}, D_p) \tag{3.20}$$

$$d = \frac{D_{slide} + D_p}{2} - Df_L \tag{3.21}$$

$$R_1 = \frac{max(D_{slide}, D_p)}{2} \tag{3.22}$$

$$R_2 = \frac{min(D_{slide}, D_p)}{2} \tag{3.23}$$

where D_{slide} is the diameter of the sliding middle plate hole, D_p is the diameter of the lower/upper fixed plates of the slide-gate in $[m]$, and f_L is the linear slide-gate opening fraction. Note that the lower and upper plates are assumed to have the same diameter.

3.2.3 Pressure Losses

The PFSG model incorporates pressure loss terms, $\sum \Delta P_L$ in Equation 3.1, between each pair of points in the system in Figure 3.1.

3.2.3.1 Tundish Liquid Level to Tundish Floor (Points 1 to 2)

The top of the liquid level in the tundish is at atmospheric pressure, so P_1 is zero gauge pressure. This is the top boundary condition for the 1-D model. Between point 1 and the tundish floor exit to UTN (point 2) velocity is negligible and there are no pressure losses, so Equation 3.1 simplifies to the potential energy term for the classic hydrostatic pressure gain:

$$P_2 = \rho_L g(h_1 - h_2) \tag{3.24}$$

This equation is also used between points 9 and 10, by replacing $(h_1 - h_2)$ with $(h_9 - h_{10})$. Similarly, the liquid level in the mold is at atmospheric pressure which defines the bottom boundary condition of the model ($P_{10} = 0$).

3.2.3.2 Tundish Floor to UTN Region (Points 2 to 3)

When flow exits the tundish bottom into the UTN, it experiences a sudden contraction in area which causes a pressure loss that depends on the decrease in area, $P_{L,tun}$, $[Pa]$ and is expressed as [41]:

$$\Delta P_{L,tun} = \frac{1}{2}\rho_m V_{UTNr}^2 (0.42(1 - \frac{n \times A_{UTNr}}{A_{tun}})) \tag{3.25}$$

where V_{UTNr} is fluid velocity just before UTN entry [m/s], A_{UTNr} is upper UTN surface area $[m^2]$ in contact with tundish floor with curvature radius of $r[m]$, A_{tun} is area of the tundish bottom $[m^2]$, and n is the number of nozzles where flow exits the tundish bottom.

Additionally, $\Delta P_{L,two}$ is considered to account for the pressure drop caused by possible argon gas injection [4]:

$$\Delta P_{L,two} = \frac{1}{2}\rho_m V_{UTNa}^2 T \tag{3.26}$$

Where V_{UTNa} is fluid velocity at UTN entry $[\frac{m}{s}]$. The pressure loss caused by the argon gas injection, T, is calculated based on the argon gas volume needed to be displaced to overcome the buoyancy effect, Vol_{gas}, in order to account for argon flow inside the nozzle. This constant is calculated as:

$$T = \frac{2gVol_{gas}}{A_{UTNa}(V_{UTNa}^2)} \tag{3.27}$$

where A_{UTNa} is the area of the UTN inlet, and Vol_{gas} is defined as:

$$Vol_{gas} = \sum Vol_x \alpha_x \tag{3.28}$$

where Vol_x is the volume of the specific nozzle region (for example UTN). It should be noted that if argon gas is injected into the UTN, then all of the argon volume and gas fraction from the UTN up to the end of the lower SEN must be calculated and summed together to find Vol_x.

3.2.3.3 UTN Region (Points 3 to 4)

In this potentially tapered region, there are three pressure losses to sum between the top of the UTN and the upper plate at the bottom of the UTN, points 3 and 4: $\Delta P_{Lf,3-4}$, $\Delta P_{L,UTN}$, and $\Delta P_{L,up}$. The first, $\Delta P_{Lf,3-4}$, is the pressure loss due to wall friction $[Pa]$:

$$\begin{aligned}\Delta P_{Lf,3-4} = \frac{1}{8}\rho_m f_{UTN}[V_{UTNa}^2 L_{UTN}\frac{(D_{UTNa}+D_{UTNb})(D_{UTNa}^2+D_{UTNb}^2)}{D_{UTNb}^4} + \\ V_{UTNb}^2 L_{up}\frac{(D_{slide}+D_p)(D_{slide}^2+D_p^2)}{D_{slide}^4}]\end{aligned} \tag{3.29}$$

where f_{UTN} is the friction factor [41] in the UTN region, L_{UTN} and L_{up} are the UTN length and thickness of the upper plate $[m]$, D_{UTNa} and D_{UTNb} are the UTN diameters at top and bottom $[m]$, V_{UTNa} and V_{UTNb} are the corresponding flow velocities at UTN entry and exit $[\frac{m}{s}]$. A derivation for this equation for tapered pipes is provided in Appendix A.

The second pressure loss inside the UTN, $\Delta P_{L,UTN}$, is the pressure loss due to gradual contraction or expansion [42] in the tapered UTN region $[Pa]$, and is defined as follows, according to the UTN taper:

If $D_{UTNa} < D_{UTNb}$ (gradual expansion)

$$\Delta P_{L,UTN} = \frac{1}{4}\rho_m V_{UTNa}^2 (2.6\sin(\frac{\theta}{2}))(1-\frac{A_{UTNa}}{A_{UTNb}})^2 \qquad 0<\theta<\frac{\pi}{4} \tag{3.30}$$

$$\Delta P_{L,UTN} = \frac{1}{4}\rho_m V_{UTNa}^2 (1-\frac{A_{UTNa}}{A_{UTNb}})^2 \qquad \frac{\pi}{4}<\theta<\frac{\pi}{2} \tag{3.31}$$

If $D_{UTNa} \geq D_{UTNb}$ (gradual contraction)

$$\Delta P_{L,UTN} = \frac{1}{4}\rho_m V_{UTNb}^2 (1.6\sin(\frac{\theta}{2}))(1-\frac{A_{UTNb}}{A_{UTNa}}) \qquad 0<\theta<\frac{\pi}{4} \tag{3.32}$$

$$\Delta P_{L,UTN} = \frac{1}{4}\rho_m V_{UTNb}^2 \sqrt{\sin(\frac{\theta}{2})}(1-\frac{A_{UTNb}}{A_{UTNa}}) \qquad \frac{\pi}{4}<\theta<\frac{\pi}{2} \tag{3.33}$$

where $\theta = 2arctan|\frac{D_{UTNa}-D_{UTNb}}{2L_{UTN}}|$ $[rad]$ and A_{UTNa} and A_{UTNb} are the corresponding area at UTN entry and exit $[m^2]$.

The third pressure loss in the UTN, $\Delta P_{L,up}$, is due to sudden contraction or expansion [41] upon exit from the UTN into the upper plate $[Pa]$, which may have different diameters:

If $D_{UTNb} < D_p$ (sudden expansion)

$$\Delta P_{L,up} = \frac{1}{2}\rho_m V_{UTNb}^2 (1 - \frac{A_{UTNb}}{A_p})^2 \tag{3.34}$$

If $D_{UTNb} \geq D_p$ (sudden contraction)

$$\Delta P_{L,up} = \frac{1}{2}\rho_m V_p^2 [0.42(1 - \frac{A_p}{A_{UTNb}})] \tag{3.35}$$

where V_p is fluid velocity at the upper plate in $[\frac{m}{s}]$.

3.2.3.4 Slide-gate Region (Points 4 to 5)

In flowing through the slide-gate, between points 4 and 5, four important pressure losses are considered, $\Delta P_{L_{f,4-5}}$, $\Delta P_{C,sg}$, $\Delta P_{L,sg}$, and $\Delta P_{L_{gate1}}$. The first, $\Delta P_{L_{f,4-5}}$, is the wall friction $[Pa]$, which is very small, but is included for completeness:

$$\Delta P_{L_{f,4-5}} = \frac{1}{8}\rho_m f_{UTN} V_p^2 h_{4-5} \frac{(D_{slide} + D_p)(D_{slide}^2 + D_p^2)}{D_{slide}^4} \tag{3.36}$$

where f_{UTN} is the friction factor in the UTN, h_{4-5} the height difference between points 4 and 5 $[m]$, D_p the diameter of the upper and lower plates $[m]$, which are assumed to match, V_p is the flow velocity through the upper/lower plates $[m/s]$.

The second pressure loss in the slide-gate, $\Delta P_{C,sg}$, is due to clogging as is treated as a pressure loss in the form of a kinetic energy change as follows:

$$\Delta P_{C,sg} = \frac{1}{2}\rho_m C_{sg} V_p^2 \tag{3.37}$$

where C_{sg} is the clogging coefficient of the slide-gate which can be input (settings menu in Figure 3.2) or left blank, (to default to 0 for no clogging).

The third pressure loss in the slide-gate, $\Delta P_{L,sg}$, is due to restriction of the flow $[Pa]$ [4]:

$$\Delta P_{L,sg} = \frac{1}{2}\zeta\rho_m V_p^2 (\frac{A_p}{\nu A_{gap}})^2 \tag{3.38}$$

where ν is an empirical coefficient which is defined as [43]:

$$\nu = 0.63 + 0.37(\frac{A_{gap}}{A_{sg}})^3 \tag{3.39}$$

where ζ is a slide-gate pressure loss constant (introduced here to adjust the pressure drop due to flow passing through the slide-gate), A_{gap} area of gap $[m^2]$, and A_{sg} area of slide-gate $[m^2]$. Although it is recommended to keep ζ equal to 1, this coefficient can be changed to calibrate the model if there are experimental measurements that the calculated pressure distribution by PFSG with $\zeta = 1$ does not match. To facilitate calibration, the user can leave the value of ζ blank in the Settings menu and let the inverse-modeling capability of PFSG calculate the value needed to match a given set of geometry and casting conditions.

Finally, the fourth pressure loss in the slide-gate, $\Delta P_{L,gate1}$, is due to sudden contraction or expansion at the transition between the lower part of the upper plate and the slide-gate middle-plate circular opening hole $[Pa]$, and depends on the velocity of fluid in the gap as well as slide-gate opening circular area. For a sudden expansion, the expression is the same as Equation 3.34, changing V_{UTNb} to γV_{gap}, where γ is a velocity correction factor due to turbulent flow in the slide-gate region, as explained elsewhere [4] and V_{gap} is the velocity in the gap in $[\frac{m}{s}]$. Also, A_{UTNb} is replaced with A_p (slide-gate middle plate hole area $[m^2]$), and A_p is changed to A_{sg} (lower/upper plate area $[m^2]$). For a sudden contraction, the expression is 3.35, replacing V_p with γV_{gap}, A_p with A_{sg} and A_{UTNb} with A_p.

3.2.3.5 Slide-gate to Upper SEN Region (Points 5 to 6)

In this potentially tapered region, four pressure loss terms are considered due to different geometry. The first term, $\Delta P_{Lf,5-6}$, wall friction $[Pa]$, is between points 5 and 6, and is similar to Equation 3.29 replacing γV_{gap} with V_{UTNa} and V_{UTNb} with χV_{gap} (χ is the correction factor of velocity due to turbulent flow in slide-gate region, as explained elsewhere [4]). Additionally, L_{Up} and L_{UTN} are changed to L_{USEN} (upper SEN length $[m]$), and L_{lp} (lower plate length $[m]$), respectively. Also, D_{UTNa}, D_{UTNb}, D_{slide}, and D_p are replaced with D_{slide} , D_{USENa} (upper SEN entry diameter $[m]$), and D_{USENb} (upper SEN exit diameter $[m]$), respectively. Finally, f_{UTN} is replaced with f_{SEN} (SEN region wall friction factor). In addition to wall friction, there are three more pressure loss terms between points 5 and 6 in the slide-gate region.

The next term, $\Delta P_{L,USEN}$, is pressure loss due to gradual contraction or expansion in the upper SEN region $[Pa]$. For gradual expansion, the expression is the same as Equation 3.30 or Equation 3.31 changing V_{UTNa} to γV_{gap} and replacing A_{UTNa} with A_{USENa} (upper SEN entry area $[m^2]$), and A_{UTNb} with A_{USENb} (upper SEN exit area $[m^2]$). In case of gradual contraction, the expression is the same as Equation 3.32 or Equation 3.33 changing V_{UTNb} to χV_{gap}. Also, A_{UTNa} is replaced with A_{USENa} and A_{UTNb} with A_{USENb}.

Next, $\Delta P_{L,gate2}$, pressure loss due to sudden cross section change between upper part of lower plate and slide-gate plate $[Pa]$. For a sudden expansion, the expression is the same as Equation 3.34, changing V_{UTNb} to χV_{gap}. As for the area, A_{UTNb} is replaced with A_{sg}. In case of sudden contraction, the expression is the same as Equation 3.35, changing V_p to χV_{gap}, and A_{UTNb} is replaced with A_{sg}.

Finally, $\Delta P_{L,P_2}$, pressure loss due to gradual contraction or expansion at transition between lower plate and upper SEN region $[Pa]$, The expression is the same as Equation 3.30 or Equation 3.31, in case of whether the gradual expansion, or similar to Equation 3.32 or Equation 3.33 for the gradual contraction, with appropriate changes in velocity. For gradual expansion changing V_{UTNb} is changed to V_p (fluid velocity in lower/upper plate slide-gate region $[\frac{m}{s}]$), and A_{UTNa} is replaced with A_{USENa}, and A_{UTNa} with A_p. In case of gradual contraction, V_{UTNb} changed to V_{USENa} (fluid velocity in upper SEN region $[\frac{m}{s}]$) and A_{UTNa} replaced with A_p and A_{UTNb} changed to A_{USENa}.

3.2.3.6 Lower SEN Tapered Region (Points 6 to 7)

Two pressure loss terms are present in this region. $\Delta P_{Lf,6-7}$ is the wall friction between points 6 and 7 $[Pa]$, similar to Equation 3.36 with appropriate changes in velocity, V_p to V_{USENb} $[\frac{m}{s}]$), and replacing h_{4-5} with h_{6-7} (tapered SEN length $[m]$). Additionally, D_{slide}, and D_p are changed to D_{USENa} (upper SEN entry diameter $[m]$) and D_{USENb} (upper SEN exit diameter $[m]$). Finally, f_{UTN} is replaced with f_{SEN} (SEN region wall friction factor).

Secondly, there is a pressure loss caused by possible taper in the tapered region of the lower SEN, $\Delta P_{L,tap}$ which is the same as 3.30 and Equation 3.31 or Equation 3.32 and Equation 3.33 with appropriate changes in velocity, V_{UTNb} to χV_{gap} or V_{UTNa} to V_{SEN} (in case of gradual contraction or expansion, respectively). For gradual expansion, A_{UTNb} is replaced with A_{SEN} as SEN exit area $[m^2]$, and A_{UTNa} with A_{USENb}. In case of gradual contraction, A_{UTNa} is replaced with A_{USENb} and A_{UTNb} with A_{SEN}.

3.2.3.7 Lower SEN To Port Region (Points 7 to 8)

Assuming that the lower SEN is straight below the potentially-tapered region, the only pressure loss term between points 7 and 8 is due to wall friction [41]:

$$\Delta P_{L,f7-8} = \frac{1}{2}\rho_m f_{SEN} V_{SEN}^2 \frac{h_{7-8}}{D_{SEN}} \tag{3.40}$$

where $\Delta P_{L,f7-8}$ is the pressure loss due to wall friction $[Pa]$, f_{SEN} is the SEN wall friction factor, V_{SEN} liquid velocity at lower SEN region $[\frac{m}{s}]$, h_{7-8} in the height difference between points 7 and 8 $[m]$, and f_{SEN} is the friction factor in the SEN region. Note that a beaver tail nozzle, often used in thin-slab casting, can be simulated with a long tapered upper SEN and a short lower SEN (between points 7 and 8) with larger diameter.

3.2.3.8 Port Region (Points 8 to 9)

In the port region, between points 8 and 9, there are three pressure loss terms: $\Delta P_{L,port}$, $\Delta P_{L,tee}$, and $\Delta P_{C,port}$. The first pressure loss, $\Delta P_{L,port}$, is due to sudden contraction between the lower SEN and the port $[Pa]$, and is defined as [4]:

$$\Delta P_{L,port} = \frac{1}{2}\rho_m V_{SEN}^2 (1 - \frac{A_{SEN}}{2A_{port}})^2 \qquad A_{SEN} > 2A_{port} \tag{3.41}$$

$$\Delta P_{L,port} = 0 \qquad A_{SEN} \leq 2A_{port} \tag{3.42}$$

where A_{SEN} is lower SEN area $[m^2]$, and A_{port} is port cross-section area $[m^2]$.

The second pressure drop is due to the change of flow direction [4] $[Pa]$, and is defined as:

$$\Delta P_{L,tee} = \frac{1}{2}\rho_m K V_{SEN}^2 \tag{3.43}$$

where K is the port loss constant, which can be input in the Settings menu, and defaults to 0.2 [4].

The third pressure loss in the port region is due to clogging:

$$\Delta P_{C,port} = \frac{1}{2}\rho_m C_{port} V_{port}^2 \tag{3.44}$$

where V_{port} is fluid velocity through the port $[\frac{m}{s}]$, and C_{port} is the port clogging constant, which can be input (in the Settings menu) or left blank (to default to 1).

3.2.4 Incorporation of Clogging

As shown in Figure 3.2, possible clogging can be defined at several different places. For the slide-gate and port regions, a clogging coefficient is considered (Equations 3.44 and 3.37). However, for other portions (tundish floor opening, UTN, lower/upper plate, upper SEN, tapered SEN, and lower SEN), clogging is given in terms of a specified reduction in the diameter of that nozzle portion. For example, if the original diameter of UTN is as 80 mm, 1 mm of clogging, (C=1mm), would reduce the diameter to 80-2 = 78 mm:

$$D_{C,UTN} = D_{UTN} \pm 2C_{UTN} \tag{3.45}$$

Additionally, for portions where the user inputs the area and perimeter, first the equivalent ellipse is constructed with major and minor axes calculated as follows:

$$2a = 4A\sqrt{\frac{1}{P^2 - \sqrt{P^4 - 16\pi^2 A^2}}} \tag{3.46}$$

$$2b = \frac{2A}{\pi a} \tag{3.47}$$

where $2a$, $2b$, A, and P are major axis, minor axis, area, and simplified perimeter of the portion, respectively [44].

Then, the amount of clogging is subtracted (for positive clogging) or added (for negative clogging) to the equivalent major and minor axis, according to Equation 3.45. Next, the clogged area, A_c, and perimeter, P_c, of the ellipse is calculated from the new major and minor axis lengths:

$$A_c = \pi a_c b_c \tag{3.48}$$

$$P_c = 2\pi \sqrt{\frac{a_c^2 + b_c^2}{2}} \tag{3.49}$$

Finally, the equivalent hydraulic diameter for further calculations is obtained by the following:

$$D_{H,c} = \frac{4A_c}{P_c} \tag{3.50}$$

It is important to note that the new model can accurately simulate the effects of any of the different types of clogging (such as aspiration, inclusion deposit, steel solidification skulling, etc.) on flow rate and pressure inside the nozzle flow-control system, so long as the shape and location of the clog is known. Although the effects of any clog type can be calculated, however, the focus of the PFSG model and the work done by Yang et al.[4] is on the aspiration-type clogging. These models can even quantify the aspiration rate for such clogging [4]. The prediction of other types of clogging is beyond the capability of the current model, but is certainly worthy of investigation in future work.

3.2.5 Slide-gate Opening Definitions/Relations

Four different popular definitions of the slide-gate opening, shown in Figure 3.4, are considered in the PFSG modeling package. Note that in PFSG, the lower and upper plate diameter are considered equal, D_p, and also match the, D_{USENa}, while the hole in the middle plate, D_{slide}, can be smaller.

3.2.5.1 Linear Slide-gate Opening

The linear slide-gate opening, f_L, is defined as:

$$f_L = \frac{L}{D_{slide}} \tag{3.51}$$

where D_{slide} is the middle-plate hole diameter $[m]$ and L is the gap opening length $[m]$, (Figure 3.4(b)). It ranges from zero (closed), when $L = 0$, to 100 pct (fully open), when $L = D_{slide}$. For any position, the gap opening distance L is the maximum distance from the left side of the nozzle bore (lower/upper plate hole diameter) to the right side of the circular opening in the sliding gate plate. Note if the middle plate hole is smaller than the nozzle bore then there is still some flow restriction even when the slide-gate is 100 pct open.

3.2.5.2 Plant (Offset) Linear Opening Fraction

The plant slide-gate opening, f_p, is defined [3] by specifying the distance $E[m]$ and the distance to the reference line, $E_{max}[m]$, which is offset (relative to f_L) from the left side of the nozzle bore by the distance $(E_{max} - D_{USENa})$, and is expressed as:

$$f_p = \frac{E}{E_{max}} \tag{3.52}$$

This common situation occurs when the reference line for $E = 0$ does not match with the left edge of the nozzle bore diameter (shown in Figure 3.4). For this situation of an offset, the gap opening ranges from zero (when $E = E_{max} D_{USENa}$) to fully open (when $E = E_{max}$).

3.2.5.3 Area Fraction

The area-based gate opening, f_A, is defined by:

$$f_A = \frac{A_{gap}}{A_{Bore}} \tag{3.53}$$

where A_{gap} is the area of the gap opening (black shaded region in Figure 3.4(b)) in $[m^2]$ and A_{Bore} is the area of the lower plate hole $[m^2]$.

3.2.5.4 Center To Center Distance

Another way to define the slide-gate opening used in some plants is Center-to-Center distance, $CTC[m]$. This measure of opening is simply the distance between the two center lines of the nozzle bore (lower plate opening) and the slide-gate opening. A given CTC value can be converted to f_L as follows:

$$f_L = \frac{\frac{D_{slide} + D_p}{2} - CTC}{D_{slide}} \tag{3.54}$$

3.2.5.5 Implementation

The user typically inputs f_L and E_{max}, and PFSG then outputs all of the results, including those based on the second and third definitions, f_p and f_A. In case f_L is left blank and both E and E_{max} are also unknown, PFSG first calculates f_L based on the rest of the casting conditions. Then assuming $E_{max} = D_{USENa}$, (no offset), PFSG calculates E according to Equation 3.56. Alternatively, if f_L is left blank and both E and E_max are input, then PFSG calculates f_p and uses it to find and output f_L (Equation 3.56). If f_p is input and either E or E_{max} are left blank, then PFSG outputs the missing value (E or E_{max}) in addition to f_L. If both E and E_{max} are missing, then f_p is assumed equal to $f_L(\frac{D_{slide}}{D_{USENa}})$, meaning $E = L$ and $E_{max} = D_{USENa}$ and there is no offset. The relationship between f_p and f_L is:

$$f_p = \frac{f_L D}{E_{max}} + \frac{Offset}{E_{max}} \tag{3.55}$$

Where the offset distance is related to E, f_L, D, E_{max}, and D_{USENa} as follows:

$$Offset = E - f_L D = E_{max} - D_{USENa} \tag{3.56}$$

$$D = min(D_{slide}, D_{USENa}) \tag{3.57}$$

The plant offset method with f_p is useful for model calibration, if there is uncertainty regarding the location of the reference line in the plant relative to the edge of the nozzle bore. Note that the user can input linear opening distance (instead of linear opening fraction), as a special case of f_p simply by setting E_{max} to D_p, and inputting E, which will then become the same as L. Beware that one of E, E_{max}, and f_L must be left blank, or the gap opening is over constrained and the program will give an error message if the 3 inputs are not compatible.

3.2.6 Model Solution Procedure

The 10 pressure energy equations [4], Equation 3.1, are solved simultaneously, in a fully-coupled manner, for the user-specified unknowns using the implicit FSOLVE subroutine in MATLAB [39]. FSOLVE uses, as default, Dogleg method for solution in which the maximum number of iterations and function evaluations allowed are 400 and 100, respectively [39]. Also, the termination tolerance for the function value and the termination tolerance for x (unknown) is set to be 10^{-32}. This equation solver aims to ensure the error in the total energy balance is as close as possible to zero. The error is the difference between pressure at point 2 (bottom of the tundish) and the hydrostatic pressure calculated at the tundish bottom, which is the maximum pressure in the system. This difference is equal to pressure at point 1 (molten steel surface in tundish). The associated error, F1, is defined then as:

$$F_1 = P_2 - \rho_L g h_{1-2} \tag{3.58}$$

Therefore, FSOLVE iterates to ensure the pressure at point 1 to be as close as possible to zero gauge pressure. After convergence, the solution error is only about $10^{-12}\frac{kJ}{m^3}$ $(10^{-10}pct)$. The entire model runs in less than 10 s on a personal computer and typical converges to within $10^{-3}\frac{kJ}{m^3}$ error in energy balance. Finally, if the user specifies all inputs, then the model simply solves for the error in the energy balance, which does not require iteration with FSOLVE, and runs in only a few seconds.

3.2.7 PFSG Inputs and Outputs

Input data for the PFSG model includes the nozzle geometry (dimensions) and casting conditions. Several examples for cases studied in this chapter are given in Table 3.1 (in page 24), including the Standard nozzle, used at the former Inland Steel caster, and studied in previous work [3]. Conditions (input data) for the Standard nozzle case are also shown in Figure 3.2.

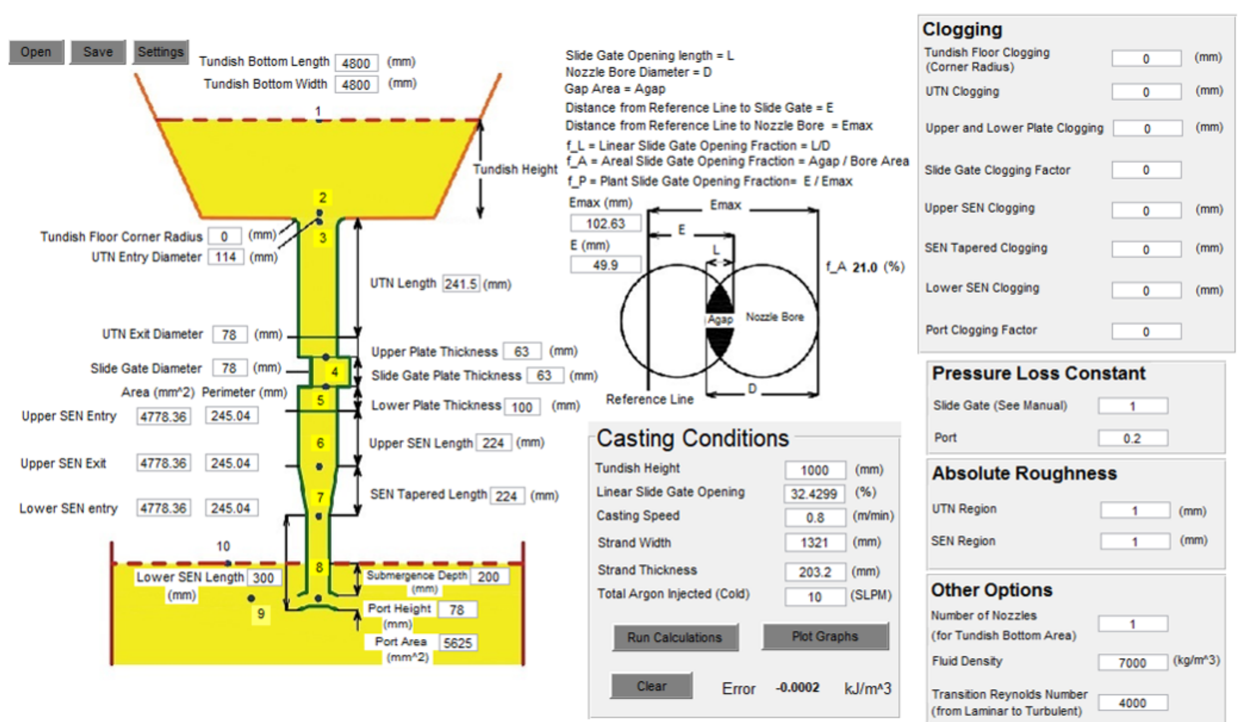

Figure 3.2 PFSG V.3.2 user interface showing input data for Standard nozzle conditions.

Table 3.1 Nozzle dimensions and plant casting conditions studied in this chapter

Dimension/Condition	Standard nozzle	Nozzle 1	Nozzle 2	Nozzle 3	Nozzle 4
UTN entry diameter $[mm]$	114	80	111	81	30
UTN length $[mm]$	241.5	255	280	254	188.5
Upper plate thickness $[mm]$	63	50	25	50	14
UTN exit diameter $[mm]$	78	80	70	78	30
Middle sliding plate thickness $[mm]$	63	25	40.5	35	17
Middle sliding plate hole diameter $[mm]$	78	80	70	80	30
Lower plate thickness $[mm]$	100	160	35	160	14
SEN bore diameter $[mm]$	78	75	72.73	85	30
SEN length $[mm]$	748	714	776	709	327
Slide-gate opening $f_L[\%]$	32.4	40.2	57.9	43.2	47
Tundish height h_{TUN} [mm]	1000	1040	1004	927.2	370
Casting speed $V_c[\frac{m}{min}]$	0.8	0.6	1.3	0.6	0.92
Argon gas flow rate $[SLPM]$	10	6	6	0	0
Submergence depth $[mm]$	200	210	110	180	60
Slab width $[mm]$ × thickness $[mm]$	1321x203.2	300x1900	1384x235	2300x300	500x75
Fluid density $[\frac{kg}{m^3}]$	7000	7000	7000	7000	1000
Clogging	0(everywhere)	0(everywhere)	0(everywhere)	0(everywhere)	0(everywhere)

The PFSG model assumes that upon injection into the nozzle, argon gas heats instantly to 1823 K, according to previous work [45]. The dynamic viscosity of the fluid is set at 0.001 $Pa.s$ for water and 0.0063 $Pa.s$ for molten steel. Finally, standard STP conditions, for gas injection, are $P_{atm} = 101kPa$ and $T_{amb} = 298K$.

The first output of PFSG, shown in Figure 3.3(a), is the gauge pressure distribution plot down the 10 different points in the tundish, UTN, SEN, and mold, arranged according to vertical distance. Next is a plot of flow rate in the system predicted as a function of slide-gate opening, for all three definitions of the opening (shown in Figure 3.3(b)).

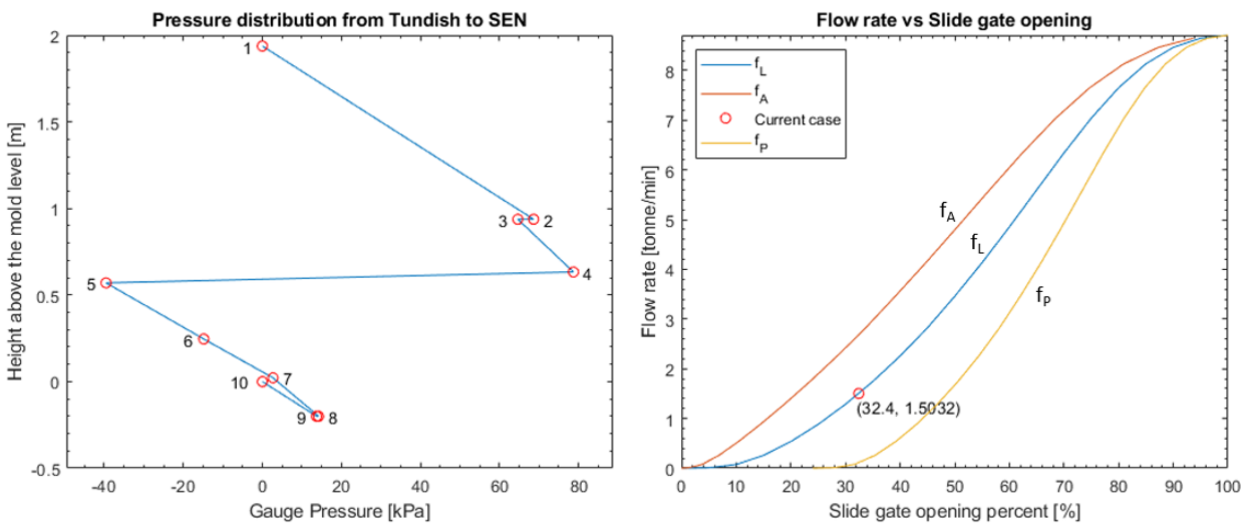

Figure 3.3 Results for Standard nozzle (PFSG V.3.2) (a) pressure distribution (b) flow rate for different definitions of gate opening.

Figure 3.4 shows the third output plot: the relation between linear slide-gate opening fraction (f_L), slide-gate area-opening fraction, (f_A) and plant offset linear opening fraction (f_p) for the given E and E_{max}. If E and E_{max} are both omitted, then E_{max} is set to D_{USENa} (offset distance = 0), so the plant offset linear fraction then coincides with the linear slide-gate opening fraction (shown in Figure 3.4). Finally, PFSG outputs the error in the energy balance $[\frac{kJ}{m3}]$ for the conditions specified, which should be nearly zero, i.e. < 0.1 $[\frac{kJ}{m3}]$, if the input data is compatible (shown in Figure 3.2).

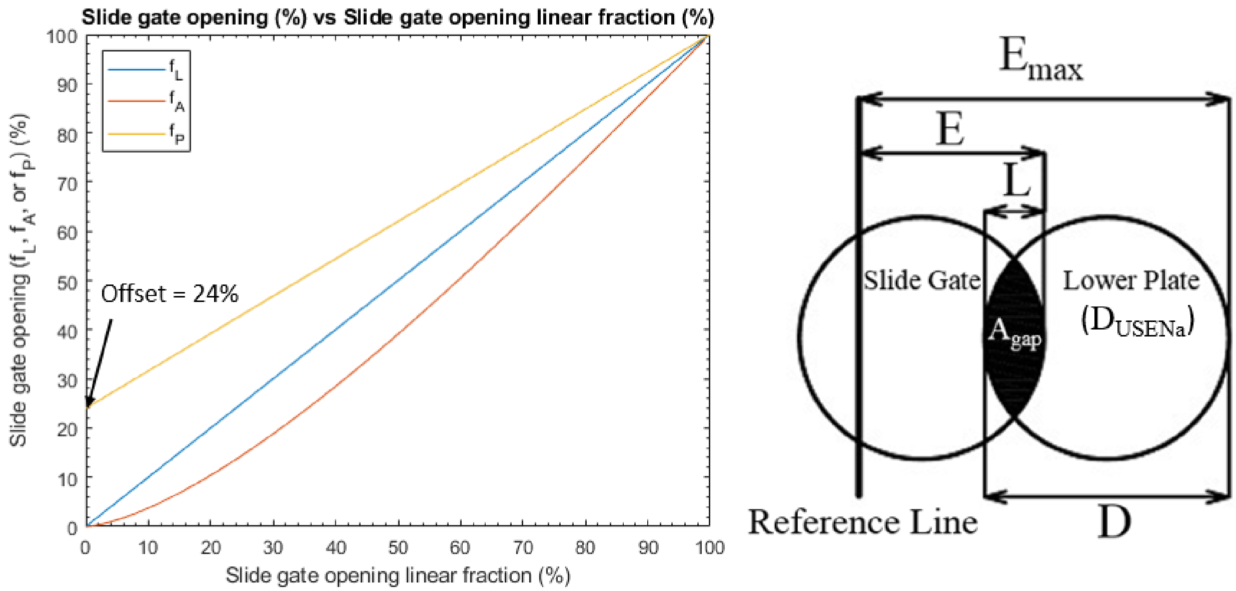

Figure 3.4 (a) Relationship between f_p, f_L, and f_A (b) geometrical relationship between parameters in calculating f_L and f_p for Standard nozzle ($D_{slide} = D_{USENa}$).

An important feature of the PFSG program is its ability to conduct parametric studies, in which the effect of changing one or more casting condition(s) or geometrical input(s) on the pressure distribution/flow rate can be studied. In addition, the program can also be used as an inverse model to determine the value of one unknown casting condition, given all of the other inputs (casting conditions and geometric data). This feature is particularly useful for researchers, process engineers, and other professionals in the steel industry to calibrate the model for a given plant, and then to apply it to solve problems and to gain deeper insights into the pressure and flow-related phenomena that affect continuous casting of steel.

The first version of PFSG was basically a user-friendly version of the model by Yang et al.[4] in which the inverse-capability of parametric study was added. PFSG V.1 also generated the three graphs and output file of useful information. Later versions of PFSG added features to this model. PFSG V.2.2 added FSOLVE, the Settings menu to customize clogging at different places inside the nozzle, absolute roughness in UTN and SEN, pressure loss constant at slide-gate region and port, fluid density (in case the water model is required to be analyzed), number of nozzles exiting the tundish bottom, and the transition Reynolds number for turbulence.

Finally, PFSG V.3.2 implemented variable argon gas flow rate inside the UTN, slide-gate, and SEN according to the local pressures when solving Equation 3.14. It also implemented an improved iteration method. This enabled incorporating the mixture density, which is highly coupled, and thus improved the model accuracy over PFSG V.2.2, which simply assumed constant density, based on the liquid phase. This version also generalized the inverse modeling feature. The value of any one of 6 missing casting conditions (Main window) or any one of 8 missing Clogging values or the slide-gate Pressure Drop Constant (Settings Menu) may be left blank (unknown) (Figure 3.2) and solved by PFSG.

3.3 Model Verification and Validation

In order to validate and verify the pressure energy model (PFSG), flow rate and pressure distribution prediction of the model is compared with CFD simulations and with available data from plant measurements and water model experiments. The information regarding validation nozzles are given in Table 3.1. Please note that two different versions of PFSG are used: PFSG V.2.2 (which assumes constant argon gas expansion) and PFSG V.3.2 (which considers argon gas expansion varying with position in the nozzle according to the local pressure).

3.3.1 Verification of PFSG with CFD Simulations

A three-dimensional finite-volume Computational Fluid Dynamics (CFD) model was applied to predict velocity and pressure fields in the nozzles during continuous casting, for both the real steel caster and water model cases. Velocity and pressure of the turbulent fluid flow inside the Eulerian domain, consisting of the UTN, slide-gate, and SEN nozzle interiors, were calculated using a Reynolds-Averaged Navier-Stokes (RANS) standard $k-\epsilon$ model for steady-state flow or a Large Eddy Simulation (LES) model for transient flow. These CFD model predictions were compared with PFSG model calculations, as well as plant and water model measurements when available.

The continuity equation for mass conservation is:

$$\frac{\partial}{\partial x_i}(\rho u_i) = 0 \tag{3.59}$$

where ρ is fluid density $[\frac{kg}{m3}]$ and u_i is velocity in the 3 coordinate directions $[\frac{m}{s}]$. The Navier-Stokes equation for momentum conservation is:

$$\frac{\partial}{\partial t}(\rho u_i) + \frac{\partial}{\partial x_j}(\rho u_i u_j) = -\frac{\partial p^*}{\partial x_i} + \frac{\partial}{\partial x_j}[(\mu + \mu_t)(\frac{\partial u_i}{\partial x_j} + \frac{\partial u_j}{\partial x_i})] \tag{3.60}$$

where p^* is modified pressure ($p^* = p + \frac{2}{3}\rho k_r$) $[Pa]$, p is gauge static pressure $[Pa]$, μ is dynamic viscosity of the fluid $[Pas]$, and μ_t is turbulent viscosity $[Pas]$ which is calculated from two additional scalar transport equations [46], of turbulent kinetic energy (k) and its dissipation rate (ϵ), or from the Smagorinsky-Lilly subgrid-scale viscosity model [47]. To consider argon gas injection in the CFD models, the two-phase Eulerian-Eulerian model is implemented into the RANS model, which solves two sets of mass and momentum equations for the liquid and gas phases [48]. A Discrete Phase Model (DPM) is two-way coupled with the LES fluid flow model, by including a source term into the momentum equation, and solving an additional transport equation for each gas bubble, as explained elsewhere [49].

For boundary conditions, inlet area at the top of the UTN (tundish bottom) was assigned as a constant-velocity inlet. The nozzle port outlets were assigned as a pressure outlet according to the hydrostatic pressure head distance from the nozzle ports to the top surface level in the mold. Nozzle walls were given standard wall functions in the RANS model, and a wall function approach given by Werner-Wengle [50] in the LES model. The initial condition was zero velocity everywhere. The equations were discretized with hexahedral finite-volume cells (e.g. Nozzle 3 case: $\sim$ 20,000 cells in the RANS model and $\sim$ 150,000 cells in the LES model), and solved for velocity and pressure by the Semi-Implicit Pressure Linked Equations (SIMPLE) algorithm, using the CFD package, Ansys Fluent [48]. Convergence of the steady-state RANS model was defined when all scaled residuals were stably lower than 10^{-4}. The transient LES model was started at time = 0 second and run for 7 seconds. First, the flow was allowed to develop for 1 second, which is longer than the residence time of molten steel inside the nozzle (total nozzle length/average velocity: 1.2 m/1.3 m/s = 0.9 second). Then, the LES simulation was run 6 seconds further to calculate time-averages of the velocity and pressure fields.

3.3.2 Validation of PFSG with Inland Steel Plant Data

Using the experimental data (curve fit of plant data) provided by Inland Steel [3], the slide-gate opening flow rate relation for Standard nozzle conditions (Table 3.1) is plotted and compared in Figure 3.5(a) with the PFSG V.2.2 and PFSG V.3.2 model predictions, and with previous CFX simulations done by Bai et al. [3]. The corresponding pressure distribution is plotted in Figure Figure 3.5(b) using both versions of PFSG.

As shown in Figure 3.5(a), the predicted relation between steel flow rate and slide-gate opening matches well with both plant measurements and the previous CFX predictions [3]. More specifically, the maximum error associated with both PFSG versions and the CFX simulations is around 6 pct, using the plant slide-gate opening with 24 pct offset from Bai [3]. These results match the upper range of the plant measurements. Decreasing the offset to 15 pct enables a closer match of PFSG with the best-fit line through the plant data.

Pressure distributions for $f_p = 62$ pct plant slide-gate opening are plotted in Figure 3.5(b). The pressure gradient predicted in the nozzles by PFSG V.3.2 is slightly lower than that of PFSG V2.2, due to the argon gas expansion and the lower density of the fluid mixture.

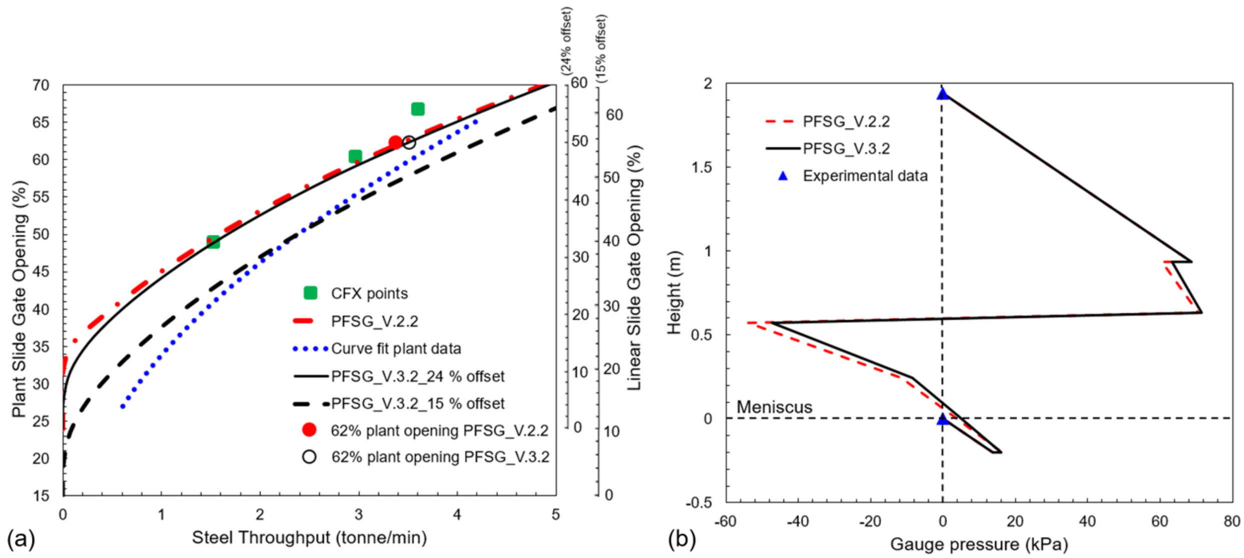

Figure 3.5 PFSG model validation with Inland Steel caster data [3] for Standard nozzle casting conditions (a) flow rate (b) pressure distribution.

3.3.3 Verification and Validation of PFSG with Plant 2 Data

Next, the PFSG models were verified with new CFD $k-\epsilon$ RANS simulations and validated with plant measurements at Plant 2 for the conditions and geometry of Nozzle 2 given in Table 3.1. The pressure distributions for 57.85 pct linear slide-gate opening with both PFSG V.3.2 and PFSG V.2.2 are compared with CFD simulation profiles in Figure 3.6. There is reasonable agreement between the pressure distributions of the CFD simulation and PFSG, which verifies the new model. PFSG V.3.2 differs only slightly from V.2.2, owing to its varying argon gas expansion according to the local pressure. Therefore, PFSG V.3.2 pressure prediction is expected to be more realistic than the Fluent and PFSG V.2.2 profiles, especially when argon flow rate is higher, so the differences are greater.

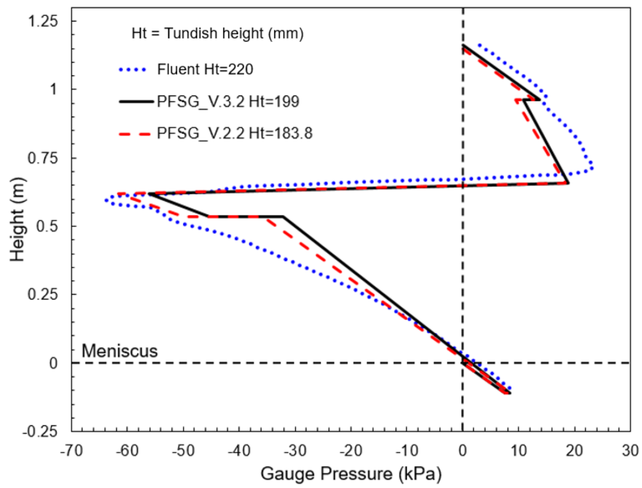

Figure 3.6 Pressure distributions verification of PFSG with CFD simulation for Nozzle 2 conditions at 57.85 pct f_L.

.

Figure 3.7 compares the predicted relation between flow rate and slide-gate opening fraction from PFSG V.3.2 with experimental data from Plant 2 [51]. The trends match reasonably well. However, a much better match was obtained using f_p with an offset of 17 mm, compared to that with f_L.

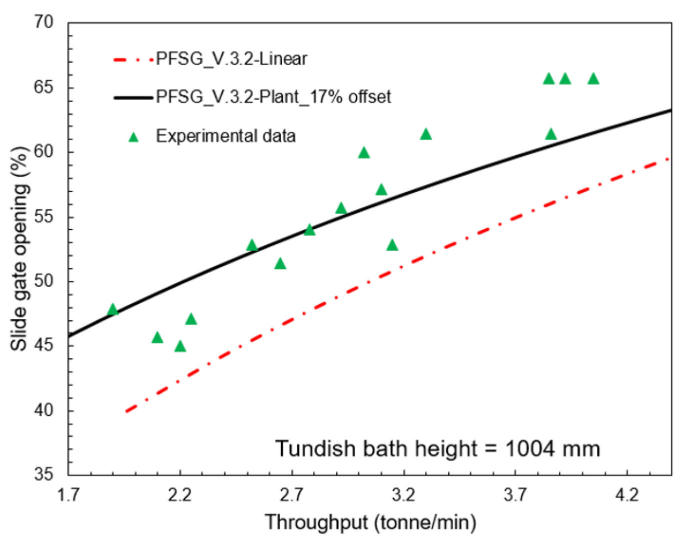

Figure 3.7 PFSG V.3.2 validation with Plant 2 data [51] for Nozzle 2 casting conditions.

.

3.3.4 Verification and Validation of PFSG with Plant 3 Data

Figure 3.8 shows the pressure distribution for Nozzle 3 (see Table 3.1) for the nozzle geometry and conditions of the steel caster at Plant 3, using new CFD simulations (both standard $k-\epsilon$ RANS and LES) together with profiles using PFSG V.2.2 and PFSG V.3.2. The pressure predictions from PFSG V.2.2 and PFSG V.3.2 match exactly, because there is zero gas injection. In addition, there is reasonable agreement between PFSG and the CFD simulations (standard $k-\epsilon$ and LES). Note that the CFD simulations do not extend into the tundish, to avoid the expense of adding the extra geometry, and because the hydrostatic pressure Equation 3.24 is very accurate in this region. The PFSG model matches best with the LES model results for the overall system pressure drop. In the local region near the slide-gate, however, the LES model produces a larger local pressure drop than either the RANS or PFSG models.

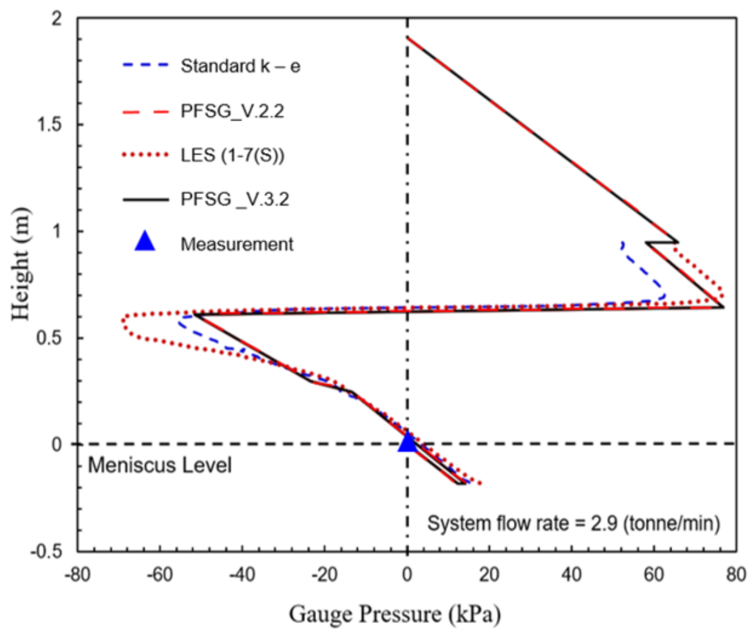

Figure 3.8 PFSG verification with Plant 3 Nozzle 3 using CFD simulations.

3.3.5 Verification and Validation of PFSG with Plant 4 Water Model Experimental Data

Finally, PFSG results are compared with measurements on a 1/3 scale water model of a steel caster at Plant 4. Details of the conditions and geometry are given in Table 3.1 for Nozzle 4. Pressure distributions are plotted in Figure 3.9 using new CFD $k-\epsilon$ RANS simulations, PFSG V.2.2 and PFSG V.3.2 calculations, and also include the experimental pressure measurements. For this case (with water), the slide-gate pressure loss constant, ζ, in Equation 3.38, in PFSG V.3.2 and PFSG V.2.2 was increased from its standard value of 1 to 2.1 in order to satisfy the energy balance. Note that the PFSG V.2.2 and PFSG

V.3.2 calculations exactly match, owing to the lack of gas injection. The results in Figure 3.9 show that the pressure distributions predicted by PFSG match very well with the pressure measurements below the slide-gate, and better than the CFD simulations. The under-prediction of the minimum pressure by the CFD model in the slide-gate region also occurred in the verification cases for Plant 2 and 3. Except in this region, the CFD predictions along three different paths inside the nozzle are almost identical, which justifies the PFSG model assumption that pressure distribution is uniform in the transverse direction across the nozzle. Finally, the PFSG pressure distributions match almost exactly with the measured tundish height.

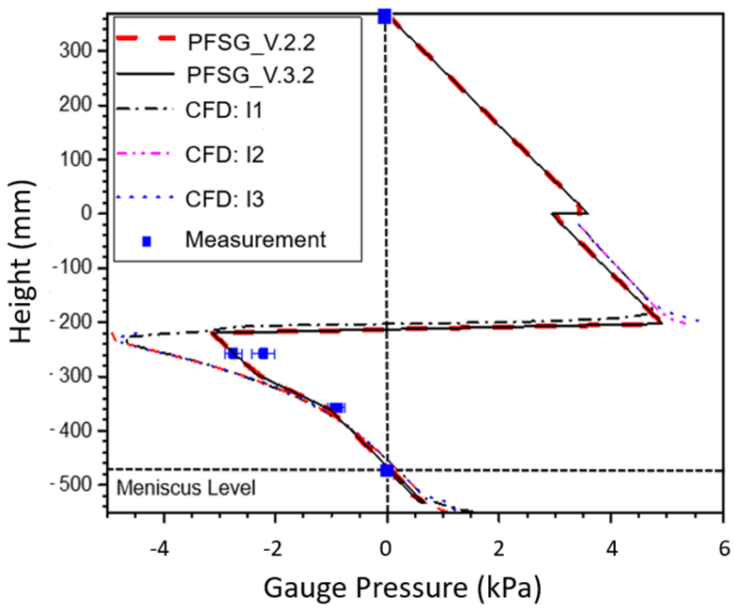

Figure 3.9 PFSG model validation with Plant 4 water model data [52] for Nozzle 4 conditions (l_1: center line, l_2: line down front, l_3: line down side of nozzle bore).

3.4 Parametric Studies

Having verified and validated the PFSG model, it was applied to conduct several different sets of parametric studies to investigate the effects of casting conditions and nozzle geometry on flow rate and minimum pressure in a typical caster with a slide-gate flow-control system. All of the studies in this section are conducted using PFSG V.3.2 with its inverse-modeling capability. The conditions are based on the Nozzle 1 and Standard nozzle geometries and casting conditions in Table 3.1, except as specifically explained, for the parametric study variations.

It is important to note that in order to maintain energy balance in the system (i.e. Error $< 0.1 \frac{kJ}{m^3}$), always two parameters must change together. Often, the slide-gate opening position (fraction) is one of these two parameters.

3.4.1 Effect of Casting Conditions and Nozzle Geometry on Flow Rate

In this section, the effect of different casting conditions and nozzle geometry on system flow rate are investigated, based on the Nozzle 1 geometry and casting conditions in Table 3.1. Specifically, the effects of changing the argon gas injection rate, lower-SEN diameter, tundish height, and nozzle submergence depth are investigated, either by allowing corresponding changes to the flow rate, or by adjusting the slide-gate opening to maintain the flow rate (and casting speed). The studies begin with an investigation of the relation between tundish height, flow rate, and slide-gate opening position.

3.4.1.1 Effect of Slide-gate Opening

The relationship between tundish height and flow rate (casting speed) depends on the slide-gate opening and is investigated with PFSG as shown in Figure 3.10. Figure 3.10(a) quantifies how, for a fixed slide-gate opening, increasing tundish height causes increasing flow and casting speed, due to the increase in the effective head of the system. Also, for a given tundish height, increasing the slide-gate opening causes an increase in flow rate. The same results are presented in Figure 3.10(b) as the relation between slide-gate opening and tundish height for a given casting speed. To maintain a constant flow rate, as the tundish height drops, the slide-gate opening must increase. The required increase in slide-gate opening is larger at low tundish heights and high casting speeds. The flow rate is most sensitive to small changes in slide-gate opening at high tundish heights and low casting speeds. Finally, Figure 3.10(b) quantifies how much more the slide-gate must open at higher casting speeds.

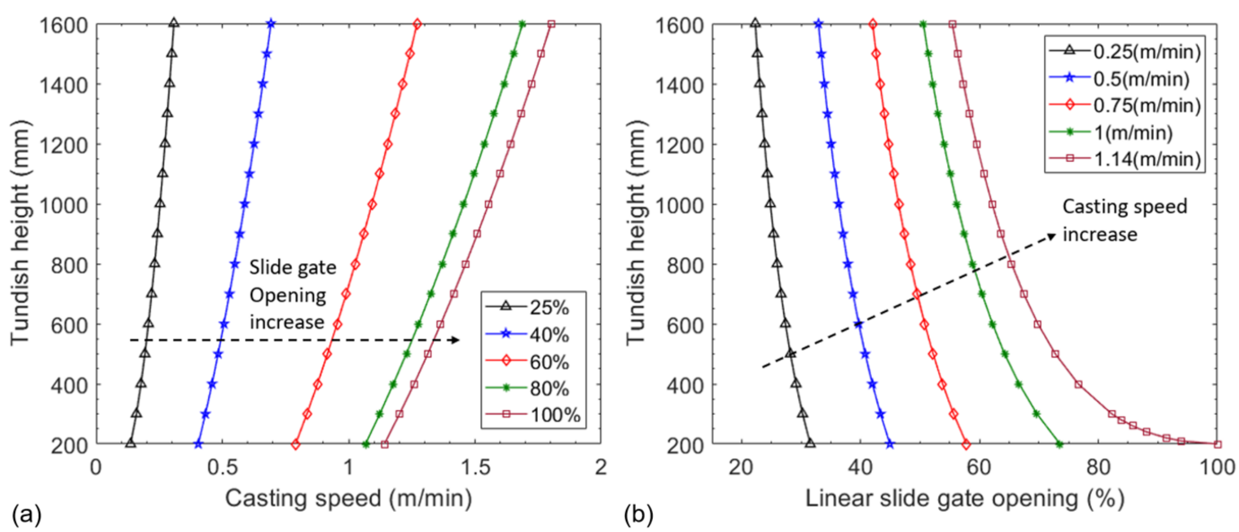

Figure 3.10 Relation between tundish height, flow rate (casting speed), and slide-gate opening for Nozzle 1 conditions plotted for (a) different slide-gate openings (b) different casting speeds.

3.4.1.2 Effect of Argon Gas Injection

Figure 3.11 illustrates the influence of argon gas injection rate on the steel flow rate for constant tundish height, (1040 m), while adjusting the slide-gate opening. To maintain a given flow rate (casting speed), increasing argon gas injection requires higher slide-gate opening. This is because maintaining a constant flow rate with more argon gas means less effective space for the molten steel, which must be compensated by a larger slide-gate opening. At a given slide-gate opening, increasing the argon gas flow rate would decrease the casting speed (flow rate). Finally, for a given argon gas injection rate, increasing slide-gate opening naturally causes increased flow rate and casting speed.

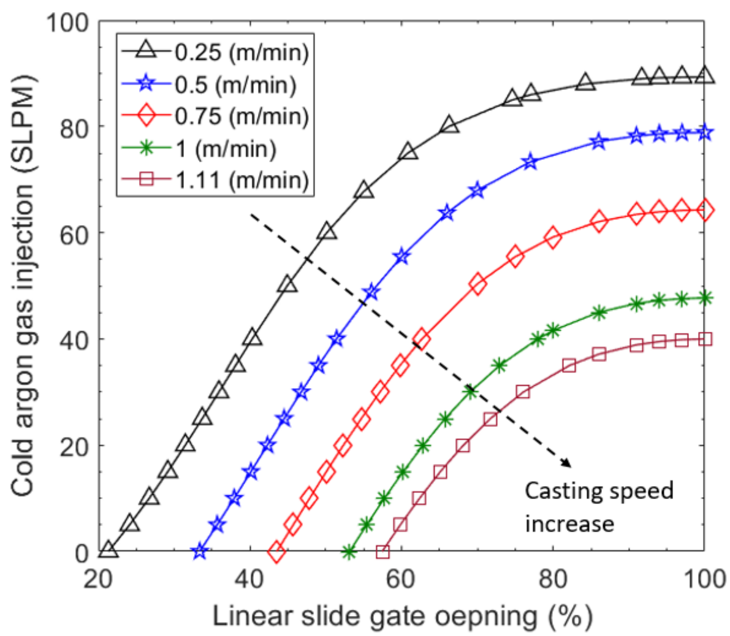

Figure 3.11 Effect of casting speed (flow rate) on argon injection rate relation with slide-gate opening for Nozzle 1 conditions.

3.4.1.3 Effect of Diameter of Lower SEN

To explore the effect of the lower SEN diameter on flow rate, casting speed is plotted in Figure 3.12 as a function of tundish height for different lower SEN diameters at a fixed slide-gate opening fraction of 40 pct. For a given diameter of the lower SEN, increasing tundish height causes an increase in casting speed, as expected. For a given tundish height, increasing the lower SEN diameter causes a higher flow rate, up to 80 mm which is a straight SEN. Increasing the diameter beyond 80mm has little effect because the flow resistance of the lower SEN then becomes negligible.

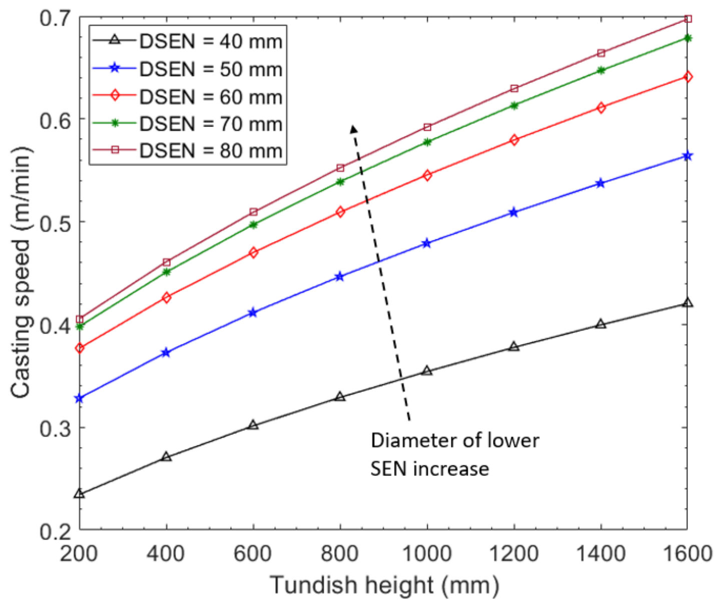

Figure 3.12 Effect of diameter of lower SEN on flow rate (casting speed) relation with tundish height for Nozzle 1 conditions (constant 40 pct slide-gate opening).

3.4.1.4 Effect of Tundish Height

Figure 3.12 also shows the effect of tundish height on flow rate/casting speed if the side gate opening remains constant. Submergence depth has the same trend as discussed later.

In actual practice at the plant, increasing tundish height requires decreasing slide-gate opening, to maintain a given steel flow rate, as already presented. These trends are alternatively quantified in Figure 3.13, which shows the effect of slide-gate opening on casting speed for different liquid levels (heights) in the tundish. This figure shows results for Standard nozzle conditions in Table 1, except that the argon flow rate was changed to consider two different values of 0 and 6 SLPM. Increasing tundish height naturally increases the casting speed, for a given slide-gate opening. It is interesting to note that the increase in casting speed is most sensitive to small changes in slide-gate opening when the system is at intermediate gate openings. At extreme low and high slide-gate openings, near to fully opened, and fully closed, the flow rate does not change as much with gate opening. Finally, comparing Figure 3.13(a) and Figure 3.13(b) shows that decreasing the argon gas injection rate (from 6 to 0 SLPM) requires a general decrease in slide-gate opening, with the same general trends. Furthermore, Figure 3.13(a) shows the theoretical situation that no flow is possible below a certain critical gate opening, due to the argon gas occupying all of the space and leaving no room for molten steel.

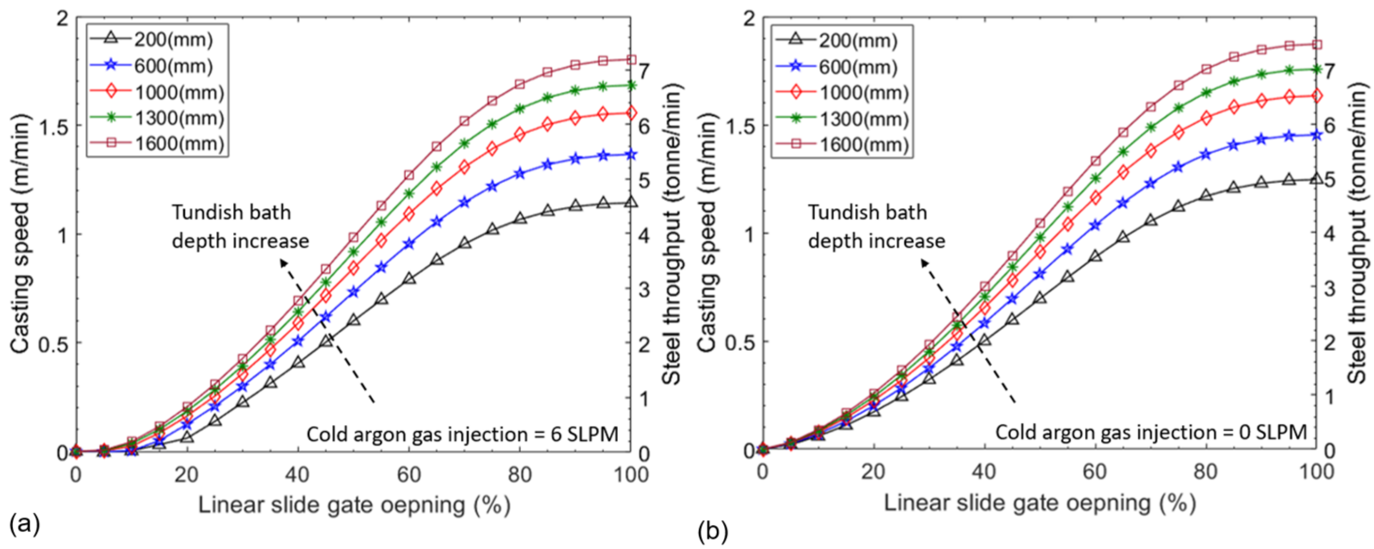

Figure 3.13 Effect of tundish height on system flow rate relation with slide-gate opening for Nozzle 1 conditions, with (a) 6 SLPM argon gas injection (b) 0 argon gas injection.

3.4.1.5 Effect of Submergence Depth

Increasing the submergence depth requires lowering of the entire tundish assembly (for a given nozzle geometry), so the effect is exactly opposite to that of tundish height. As shown in Figure 3.14 (in page 37), increasing submergence depth for a given slide-gate opening causes a decrease in flow rate and casting speed. Alternatively, increasing submergence depth while maintaining the casting speed requires an increased slide-gate opening. Except at large slide-gate openings, these effects are very small, because the typical range of submergence depths is relatively small (50 to 250mm). The results are similar when argon gas injection is decreased from 6 SLPM (shown in Figure 3.14) to zero, except that the slide-gate openings all decrease by ∼10-15 pct, depending on the casting speed. It is important to note that (tundish height - submergence depth) is the fundamental driving force for flow. Therefore, these two variables can be easily combined together into one variable: the difference in liquid level between the tundish and the mold.

3.4.2 Minimum Pressure Results

As explained earlier, the minimum pressure in the flow system occurs just below the slide-gate opening in the upper SEN. Finding the minimum pressure is important, because negative gauge pressure can cause air aspiration, which leads to re-oxidation, nozzle clogging and inclusions, resulting in defect(s) in the final product. Therefore, in this section, parametric studies are presented, based on the Standard nozzle and Nozzle 1 geometry and casting conditions in Table 3.1, to investigate the minimum pressure in the nozzle, and to find ways to raise it.

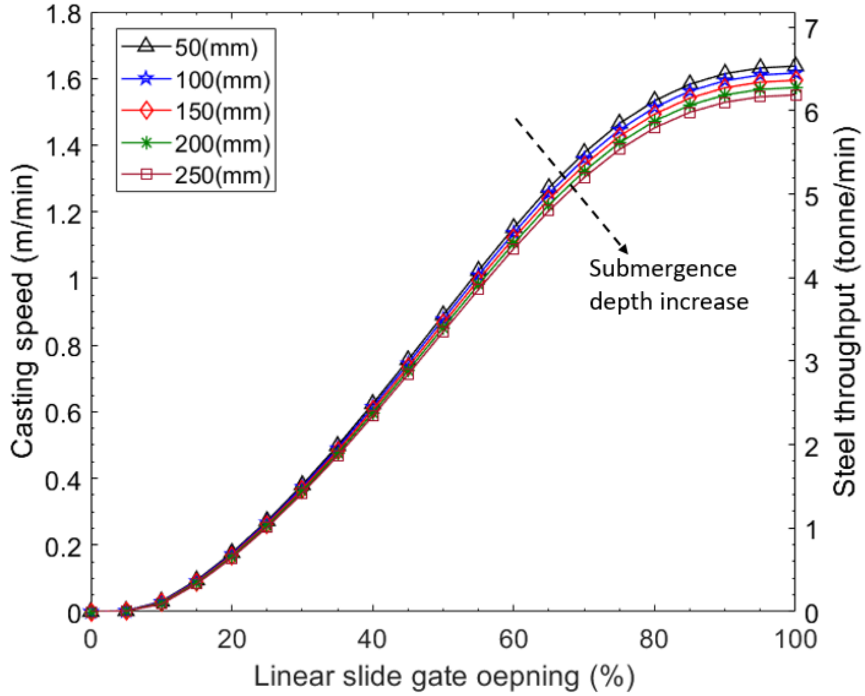

Figure 3.14 Effect of nozzle submergence depth on relation between flow rate and slide-gate opening, for Nozzle 1 conditions.

3.4.2.1 Effects of Tundish Height and Casting Speed

Figure 3.15 through Figure 3.17 show the effect of flow rate on minimum pressure at different tundish heights for Standard nozzle conditions, but with three different bore diameters of all of the nozzles (UTN, upper and lower SEN). Increasing casting speed initially causes the minimum pressure to decrease, but after reaching a critical value (minimum of minimums), further increase in casting speed causes the minimum pressure to increase. For a given nozzle bore diameter, the critical minimum pressure is always observed at the same slide-gate opening fraction, regardless of tundish height. Specifically, the minimum pressure occurs at about 50, 70, and 75 pct linear slide-gate opening for nozzle bore diameters of 75, 85, and 90 mm, respectively. The tundish height and SEN submergence depth have a negligible effect on this critical slide-gate opening. Increasing tundish height worsens the minimum negative pressure, as shown in Figure 3.15(a), Figure 3.16(a) (in page 38), and Figure 3.17(a) (in page 39). This finding suggests that to reduce aspiration in the system, tundish height should decrease.

It is worth mentioning that further increase in diameter of the nozzle bores, or excessive increase in tundish height or nozzle length may decrease the minimum pressure to below -101kPa in the model. This is not physically possible, so other physics must be activated, such as cavitation and/or non-primed flow, and the current model results are not accurate in such scenarios. This issue is more common in stopper-rod systems, as noted in recent work [36] and should be investigated in future studies.

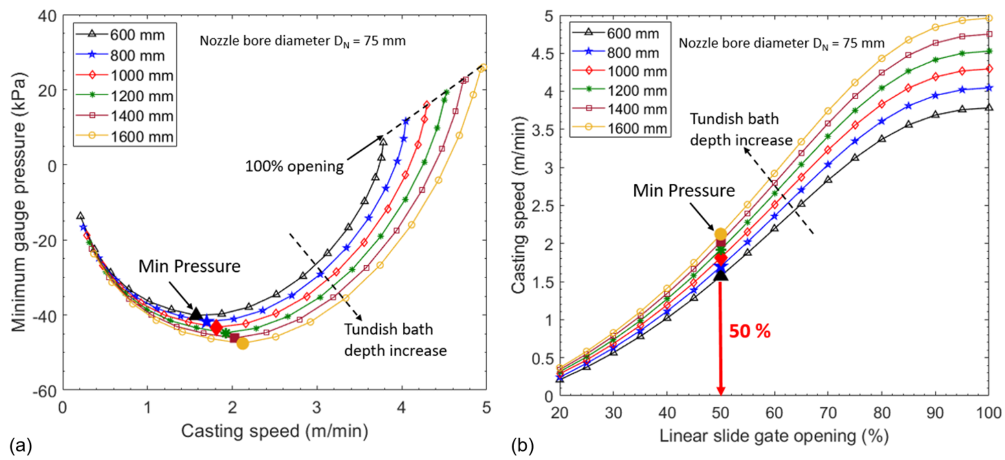

Figure 3.15 Effect of tundish height on casting speed relation with (a) minimum gauge pressure and (b) slide-gate opening (Standard Nozzle conditions but with 75mm nozzle bore).

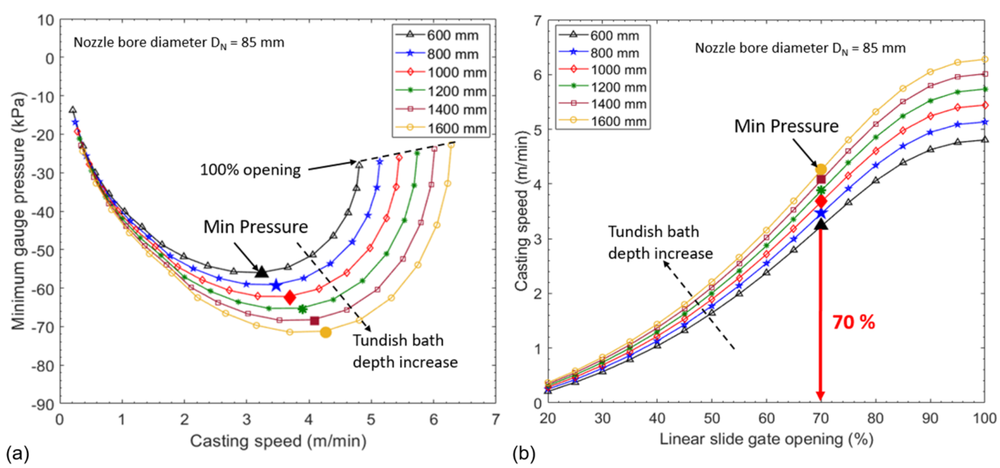

Figure 3.16 Effect of tundish height on casting speed relation with (a) minimum gauge pressure and (b) slide-gate opening (Standard Nozzle conditions but with 85mm nozzle bore).

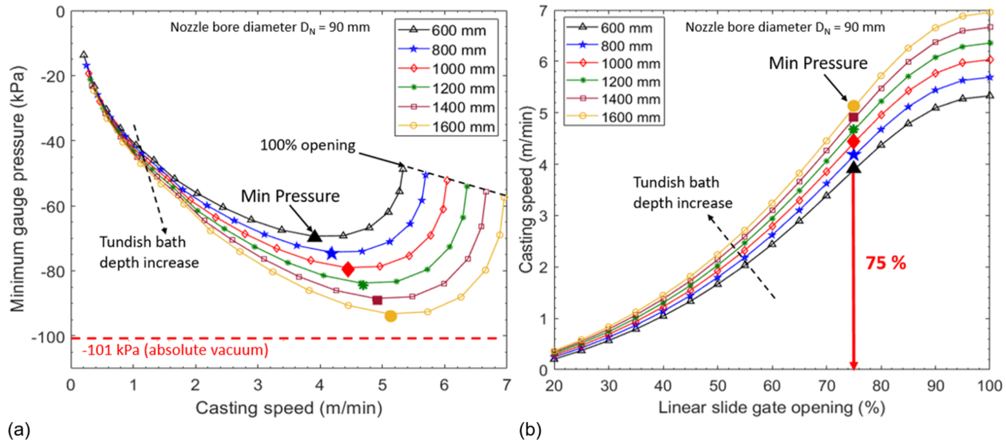

Figure 3.17 Effect of tundish height on casting speed relation with (a) minimum gauge pressure and (b) slide-gate opening (Standard Nozzle conditions but with 90mm nozzle bore).

3.4.2.2 Effects of Submergence Depth and Casting Speed

The effect of flow rate on minimum pressure in the flow system is plotted with casting speed in Figure 3.18 for different submergence depths. To maintain the energy balance, the slide-gate opening varies according to the casting speed. The effect is exactly the opposite of the effect of tundish height, as expected. Figure 3.18(b) shows that the minimum pressure is achieved at a constant linear slide-gate opening (55 pct for this case) regardless of submergence depth. Also, as submergence depth increases, the minimum pressure increases. This is due to the greater slide-gate opening required. These findings suggest that to lessen the negative pressure problem and thereby lessen air aspiration problems, nozzle submergence should be deeper.

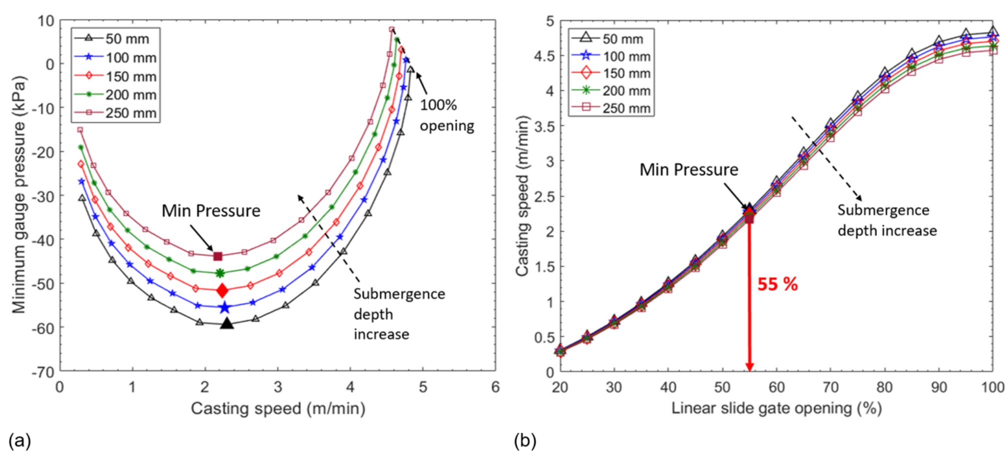

Figure 3.18 Effect of nozzle submergence depth on variation of minimum pressure with (a) casting speed and (b) slide-gate opening. (Standard Nozzle conditions).

3.4.2.3 Effect of Nozzle Bore Diameter

The effect of diameter of the lower SEN on the relation between casting speed, tundish height, and minimum pressure can be seen by comparing Figure 3.15 through Figure 3.17. In general the trends are the same, and increasing the lower SEN bore diameter causes the critical slide-gate opening that causes the lowest minimum pressure to increase, as presented in section 3.4.2. This critical slide-gate opening is almost independent of tundish height, submergence depth, and throughput. However, it increases greatly with increasing bore diameter. This trend is visualized more clearly in Figure 3.19, where it is important to note that each symbol represents many different cases.

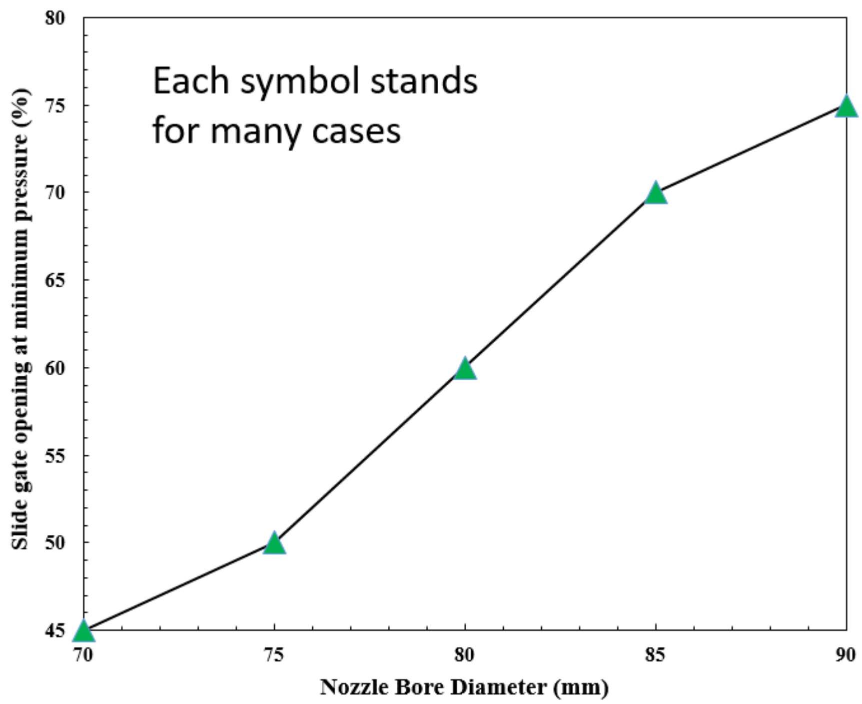

Figure 3.19 Effect of lower SEN diameter on slide-gate opening fraction at minimum pressure for Standard nozzle at various casting speeds, tundish heights, and submergence depths.

Figure 3.20 shows the value of the critical (lowest) minimum gauge pressure corresponding to the points in Figure 3.20, while operating at the critical gate opening that gives minimum pressure. The value of the minimum pressure decreases (gets worse) with increasing tundish height, decreasing submergence depth, or increasing nozzle diameter. In this figure, the casting speed varies from 1.3 $\frac{m}{min}$ (70 mm diameter SEN at tundish height of 600 mm) to 5.2 $\frac{m}{min}$ (90 mm diameter SEN at tundish height of 1600 mm). This finding suggests that air aspiration and re-oxidation problems should be minimized with lower tundish level, and/or smaller diameter of the lower SEN, which is consistent with previous findings [3].

Intermediate casting speeds should be avoided, as the minimum pressure is less severe when the slide-gate opening is near to fully opened or fully closed. Unfortunately, this last recommendation requires great care to implement in practice, and many caster operations tend to operate near the worst condition of the critical slide-gate opening.

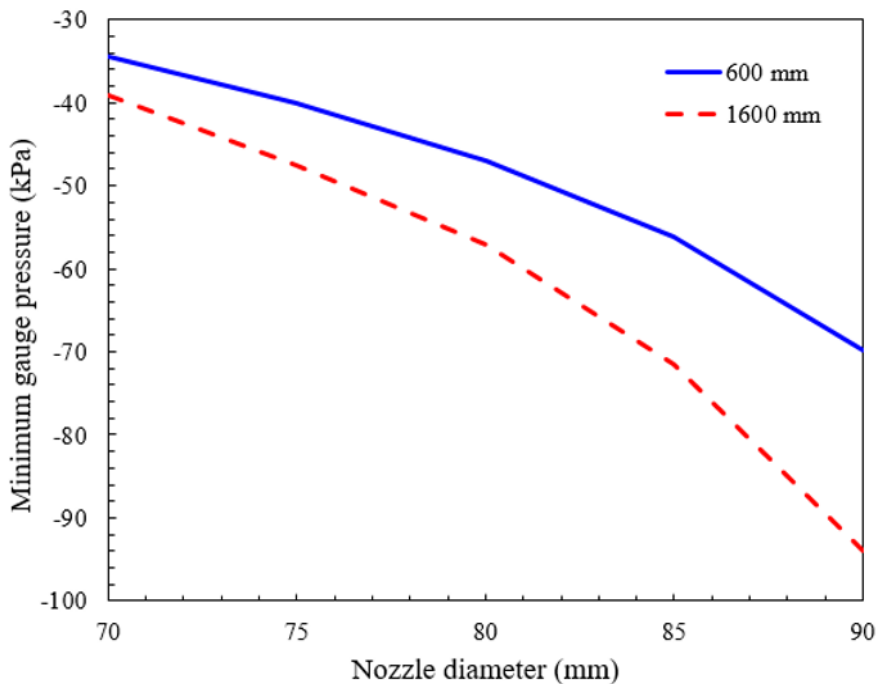

Figure 3.20 Effect of diameter of lower SEN on minimum pressure (Standard nozzle).

3.5 Conclusion

This work presents a new, standalone, user-friendly MATLAB-based graphical user interface program, Pressure-drop and Flow-rate in slide-gate systems (PFSG) to quantify pressure distribution and flow rate in continuous steel casting flow-delivery systems. This software tool includes the effects of argon gas with locally-varying expansion with pressure, clogging, and complex nozzle geometry. It can predict potential negative pressure which may cause quality problems related to air aspiration and nozzle clogging. The model is verified with CFD simulations and validated with various plant measurements and water model experiments. The maximum error associated with the validation cases is approximately 6 pct. Parametric studies with the validated model revealed the following results:

- Flow rate and casting speed increase in proportion with increasing the pressure head height that drives the flow, which is governed by the distance between the liquid levels in the tundish and mold.

- Owing to their effects on the pressure head height, the flow rate increases with increasing tundish height, increasing SEN length, and decreasing nozzle submergence depth, for a given slide-gate opening.
- Specifically, doubling the tundish height increases casting speed by about 20 pct, for the same slide-gate opening.
- Varying the nozzle submergence depth over typical commercial caster ranges, between 100 to 200 mm, does not change the flow rate significantly.
- Increasing argon gas injection requires increasing the slide-gate opening to maintain the flow rate.
- Increasing SEN diameter requires decreasing the slide-gate opening (and opening fraction) to maintain flow rate.
- The slide-gate opening fraction at minimum pressure is almost independent of tundish height, submergence depth, and throughput.
- The critical opening fraction at minimum pressure depends greatly on SEN diameter. Specifically, it increases from 45 pct open to 75 pct open with increasing SEN diameter from 70 to 90 mm, for the conditions of this study.
- The effect of argon gas on pressure depends on the slide-gate opening fraction. For large casting speeds, (with large gate openings greater than the critical fraction for minimum pressure), increasing argon injection causes increase in gate opening which increases the minimum pressure, tending to alleviate air aspiration. For small casting speeds, (with small gate openings less than the critical fraction), increasing argon injection causes increasing gate opening, which lowers the minimum pressure and aggravates the air aspiration problem.
- The minimum pressure tends to decrease (gets worse) with increasing tundish level height, and increasing nozzle bore diameter.

CHAPTER 4

PRESSURE DISTRIBUTION AND FLOW RATE BEHAVIOR IN CONTINUOUS-CASTING STOPPER-ROD SYSTEMS: PFSR

Modified from a paper to be submitted to The Journal of Metallurgical and Materials Transactions B.

Hamed Olia[9,10], B. G. Thomas[11,12], Dirk van der Plas[13,14]

Similar to chapter 3, a one-dimensional pressure energy model for stopper-rod flow delivery systems, PFSR, is introduced. The new model is able to calculate pressure distribution and flow rate in a stopper-rod controlled nozzle for argon-molten steel mixture flow including argon gas expansion by solving a system of Bernoulli equations. PFSR, like PFSG, is a MATLAB-based Graphical User Interface (GUI) software package. It employs an inverse model to solve a system of equations. It also enables users to conduct parametric studies in a very short time. The Computational Fluid Dynamics (CFD) simulations along with the water model and the plant measurements are used to verify and validate the model, respectively.

4.1 Introduction

The pressure distribution in the molten metal delivery system of a commercial steel continuous caster is important for several reasons: 1) it governs the flow rate and its sensitivity to changes in casting conditions, and 2) the minimum pressure may cause air aspiration and accompanying quality problems [3, 4]. The flow is driven by gravity according to the pressure drop between the liquid surface level in the tundish and the liquid surface level in the mold [3, 4]. A flow-control device, consisting of either a sliding gate or a stopper-rod, decreases the local cross-sectional area to restrict the flow, which causes a large local pressure drop. This is continuously adjusted during casting to maintain the desired flow rate and casting speed.

In a stopper-rod system, molten steel from the tundish flows through the thin gap between the stopper-rod and the tundish floor, down through the Upper Tundish Nozzle (UTN), into the Submerged Entry Nozzle (SEN), and finally exits the nozzle ports into the mold cavity. Just beneath the minimum gap near the stopper-rod tip, the pressure often drops below atmospheric pressure. This tends to aspirate gas leakage into the nozzle through any porous refractory, cracks, or joints in the refractory components

[9]Graduate student at the Colorado School of Mines
[10]Primary researcher and author
[11]Full Professor at the Colorado School of Mines
[12]Author for correspondence
[13]Knowledge group leader in Research and Development, TATA Steel
[14]Author

[3–5]. In some systems, argon gas is supplied to the region in order to aspirate argon instead of air if any leakage occurs [26, 53, 54]. If air aspiration from the atmosphere occurs, then the oxygen and nitrogen will react with dissolved alloy elements in the molten steel to form inclusions which may adhere to the nozzle walls as clogging, decreasing the local cross sectional area. The reaction products and clog material may agglomerate into large detrimental inclusions, which may become entrapped in the final steel as defects which lower product quality [6, 55]. In addition to lower productivity, by changing the internal geometry of the flow path inside the liquid delivery system, clogging also causes instability in the turbulent flow, leading to variations in flow rate, mold flow problems such as surface level fluctuations, and finally slivers and other serious defects in the steel product [56–58].

Clogging may occur at different places in the nozzle according to its formation mechanism [3, 5, 10]. The most susceptible places are near joints and/or cracks, where re-oxidation inclusion products form. Clogging buildup may also occur at the entrance to the UTN or at the top of the nozzle port outlets, where there may be flow separation that allows upstream inclusions to attach to the walls [3–5, 55]. Uniform clogging buildup around the perimeter of the nozzle is common if the superheat drops and a combination of clogging and frozen steel skulls can form, especially in the lower SEN [6]. Further details on clogging mechanisms and their accompanying defects are discussed elsewhere [3–5, 59, 60].

Different practices have been implemented in commercial casters aiming to alleviate clogging problems [60]. One option is to modify the nozzle geometry to lessen re-circulation and inclusion attachment to the nozzle walls [6, 55] to improve joint sealing [13] using oversized nozzle bores and ports [14, 15] to accommodate longer times of casting while clogging before a nozzle change, and varying nozzle diameter [16, 17], or insulating around the nozzle exterior to lessen skulling-type clogs [16]. A second option is to liquefy the inclusions, if they are alumina-based, by calcium treatment [18–22], or using a different nozzle material or coating, such as calcia [61–63], or boron nitride [64–66] to lessen inclusion adherence to the nozzle walls. Finally, the most common practice is to add argon into the system through stopper-rod tip, UTN, or other places inside the nozzle. Argon acts to less clogging via several different mechanisms, which are discussed elsewhere [3, 4, 6].

Several different models have been applied in previous work to predict the pressure distribution and flow rate in slide-gate or stopper-rod molten-metal delivery systems as a function of system geometry and casting conditions. Previous work on slide-gate systems is reviewed elsewhere [6, 9, 59]. Computational methods for models of stopper-rod systems include: computational fluid dynamics (CFD) models [67–73], the Bernoulli energy-balance approach, [26, 53, 70, 74], and neural networks (machine learning) [75]. The results indicate that the combined effects of stopper-rod opening, casting speed, nozzle geometry, argon gas injection rate, tundish height and submergence depth all determine the pressure distribution in the system.

Bai et al. [3] used a 3-D multiphase CFD model to calculate how the injection of argon gas can alleviate the negative pressure problem and quantified how much argon is needed for different nozzle diameters and casting conditions. For most conditions, the required argon is unfeasibly high to completely avoid negative pressure.

A one-dimensional (1-D) analytical Bernoulli energy-balance approach to model pressure and flow rate has been introduced by several researchers [26, 53, 70, 74] to calculate flow in stopper-rod systems as a function of stopper opening. For example, Liu's Bernoulli-type model [70] revealed the classic pressure distribution. This model used a clogging factor to implement the effect of clogging and quantified how much the stopper had to open to accommodate increasing clogging, in order to maintain the flow rate (and casting speed). Another such Bernoulli-type model, by Javurek et al. [26, 53], calculated pressure at various points in stopper-rod flow systems with a single tip radius using different empirical loss coefficients for single phase and multi-phase flow. Another 1-D Bernoulli-type model by Eck [74] for single-tip radius stopper-rod systems with single-phase flow featured a simple Graphic User Interface (GUI) for input data. The calculated pressure distributions predicted similar trends.

The present chapter introduces a general, flexible, computationally-efficient modeling package for calculating Pressure distribution and Flow rate within stopper-rod flow delivery systems: PFSR. Like PFSG [59], the new PFSR software package features a user-friendly GUI with an inverse-modeling solver which includes the effects of argon gas injection with locally-varying gas volume expansion, non-circular stopper-rod tip shape, and clogging that may vary with location in the nozzle. The new model is verified with three-dimension CFD simulations and validated with measurements in both water models and commercial casters. To overcome issues with non-physical negative pressure in some commercial systems, methodologies are introduced to include the effects of non-primed flow and cavitation.

4.2 Model Description

PFSR employs the Bernoulli energy-balance approach to calculate pressure distribution and flow rate in stopper-rod flow-control systems in continuous casting of steel slabs. The program features a MATLAB [39]-based GUI and several steel plants are using this offline model to understand and improve their operations. The modeled metal delivery system starts from the top surface of the molten steel inside tundish, through the stopper-rod gap region, the upper tundish nozzle (UTN), submerged entry nozzle (SEN), and ends at the top surface level in the mold. In addition to the geometry, model inputs include the casting conditions, such as the stopper-rod opening, tundish height, flow rate, slab thickness/width, argon gas injection rate, and possible clogging. The model equations, which are solved using MATLAB, are described in the next section.

4.2.1 Pressure-Energy Model Equations

A one-dimensional system of pressure - energy balance equations for continuous casting systems with stopper-rod flow control is solved using PFSR. These Bernoulli-type equations consider kinetic energy, potential energy, and turbulent dissipation pressure/energy losses [4, 59]. Similar to the approach used for slide-gate systems, PFSG, [59], general analytical expressions are obtained for the pressure/energy loss between 10 selected points distributed vertically down the flow system (Figure 4.1 in page 47), such that the pressure is calculated at each point by:

$$P_x = P_{x+1} + \rho_m g h_{x+1} - \rho_m g h_x + \frac{1}{2}\rho_m V_{x+1}^2 - \frac{1}{2}\rho_m V_x^2 + \sum \Delta P_L \tag{4.1}$$

where P_x is gauge pressure of point x $[Pa]$, ρ_m is mixture fluid density $[\frac{kg}{m^3}]$, V_x is velocity at point x $[\frac{m}{s}]$, h_x is the height of point x $[m]$, and g is gravitational acceleration $[9.81\frac{m}{s^2}]$. Fluid velocities at each point are calculated from the system flow rate, based on the effective local cross-sectional area, as described in 4.2.2. A boundary condition of 1 atm pressure is applied at the top surface levels of the tundish and mold. The pressure energy loss terms, $\sum \Delta P_L$, $[Pa]$ are explained in Section 4.2.3 below, and depend on the geometric details and flow phenomena between each pair of points. The molten steel velocity at the tundish top surface, V_1, and at top surface in the mold, V_{10}, are considered to be negligible [4, 59].

Applying Equation 4.1 to the ten points in the continuous casting system shown in Figure 4.1 yields to the following ten equations:

$$P_1 = P_2 - \rho_L g h_{1-2} \tag{4.2}$$

$$P_2 = P_3 + \frac{1}{2}\rho_m V_3^2 + \Delta P_{L,cont} + \Delta P_{L,tun} + \Delta P_{L,two} + \Delta P_{L,stopper} \tag{4.3}$$

$$P_3 = P_4 - \frac{1}{2}\rho_m V_3^2 + \frac{1}{2}\rho_m V_{UTNa}^2 + \Delta P_{L,exp} \tag{4.4}$$

$$P_4 = P_5 - \rho_m g h_{4-5} - \frac{1}{2}\rho_m V_{UTNa}^2 + \frac{1}{2}\rho_m V_{USENa}^2 + \Delta P_{Lf,4-5} + \Delta P_{L,UTN} \tag{4.5}$$

$$P_5 = P_6 - \rho_m g h_{5-6} - \frac{1}{2}\rho_m V_{USENa}^2 + \frac{1}{2}\rho_m V_{USENb}^2 + \Delta P_{Lf,5-6} + \Delta P_{L,USEN} \tag{4.6}$$

$$P_6 = P_7 - \rho_m g h_{6-7} - \frac{1}{2}\rho_m V_{USENb}^2 + \frac{1}{2}\rho_m V_{SENa}^2 + \Delta P_{Lf,6-7} + \Delta P_{L,tap} \tag{4.7}$$

$$P_7 = P_8 - \rho_m g h_{7-8} - \frac{1}{2}\rho_m V_{SENa}^2 + \frac{1}{2}\rho_m V_{SENb}^2 + \Delta P_{Lf,7-8} + \Delta P_{L,lSEN} \tag{4.8}$$

$$P_8 = P_9 - \frac{1}{2}\rho_m V_{SENb}^2 + \frac{1}{2}\rho_m V_{port}^2 + \Delta P_{L,port} + \Delta P_{L,tee} + \Delta P_{C,port} \tag{4.9}$$

$$P_9 = \rho_L g h_{sub} \tag{4.10}$$

$$P_{10} = P_{atm} = 0 \tag{4.11}$$

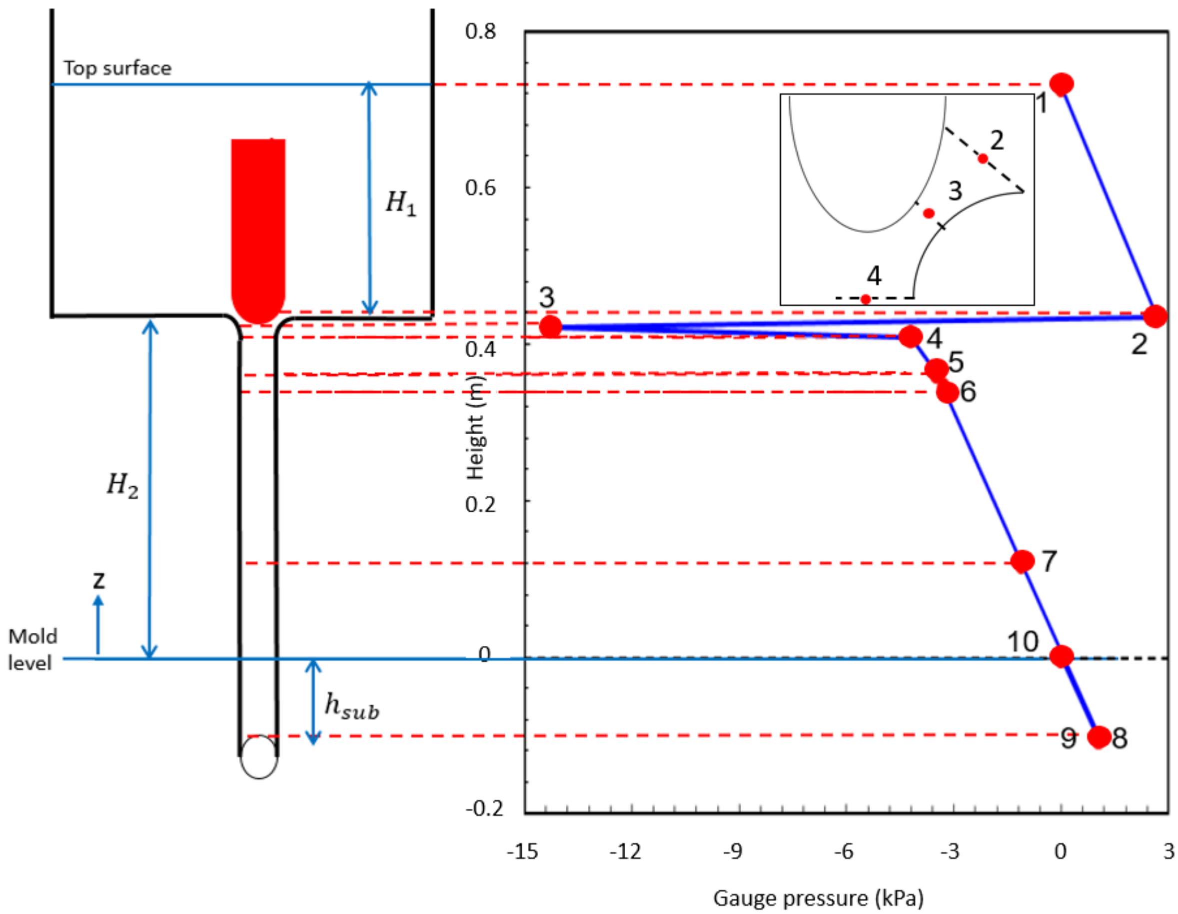

Figure 4.1 Example pressure distribution for all 10 points in a stopper-rod metal delivery system (Nozzle 1 conditions).

4.2.2 Velocity and Area Calculations

Velocity at each point in the PFSR model, V_x $[\frac{m}{s}]$, is calculated from the system flow rate as follows:

$$V_x = \frac{Q}{A_{eff,x}} \tag{4.12}$$

where Q is the liquid (water or steel) flow rate $[\frac{m^3}{s}]$, and $A_{eff,x}$ is the effective area of the local horizontal cross section $[m^2]$.

4.2.2.1 Effective Area Calculations

At any given point, x, in the flow system, $A_{eff,x}$ is the area of the local cross section of the nozzle $[m^2]$. With no gas injection, this effective area matches the physical cross-section area according to the nozzle geometry, $A_{eff,x}$ $[m^2]$. However, if argon gas is injected, then the effective area occupied by the liquid flow will be smaller:

$$A_{eff,x} = A_x(1 - \alpha_x) \tag{4.13}$$

The gas volume fraction, α_x, is defined as:

$$\alpha_x = \frac{Q_{gas,x}}{Q_{gas,x} + Q} \tag{4.14}$$

where $Q_{gas,x}$ is the flow rate of the "hot" (i.e. at molten steel temperature, $T_{hot} = 1823K$) argon gas at point x $[\frac{m^3}{s}]$ and is calculated as follows:

$$Q_{gas,x} = SLPM \frac{P_{atm}}{P_{atm} + (\frac{P_{x+1}+P_x}{2})} \frac{T_{hot}}{T_\infty} \frac{0.001}{60} \tag{4.15}$$

where $SLPM$ (standard liters per minute) is the flow rate of the "cold" (i.e. at ambient temperature $T_\infty = 298K$) argon gas injected, P_{atm} is the standard (atmospheric) pressure 101 kPa, and P_{x+1} is gauge pressure at point $x+1$ $[kPa]$ (downstream pressure). The local gas fraction can also be used to calculate the mixture density between two points:

$$\rho_m = \rho_L(1 - \alpha_x) \tag{4.16}$$

where ρ_L is liquid density $[\frac{kg}{m^3}]$.

The cross section of the UTN is considered to be circular, so can be calculated as follows:

$$A_x = \frac{\pi}{4} D_x^2 \tag{4.17}$$

where D_x is the diameter at that location, x, down the nozzle $[m]$. At other vertical locations down the nozzle system, the local cross section is based on $D_x = D_{h,x}$, the equivalent hydraulic diameter $[m]$, for more generality, based on the local area and perimeter as follows:

$$D_{h,x} = \frac{4A_x}{p_x} \tag{4.18}$$

where p_x is the perimeter at that location x $[m]$. Also [59], for a nozzle with bifurcated ports, if the area of each port exceeds half of the SEN bore area, it is set down to only half of the SEN area, because the jet exiting that port cannot expand fast enough to change its area significantly, so the rest of the area, in the upper port, typically has negligible net outward flow [3, 4].

4.2.2.2 Gap Area Calculation

The minimum cross-section area of the gap formed between the stopper-rod and tundish floor region, A_{gap}, $[m^2]$ controls the flow rate and pressure in the system. It is calculated based on the parameters shown in Figure 4.2.

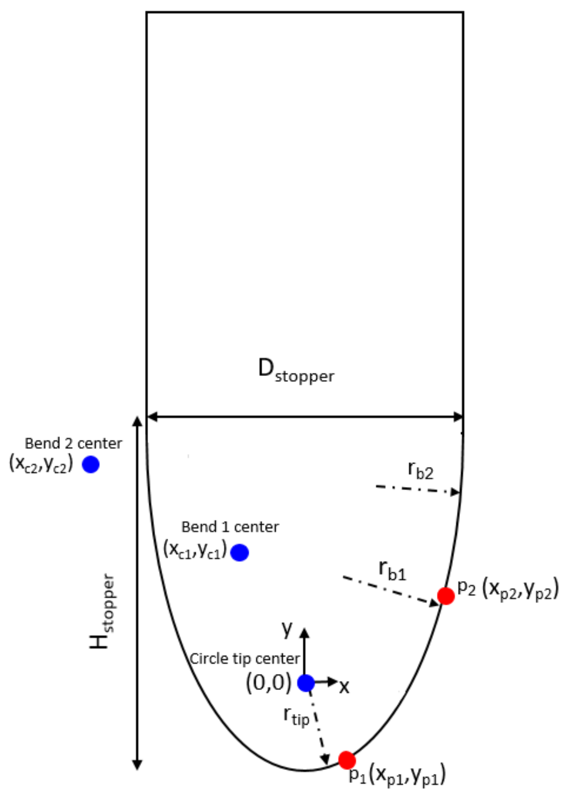

Figure 4.2 Stopper-rod schematic showing parameters associated with general nozzle tip defined with 3 radii.

These include: stopper-rod nose (tip) radius, r_{tip}, stopper-rod bend 1 radius, r_{b1}, stopper-rod bend 2 radius, r_{b2}, stopper-rod height from tip to the straight section, $H_{stopper}$, stopper-rod diameter, $D_{stopper}$, all in $[mm]$ are input by the user to PFSR to define the stopper shape. To fully define the stopper geometry, 8 more parameters are required: the coordinates of the two tangent points between part-circles p_1 and p_2 , and their centers (x_{c1}, y_{c1}) and (x_{c2}, y_{c2}). This geometry is defined relative to the nose (tip) radius center at the origin, (0,0). The following 8 independent equations are solved simultaneously for these 8 unknowns:

$$y_{c2} = H_{stopper} - r_{tip} \tag{4.19}$$

$$(\frac{D_{stopper}}{2} - x_{c2})^2 + ((H_{stopper} - r_{tip}) - y_{c2})^2 = r_{b2}^2 \tag{4.20}$$

$$(x_{p_2} - x_{c2})^2 + (y_{p2} - y_{c2})^2 = r_{b2}^2 \tag{4.21}$$

$$(x_{p_2} - x_{c1})^2 + (y_{p2} - y_{c1})^2 = r_{b1}^2 \tag{4.22}$$

$$(x_{p_1} - x_{c1})^2 + (y_{p1} - y_{c1})^2 = r_{b1}^2 \tag{4.23}$$

$$x_{p_1}^2 + y_{p1}^2 = r_{tip}^2 \tag{4.24}$$

$$\frac{y_{c2} - y_{p2}}{x_{c2} - x_{p2}} = \frac{y_{c2} - y_{c1}}{x_{c2} - x_{c1}} \tag{4.25}$$

$$\frac{y_{c1} - y_{p1}}{x_{c1} - x_{p1}} = \frac{y_{c1}}{x_{c1}} \tag{4.26}$$

where x_{ci} and y_{ci} $(i = 1, 2)$ are the x-coordinate and y-coordinate of the bend i.

The next step is to define the tundish floor geometry. The user must input: tundish floor radius, r_t, and diameter of the UTN entry, D_{UTNa}, both in $[mm]$. Assuming a single radius of curvature of this floor, this requires the coordinates of the circular segment (x_t, y_t) with given radius r_t and the coordinates of the tangent point (x_m, y_m) where the stopper touches the tundish floor when the system is fully closed (i.e no flow), as shown in Figure 4.3(a).

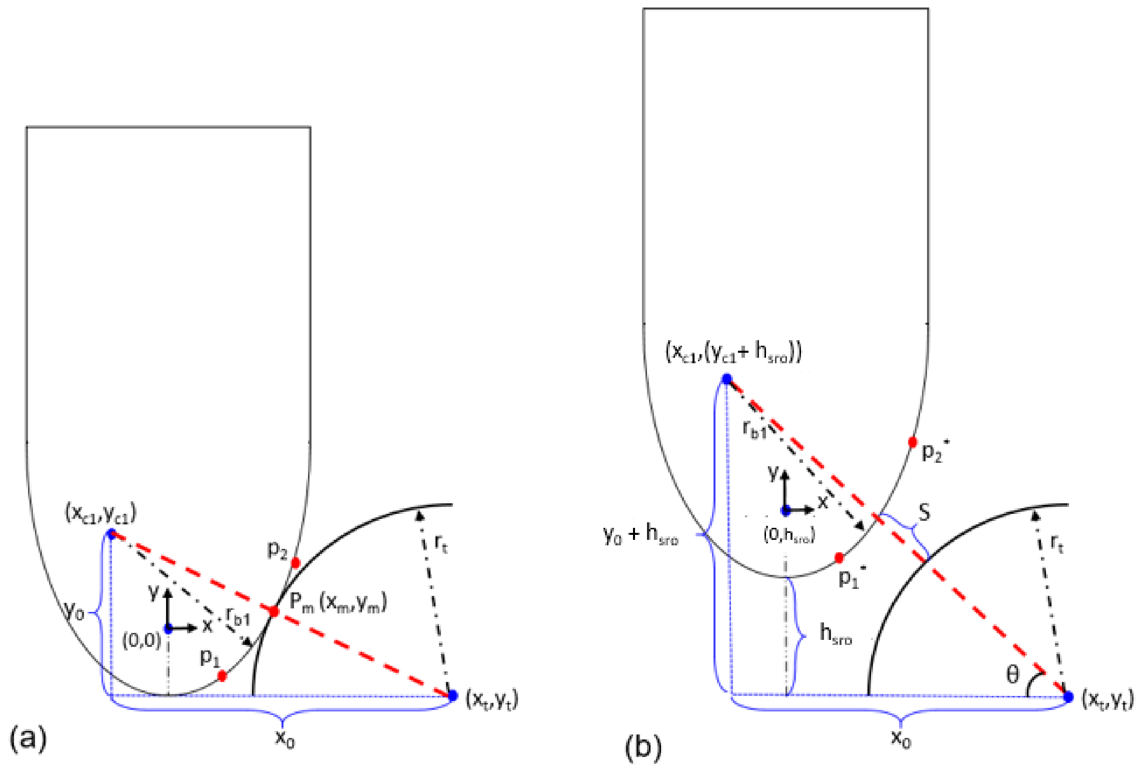

Figure 4.3 Geometrical relationship between stopper-rod and tundish floor circular segment at (a) fully closed (b) partially open position.

These 4 parameters are found by solving the following 4 equations simultaneously:

$$x_t = r_t + \frac{D_{UTNa}}{2} \tag{4.27}$$

$$(x_{c1} - x_m)^2 + (y_{c1} - y_m)^2 = r_{b1}^2 \tag{4.28}$$

$$(x_t - x_m)^2 + (y_t - y_m)^2 = r_{b1}^2 \tag{4.29}$$

$$\frac{y_{c1} - y_t}{x_{c1} - x_t} = \frac{y_m - y_{c1}}{x_m - x_{c1}} \tag{4.30}$$

From these parameters, the gap opening distance, S, for any stopper-rod opening, h_{sro}, is calculated according to the geometry shown in Figure 4.3(b) as follows:

$$S = \sqrt{(x_0)^2 + (y_0 + h_{sro})^2} - (r_t + r_{b1}) \tag{4.31}$$

and the angle θ , shown in Figure 4.3(b), is found from:

$$\theta = \arccos(\frac{x_0}{S + r_t + r_{b1}}) \tag{4.32}$$

where the horizontal and vertical distances between the center of the circular segment of the tundish floor and the center of the first bend, x_0 and y_0, are defined as follows:

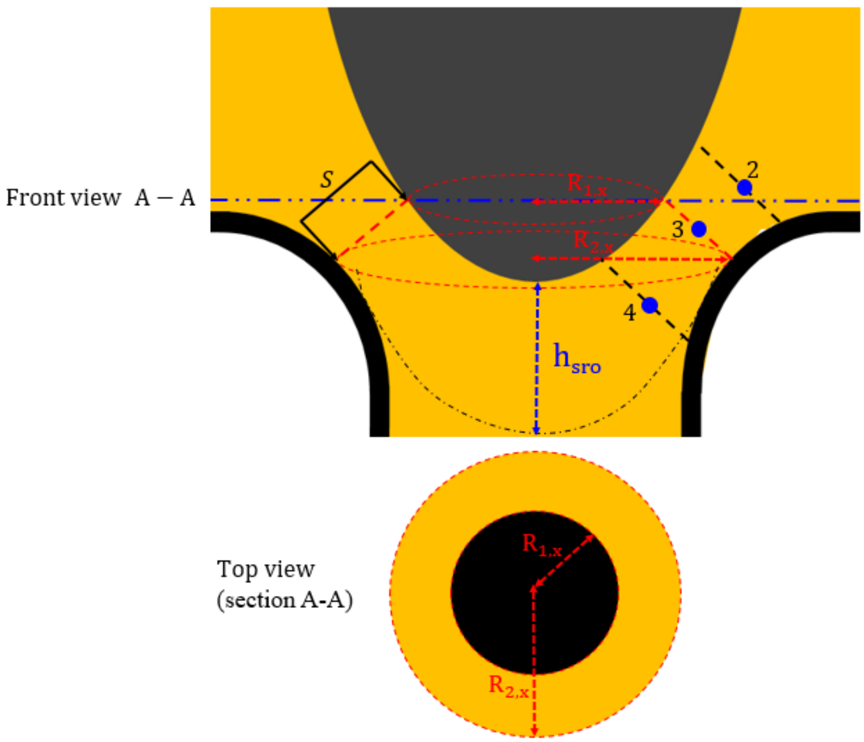

Figure 4.4 Stopper geometry showing minimum gap.

$$x_0 = x_{c1} - x_t \tag{4.33}$$

$$y_0 = y_{c1} - y_t \tag{4.34}$$

Finally, to calculate the area of the gap which is similar to a lateral surface area of a conical frustum as shown in Figure 4.4, the below equation is used [76]:

$$A_{gap} = \pi S(R_{1,x} + R_{2,x}) \tag{4.35}$$

where:

$$R_{1,x} = x_{c1} + r_{b1}\cos\theta \tag{4.36}$$

$$R_{2,x} = x_t - r_t\cos\theta \tag{4.37}$$

4.2.3 Pressure Losses

The pressure loss terms, $\sum \Delta P_L$ in Equation 4.1, between each pair of points in the PFSR model system in Figure 4.1, are defined in the following sections.

4.2.3.1 Tundish Liquid Level to Tundish Floor (Points 1 to 2)

The simple linear equation for hydrostatic pressure that relates these two points has no undefined pressure loss terms, and P_1 is at atmospheric pressure, which comprises the lower boundary condition of the system. Similarly, point 10 is the upper boundary condition fixed at 1 atm.

4.2.3.2 Tundish Floor to Gap Region (Points 2 to 3)

While passing from the tundish floor, point 2, to the minimum gap, point 3, the hydrostatic pressure increase is negligible, but the flow experiences 4 different pressure losses. First, the very large contraction in area from the tundish floor to the UTN inlet causes: $\Delta P_{L,tun}$ which is discussed elsewhere [59].

Second and further down to the UTN is the pressure loss, $\Delta P_{L,cont}$, due to contraction of area from A_{UTNr} (upper UTN surface area $[m^2]$) to A_{UTNa} (UTN inlet surface area $[m^2]$) [41]:

$$\Delta P_{L,Cont} = \frac{1}{2}\rho_m V_{UTNa}^2 (0.42(1 - \frac{A_{UTNa}}{n \times A_{UTNr}})) \tag{4.38}$$

Where V_{UTNa} is fluid velocity at UTN entry $[\frac{m}{s}]$, and n is the number of tundish nozzles (casters) where flow exits the tundish bottom.

Thirdly, $\Delta P_{L,two}$ accounts for the pressure drop due to possible argon gas injection, discussed elsewhere [59].

Finally, the most important pressure drop is caused by the contraction in area from the UTN entry A_{UTNa} to minimum gap area A_{gap}:

$$\Delta P_{L,stopper} = \frac{1}{2}\chi\rho_m V_3^2 \tag{4.39}$$

where χ is defined as [43]:

$$\chi = (\frac{1}{\mu} - 1)^2 \tag{4.40}$$

and μ is Weisbach contraction coefficient [43]:

$$\mu = 0.63 + 0.37(\frac{A_{gap}}{A_{UTNa}})^3 \tag{4.41}$$

where V_3 is the fluid velocity in the minimum gap (point 3) $[\frac{m}{s}]$. It is important to note that if the stopper-rod position is high enough that $A_{gap} > A_{UTNa}$, then the pressure loss caused by the stopper-rod becomes negligible, and only the first 3 pressure losses are present in this region.

4.2.3.3 Gap Expansion Region (Points 3 to 4)

The expansion region from points 3 to 4, is shown in Figure 4.4. Again, the hydrostatic pressure drop is negligible, so the pressure drop in this region, $\Delta P_{L,exp}$, is the expansion component of the diffuser expression [77], and is calculated from:

$$\Delta P_{L,exp} = \frac{1}{2}\kappa\rho_m V_3^2(1 - \frac{A_{gap}}{A_{UTNa}})^2 \tag{4.42}$$

where κ is diffuser pressure loss constant which is chosen as 0.35 [77]. It is very important to note that in case $A_{gap} > A_{UTNa}$, not only $\Delta P_{L,stopper}$ becomes zero, but also $\Delta P_{L,exp}$ is equal to zero (since $V_3 = V_{UTNa}$). In this case, there is no pressure loss between point 3 and 4, leading to $P_3 = P_4$.

4.2.3.4 UTN Region (Points 4 to 5)

Between points 4 and 5 inside the UTN, there are two pressure losses: 1) $\Delta P_{Lf,4-5}$, due to wall friction, and 2) $\Delta P_{L,UTN}$, due to UTN wall tapering. The wall friction loss, $\Delta P_{L_{f,4-5}}$, is defined as:

$$\Delta P_{Lf,4-5} = \frac{1}{8}\rho_m f_{UTN}[V_{UTNa}^2 L_{UTN}\frac{(D_{UTNa} + D_{UTNb})(D_{UTNa}^2 + D_{UTNb}^2)}{D_{UTNb}^4}] \tag{4.43}$$

where f_{UTN} is the friction factor [59] in the UTN region, L_{UTN} is the UTN length $[m]$, D_{UTNa} and D_{UTNb} are the UTN diameters at entry and exit $[m]$, and V_{UTNa} is the corresponding flow velocity at UTN entry $[\frac{m}{s}]$. A derivation for this equation (tapered pipes) is provided elsewhere [59].

The UTN wall tapering term, $\Delta P_{L,UTN}$, $[Pa]$, is due to gradual contraction or expansion if the UTN and is defined [59] as follows:

If $D_{UTNa} < D_{UTNb}$ (gradual expansion)

$$\Delta P_{L,UTN} = \frac{1}{4}\rho_m V_{UTNa}^2(2.6\sin(\frac{\theta}{2}))(1 - \frac{A_{UTNa}}{A_{UTNb}})^2 \qquad 0 < \theta < \frac{\pi}{4} \tag{4.44}$$

$$\Delta P_{L,UTN} = \frac{1}{4}\rho_m V_{UTNa}^2(1 - \frac{A_{UTNa}}{A_{UTNb}})^2 \qquad \frac{\pi}{4} < \theta < \frac{\pi}{2} \tag{4.45}$$

If $D_{UTNa} \geq D_{UTNb}$ (gradual contraction)

$$\Delta P_{L,UTN} = \frac{1}{4}\rho_m V_{UTNb}^2 (1.6\sin(\frac{\theta}{2}))(1 - \frac{A_{UTNb}}{A_{UTNa}}) \qquad 0 < \theta < \frac{\pi}{4} \tag{4.46}$$

$$\Delta P_{L,UTN} = \frac{1}{4}\rho_m V_{UTNb}^2 \sqrt{\sin(\frac{\theta}{2})}(1 - \frac{A_{UTNb}}{A_{UTNa}}) \qquad \frac{\pi}{4} < \theta < \frac{\pi}{2} \tag{4.47}$$

where $\theta = 2arctan|\frac{D_{UTNa} - D_{UTNb}}{2L_{UTN}}|$ $[rad]$, V_{UTNb} is the velocity at UTN exit $[\frac{m}{s}]$, and A_{UTNa} and A_{UTNb} are the corresponding area at UTN entry and exit $[m^2]$. Also, note that according to Figure 4.5, $V_{UTNb} = V_{USENa}$ (velocity at upper SEN entry $[\frac{m}{s}]$).

4.2.3.5 Upper SEN Region (Points 5 to 6)

In this potentially tapered region between point 5 and point 6, two pressure loss terms are considered. The first term, $\Delta P_{Lf,5-6}$, the wall friction pressure loss $[Pa]$, is similar to Equation 4.43 replacing V_{UTNa} with V_{USENa}. Additionally, L_{UTN} is changed to L_{USEN} (upper SEN length $[m]$). Finally, D_{UTNa} and D_{UTNb} are replaced with D_{USENa} and D_{USENb} (upper SEN entry and exit diameter $[m]$), respectively.

The next term, $\Delta P_{L,USEN}$, is the pressure loss due to gradual contraction or expansion in the upper SEN region $[Pa]$. For gradual expansion, the expression is the same as Equation 4.44 or Equation 4.45 changing V_{UTNa} to V_{USENa} and replacing A_{UTNa} with A_{USENa} (upper SEN entry area $[m^2]$), and A_{UTNb} with A_{USENb} (upper SEN exit area $[m^2]$). In case of gradual contraction, the expression is the same as Equation 4.46 or Equation 4.47 changing V_{UTNb} to V_{USENb}.

4.2.3.6 Lower SEN Tapered Region (Points 6 to 7)

The lower SEN has two pressure loss terms. Firstly, $\Delta P_{Lf,6-7}$, the wall friction between points 6 and 7 $[Pa]$, is similar to Equation 4.43 with appropriate changes for the velocity, replacing V_{UTNa} with V_{USENb} $[\frac{m}{s}]$. For the (potentially) tapered SEN length, replacing L_{UTN} with L_{tSEN} $[m]$, for upper SEN exit diameter, replacing D_{UTNa} with D_{USENb}, for SEN entry diameter, replacing D_{UTNb} with D_{SENa}, and for the wall friction factor, replacing f_{UTN} with f_{SEN}.

Secondly is a pressure loss caused by possible taper in the tapered region of the lower SEN, $\Delta P_{L,tap}$ which is the same as Equation 4.44 and Equation 4.45 or Equation 4.46 and Equation 4.47 with appropriate changes in velocity, V_{UTNb} to V_{SENa}, as fluid velocity at lower SEN entry, or V_{UTNa} to V_{USENb} (in case of gradual contraction or expansion, respectively). For both gradual expansion and contraction, A_{UTNa} is replaced with A_{USENb}, and A_{UTNb} with A_{SENa}, as SEN entry area $[m^2]$.

4.2.3.7 Lower SEN to Port Region (Points 7 to 8)

Similar to lower SEN tapered region, there are two pressure loss terms between points 7 and 8. The first term is due to wall friction, $\Delta P_{Lf,7-8}$, and is similar to Equation 4.43, with appropriate changes for the velocity, replacing V_{UTNa} with V_{SENa} $[\frac{m}{s}]$. For the (potentially) tapered lower SEN length, replacing L_{UTN} with L_{SEN} $[m]$, for SEN entry diameter, replacing D_{UTNa} with D_{SENa}, for SEN exit diameter, replacing D_{UTNb} with D_{SENb}, and for the wall friction factor, replacing f_{UTN} with f_{SEN}.

The second pressure loss term is the pressure loss for the possible taper in lower SEN region, $\Delta P_{L,lSEN}$, which is the same as Equation 4.44 and Equation 4.45 or Equation 4.46 and Equation 4.47 with appropriate changes in velocity, V_{UTNb} to V_{SENb}, liquid velocity at the exit of lower SEN region, or V_{UTNa} to V_{SENa} $[\frac{m}{s}]$ (in case of gradual contraction or expansion, respectively). Finally for both cases (gradual expansion and contraction), A_{UTNa} is replaced with A_{SENa} as SEN entry area $[m^2]$, and A_{UTNb} with A_{SENb} as SEN exit area $[m^2]$.

4.2.3.8 Port Region (Points 8 to 9)

In the port region, between points 8 and 9, there are three pressure loss terms: $\Delta P_{L,port}$, $\Delta P_{L,tee}$, and $\Delta P_{C,port}$. The first pressure loss, $\Delta P_{L,port}$, is due to sudden contraction between the lower SEN and the port $[Pa]$, and is defined as [4]:

$$\Delta P_{L,port} = \frac{1}{2}\rho_m V_{SENb}^2 (1 - \frac{A_{SENa}}{2A_{port}})^2 \qquad A_{SENb} > 2A_{port} \tag{4.48}$$

$$\Delta P_{L,port} = 0 \qquad A_{SENb} \leq 2A_{port} \tag{4.49}$$

where A_{port} is port cross-section area $[m^2]$.

The second pressure drop, $\Delta P_{L,tee}$, is due to the change of the flow direction [6] $[Pa]$, and is defined as:

$$\Delta P_{L,tee} = \frac{1}{2}\rho_m K V_{SENb}^2 \tag{4.50}$$

where K is the port loss constant, which defaults to 0.2 [59], but can be changed in Settings menu.

The third pressure loss in the port region is due to clogging:

$$\Delta P_{C,port} = \frac{1}{2}\rho_m C_{port} K V_{port}^2 \tag{4.51}$$

where V_{port} is fluid velocity through the port $[\frac{m}{s}]$, and C_{port} is the port clogging constant, which can be input (in the Settings menu) or left blank (to default to 1).

4.2.4 Incorporation of Clogging

As shown in Figure 4.5, possible clogging can be defined at several different places. In the port region, a clogging coefficient is considered [59]. Elsewhere, (tundish floor opening, UTN, upper SEN, tapered SEN, and lower SEN), clogging is specified by a reduction in the diameter of that nozzle portion. Similarly, erosion, such as caused by Ca-treated steel in an alumina nozzle is specified by an increased diameter. The methodology to account for clogging in the stopper-rod flow delivery system is similar to the one used in PFSG and is discussed elsewhere [59].

4.2.5 Model Solution Procedure

For a given set of geometrical inputs and casting conditions, the 10 fully-coupled pressure energy equations, Equation 4.2 to 4.11, defined previously, are solved simultaneously using the implicit solver, FSOLVE, in MATLAB [39], for exactly one missing user-selected casting condition input. FSOLVE uses, as default, Dogleg method for solution in which the maximum number of iterations and function evaluations allowed are 400 and 100, respectively [39]. Also, the termination tolerance for the function value and the termination tolerance for x (unknown) is set to be 10^{-32}. This solver ensures the error in the total energy balance is as close as possible to zero. This is quantified by the difference between pressure calculated at point 2 (tundish bottom) and the hydrostatic pressure calculated at the tundish bottom (Equation 4.2), which happens to be the largest magnitude pressure in the stopper-rod system (Equation 4.2). The associated error, F_1, is defined then as:

$$F_1 = P_2 - \rho_L g h_{1-2} \tag{4.52}$$

This means that FSOLVE solves for the value of the user-defined unknown (casting conditions, geometrical input, or clogging) in order to ensure the pressure at point 1 is as close as possible to zero gauge pressure. After convergence, this solution error is very small, on the order of $10^{-12}\frac{kJ}{m^3}$ ($10^{-10}\%$). The entire model runs in less than 10 s on a personal computer and the energy balance error lies within $10^{-3}\frac{kJ}{m^3}$. It is important to note that in case all inputs (geometrical and casting conditions) are given by the user, no iteration with FSOLVE is needed then the model simply and very quickly only outputs the error associated with the energy balance.

4.2.6 PFSR Inputs and Outputs

Two different sets of data are input to the PFSR model: 1) nozzle geometry (dimensions) and 2) casting conditions. Input data for 4 case studies where plant measurements are available are given in Table 4.1.

Table 4.1 Nozzle dimensions and plant casting conditions studied in this chapter

Dimension/Condition	Nozzle 1	Nozzle 2	Nozzle 3	Nozzle 4
UTN entry diameter $[mm]$	31.5	59	75	80
UTN length $[mm]$	153.4	70	350	150
UTN exit diameter $[mm]$	35.1	59	70	80
SEN bore diameter $[mm]$	35.1	59	70	85
SEN length $[mm]$	247.2	363.5	712	1054
Port height $[mm]$	81	110	100	140
Port angle (down) [deg] $[mm]$	15	15	15	15
Stopper-rod opening h_{sro} $[mm]$	3	4.6	Varying	Varying
Tundish height h_{TUN} [mm]	272	274	1067	800
Casting speed $V_c[\frac{m}{min}]$	0.72	0.75	Varying	Varying
Argon gas flow rate $[SLPM]$	0	0	0	0
Submergence depth $[mm]$	82.5	110	178	148
Slab width $[mm]$ × thickness $[mm]$	1524×76	1124×147	1500×300	1300×70
Fluid density $[\frac{kg}{m^3}]$	1000	1000	1000, 7000	7000
Transition Reynolds number [6]	4000	4000	4000	4000
Clogging	0(everywhere)	0(everywhere)	0(everywhere)	0(everywhere)

An example of the PFSR user interface, with input data conditions for Case 2, is shown in Figure 4.5. Argon gas flow rate is input to PFSR at standard temperature and pressure conditions $P_{atm} = 101kPa$ and $T_{amb} = 298K$. This gas is assumed to heat up to the molten steel temperature of 1823 K exactly at the time of injection. The dynamic viscosity of the fluid is set at 0.001 and 0.0063 $Pa.s$ for water and molten steel, respectively.

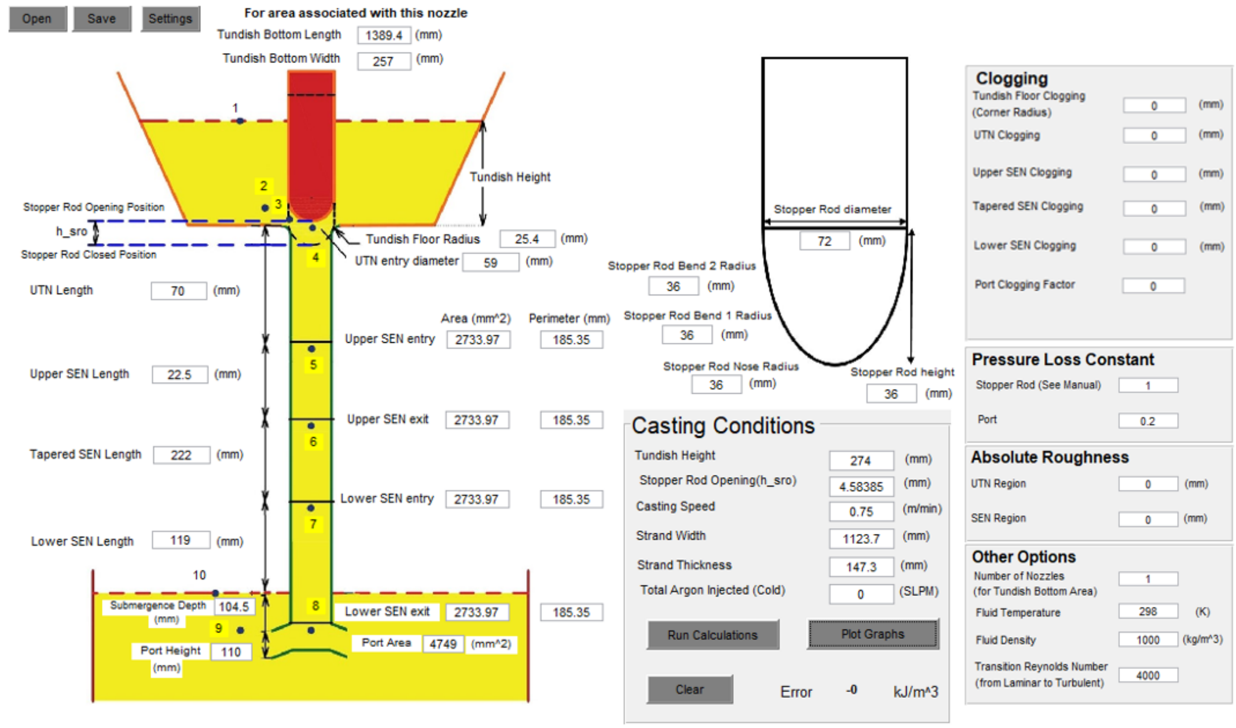

Figure 4.5 PFSR V.2.1 user interface showing input data for Nozzle 2 conditions.

The first output of PFSR is a pressure distribution plot, such as shown in Figure 4.6(a) (in page 60) . This plot shows the gauge pressure at the 10 different points in the system, arranged vertically. The second output is a plot of system flow rate as a function of stopper-rod opening (shown in Figure 4.6(b)). PFSR also outputs the total energy balance error (kJ/m^3) in the calculation.

The ability to conduct parametric studies is an important feature of PFSR. This is typically done to investigate the effect of changing a casting condition or geometrical input. Given complete geometry data and all other casting conditions, if a single casting condition (or a clogging size parameter, given in Figure 4.5) is unknown, PFSR calculates its value. This "inverse model" feature, also included in PFSG [59], enables realistic, industry-relevant parametric studies. Before that, the model should be calibrated for a given plant, which is relatively easy to accomplish.

PFSR V.1 using FSOLVE, inverse-capability of parametric study, generated the two graphs and output file of useful information. It also included the Settings menu to customize clogging at different places inside the nozzle, absolute roughness in UTN and SEN, pressure loss constant at stopper-rod region and port, fluid density (in case the water model is required to be analyzed), number of nozzles exiting the tundish bottom, and the transition Reynolds number for turbulence. PFSR V.2.1 has variable argon gas flow rate inside the UTN, stopper-rod gap, and SEN according to the local pressures when solving Equation 4.14.

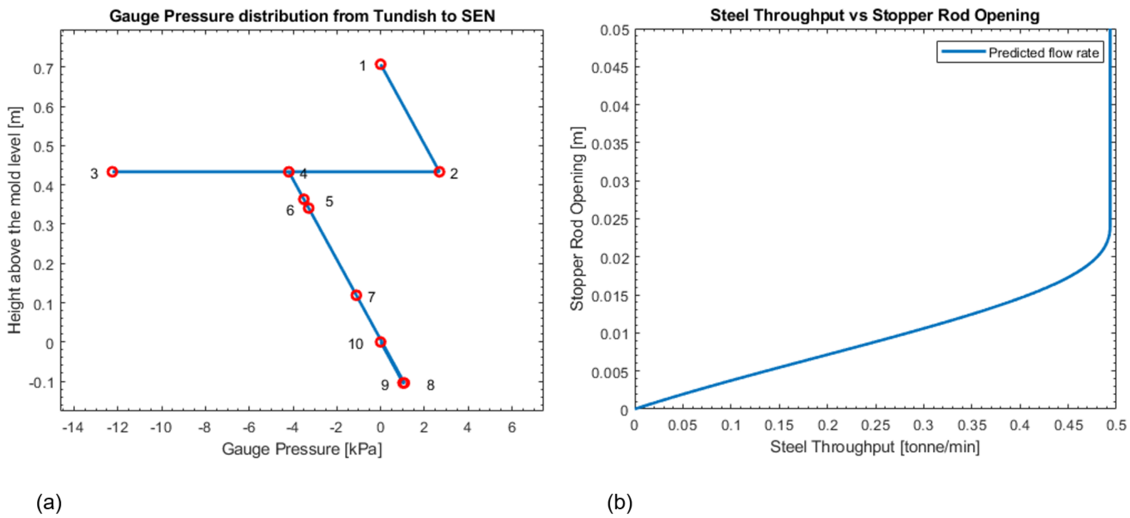

Figure 4.6 Results for Nozzle 2 (PFSR V.2.1) (a) pressure distribution (b) flow rate.

This enabled incorporating the mixture density, which is highly coupled. The value of any one of 6 missing casting conditions (Main window) or any one of 6 missing Clogging values or the stopper-rod Pressure Drop Constant (Settings Menu) may be left blank (unknown), shown in Figure 4.5, and solved by PFSR.

4.3 Model Verification and Validation

To verify and validate PFSR, pressure distribution predictions of the model are compared with CFD simulations and available data from four different sets of plant measurements and water model experiments. The system geometries and flow conditions of the different data sets are given in Table 4.1.

4.3.1 Verification of PFSR with CFD Simulations

A three-dimensional (3D) finite-volume CFD model was employed to calculate velocity and pressure fields in several stopper-rod nozzle flow systems during continuous casting, for both water model and real steel caster cases. The Eulerian domain includes a portion of the tundish floor, the stopper-rod, UTN, and SEN nozzle interiors. The following continuity and momentum equations were solved with a Reynolds-Averaged Navier-Stokes (RANS) standard $k - \epsilon$ model for steady-state flow.

$$\frac{\partial}{\partial x_i}(\rho u_i) = 0 \tag{4.53}$$

$$\frac{\partial}{\partial t}(\rho u_i) + \frac{\partial}{\partial x_j}(\rho u_i u_j) = -\frac{\partial p^*}{\partial x_i} + \frac{\partial}{\partial x_j}[(\mu + \mu_t)(\frac{\partial u_i}{\partial x_j} + \frac{\partial u_j}{\partial x_i})] \tag{4.54}$$

where ρ is fluid density $[\frac{kg}{m3}]$ and u_i is velocity in the 3 coordinate directions $[\frac{m}{s}]$, p^* is modified pressure ($p^* = p + \frac{2}{3}\rho k_r$) $[Pa]$, p is gauge static pressure $[Pa]$, k_r is an unknown residual kinetic energy $[\frac{m^2}{s^2}]$, μ is dynamic viscosity of the fluid $[Pa.s]$, and μ_t is turbulent viscosity $[Pa.s]$. The details on the calculations of turbulent viscosity, turbulent kinetic energy (k), turbulent dissipation rate (ϵ) and the boundary condition assignments are explained previously [59]. The initial condition, element type and size, solver, and convergence criteria are similar to those used in previous work [59] and is solved using Ansys Fluent [48]. Predictions from this CFD model are compared with PFSR model calculations, as well as water model and plant model measurements when available.

4.3.2 Verification and Validation of PFSR with Water Model 1 Data

The new PFSR model is first verified with CFD simulations and validated with measurements at Plant 1 for the conditions and geometry of Nozzle 1 given in Table 4.1. Pressure distributions predicted by PFSR with a 2.8 mm stopper-rod opening are compared with 3D CFD simulation profiles in Figure 4.7.

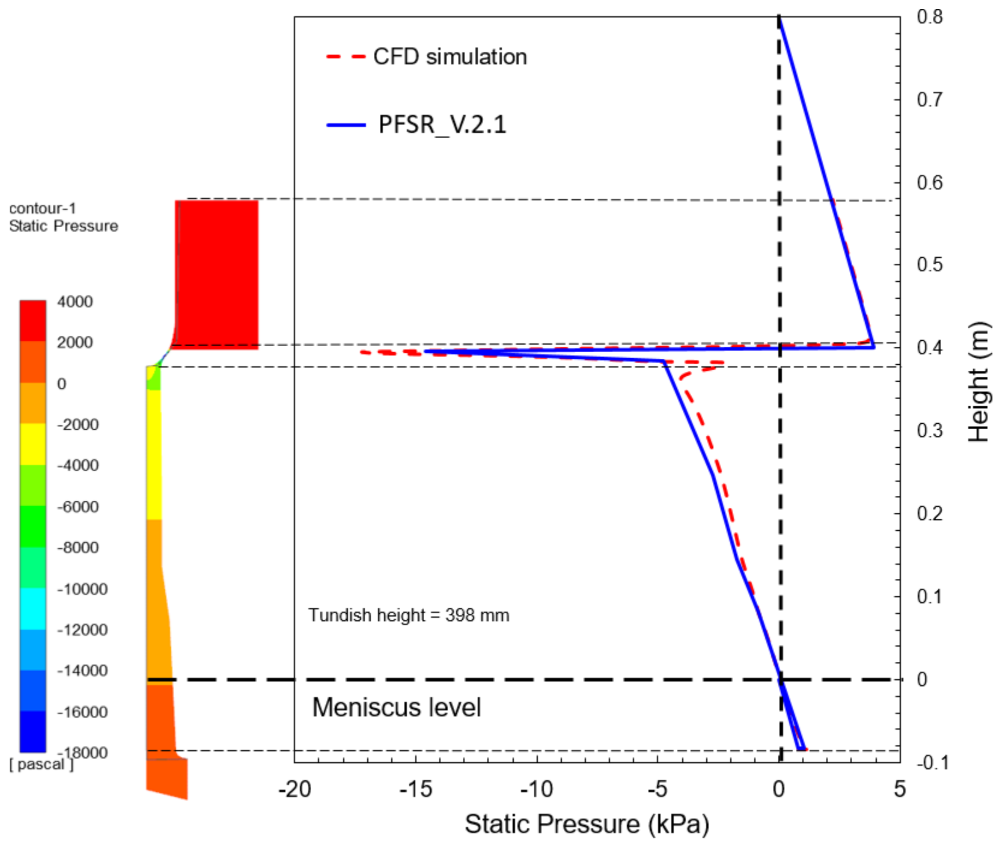

Figure 4.7 Pressure distributions verification of PFSR with CFD simulation for Nozzle 1 conditions at 2.8 mm.

To validate the PFSR model, its predictions are compared with plant measurements of the liquid levels in the tundish and mold for the given system geometry. Casting conditions include a stopper opening of 3 mm and tundish height of 272 mm. The results, shown in Figure 4.8, match very well with the plant data.

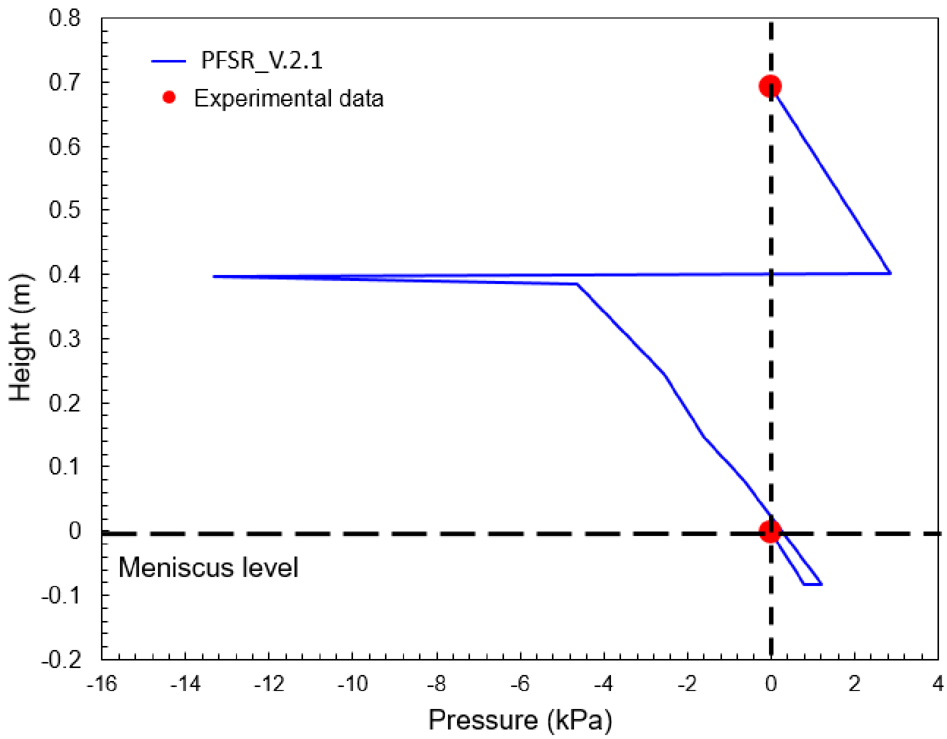

Figure 4.8 Pressure distribution validation of PFSR with measurements for Nozzle 1 conditions.

.

4.3.3 Validation of PFSR with Water Model 2 Data

Next, PFSR model predictions are compared with measurements using the 0.6-scale water model of a continuous slab caster with a stopper-rod control system housed at the Colorado School of Mines for conditions in Table 4.1 for Nozzle 2. As shown in Figure 4.9, the predicted pressure distribution matches fairly well with the water model pressure measurements. More specifically, the predictions match almost exactly in the SEN. Agreement was not as close in the UTN, where turbulent recirculating flow was observed.

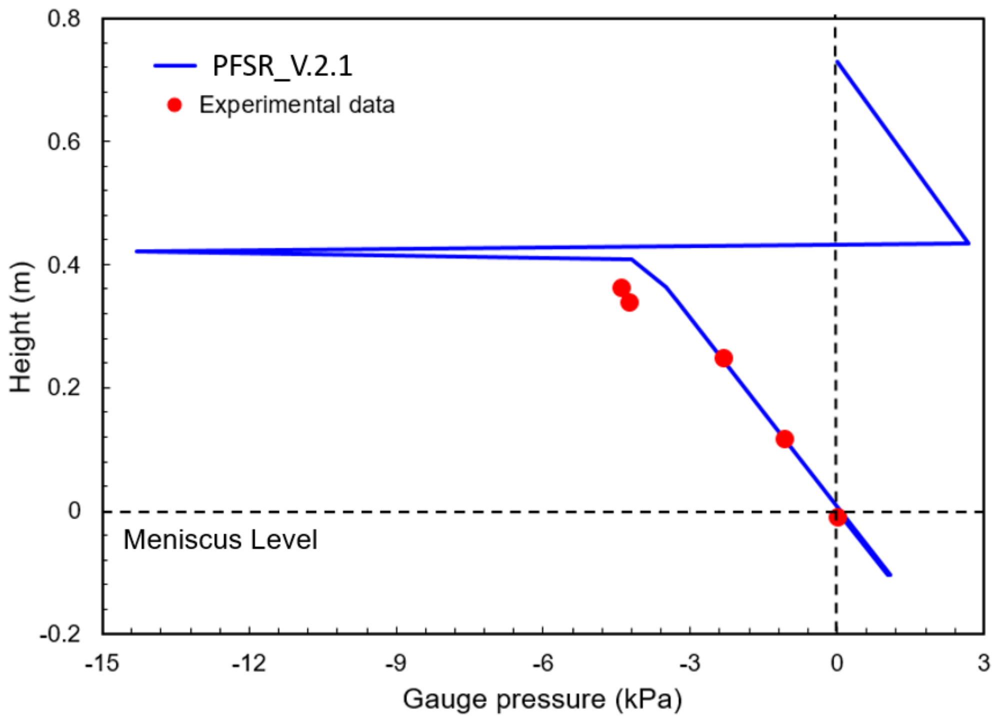

Figure 4.9 Pressure distributions validation of PFSR with experimental measurements for Nozzle 2 conditions.

.

4.3.4 Verification of PFSR with Water Model 3 and Plant 3 Data

Finally, PFSR predictions are verified and validated with both water model and plant measurements [36] for Nozzle 3 conditions. Water model 3 is a full 1:1 scale model of the Plant 3 geometry and all of the casting conditions are the same, given in Table 4.1. Stopper-rod opening was 10 mm. Figure 4.10 compares the pressure distribution calculated by PFSR with that of a 3D computational model with Fluent, using the $k-\omega$ shear-stress transport ($k-\omega$ SST) turbulence model [36]. The PFSR predictions match fairly well with the CFD simulations. In addition, Figure 4.10 shows that PFSR matches better with water model experimental measurements [36] rather do the CFD simulation results [36].

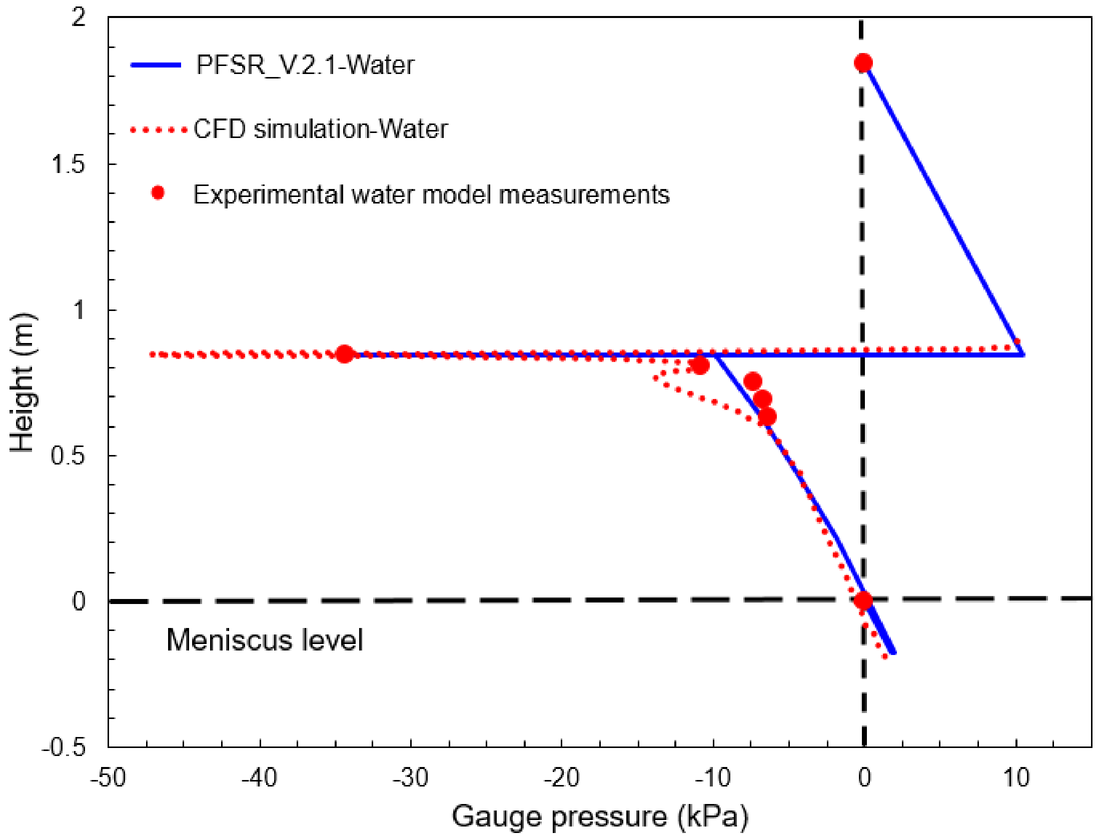

Figure 4.10 PFSR verification and validation with Nozzle 3 water model conditions.

Pressure predictions from PFSR and the CFD model are next compared in Figure 4.11 for the Plant 3 (Nozzle 3) casting conditions, with 10 mm stopper-rod opening. The PFSR model predictions match fairly well with the CFD simulations. In addition, the water model measurements are scaled to estimate pressure in the steel caster (real caster measurements of pressure were not available), by multiplying the steel/water density ratio of 7. Again, the two simulations match reasonably with each other and with the scaled measurements, which again verifies the model.

Note that in both PFSR and the CFD models, the minimum pressure, which occurs in the gap, is more negative than the minimum possible gauge pressure of -101.325 kPa for a perfect vacuum. This means that this predicted pressure is non-physical, that both models are incorrect, and that other phenomena must be introduced to correct the problem.

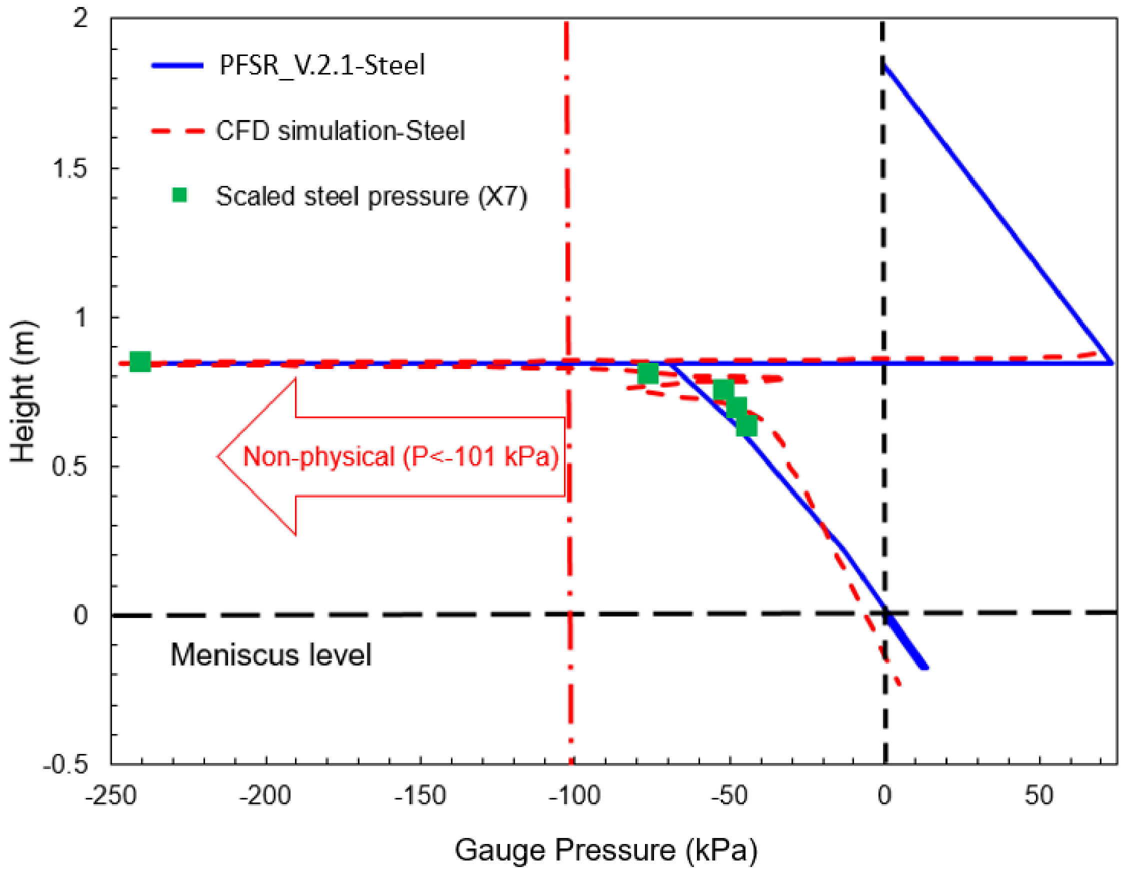

Figure 4.11 PFSR verification with Nozzle 3 plant conditions (10 mm stopper opening).

Finally, the PFSR and CFD model predictions [36] of the flow rate variation with stopper-rod vertical position are compared in Figure 4.12 with the water model 3 measurements (again scaled 7-fold) and with actual measurements in the plant 3 steel caster.

As expected, the PFSR predictions match well with those of the CFD simulation and with the scaled water model 3 measurements. However, the real plant measurements disagree with all three of these sets of data. Even the full-scale water model measurements disagree with the plant 3 measurements. The minimum gauge pressures predicted by PFSR are less than -101 kPa (and therefore non-physical) for the entire range of stopper-rod movement from 1 to 17mm. These findings agree exactly with the previous work by Liu et al. [36]. They confirm that other phenomena must be included into to the model in order to capture the flow and pressure behavior in the real steel plant for these conditions.

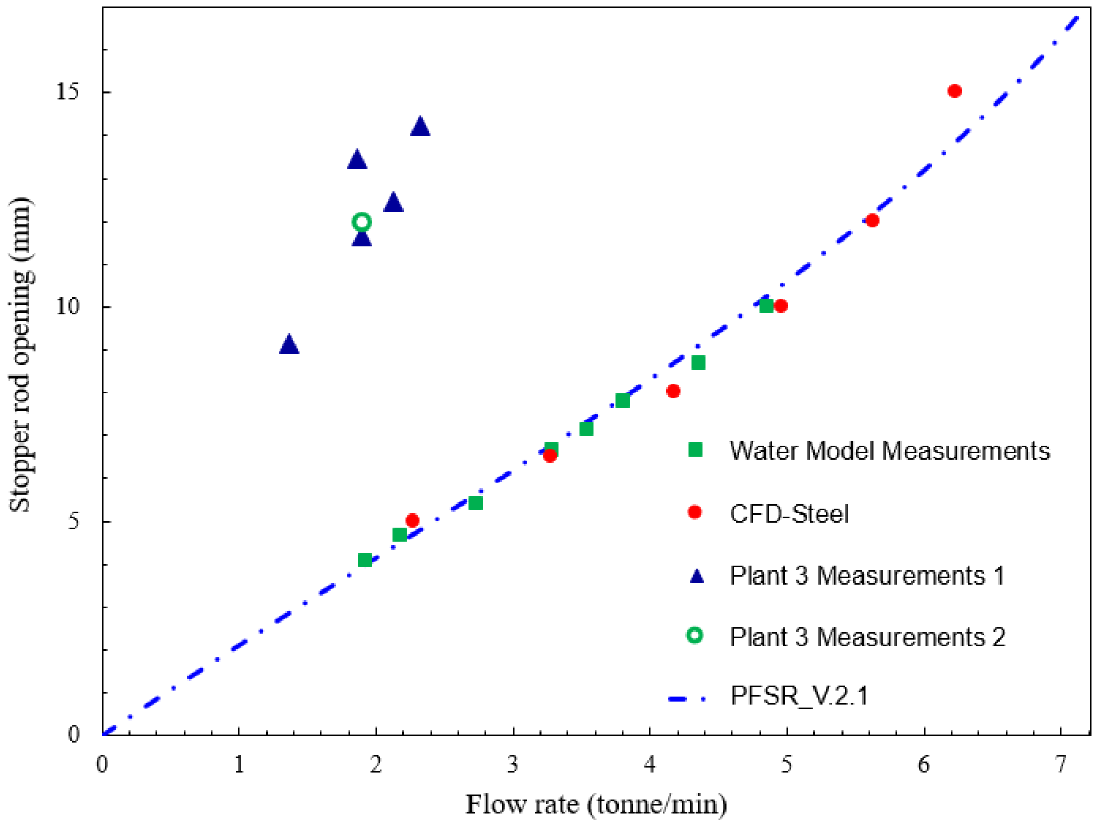

Figure 4.12 PFSR flow prediction comparison with Plant 3, CFD simulation, and water model 3 measurements.

4.4 Other Phenomena in Stopper-rod Flow

Although PFSR V.2.1 has been verified with CFD simulations (both water model and steel plant) and validated with water model experimental data, its minimum pressure prediction is unphysically low, ($P < -101.325$ kPa), for steel caster plant 3. As discussed in the previous section, CFD simulations and water model measurements have the same problem. This serious problem arises because there are physical phenomena left out of these models. This section introduces two new phenomena into the model system to overcome this problem: 1) non-primed flow/waterfall behavior and 2) cavitation. Each of these phenomena will be introduced, followed by introduction of a new methodology to implement them into PFSR.

4.4.1 Primed vs Non-Primed Flow

Two different types of flow are possible in stopper-rod nozzles with or without argon gas injection [78, 79]. The first, illustrated in Figure 4.13(a), is “primed flow” where any gas in the system, such as injected or introduced via refractory leaks, generates “bubbly flow”, where there is continuous fluid or fluid/gas mixture phase in the system and no air pockets. Primed flow is able to sustain pressure drops, according to Equation 4.1.

The second flow type is "non-primed" flow, or slug flow, which involves large air pockets. When argon gas is injected through the stopper tip, the non-primed flow is called "annular" flow, where molten steel enters the upper UTN through the annular-shaped gap and then flows down along the nozzle walls, while argon gas fills the center of the nozzle cross section [79]. As shown in Figure 4.13(b), large air pockets form beneath the stopper top in the central region of the nozzle, which move chaotically with the turbulent flow. Non-primed or annular flow tends to be very unstable and periodic [79], which likely leads to subsequent problems in mold flow and surface quality problems. Other gas sources include argon injection at other locations, leakage through joints or cracks in the refractory, or even degassing of elements such as carbon in the molten steel due to the very low pressure in the gap, cavitation [80]. Non-primed flow can occur along the entire length of the nozzle, depending on the flow conditions. It is most common in local portions of the nozzle, especially near the stopper tip, where pressure is lowest. It typically transitions to continuous bubbly flow part way down the nozzle, often at a sharp interface, which may wander around. Non-primed flow cannot sustain a pressure change over some vertical distance, as it contains a continuous gas phase which quickly flows to alter its shape and maintain a roughly constant pressure within the non-primed volume. This behavior is now implemented into the PFSR model as a new phenomenon.

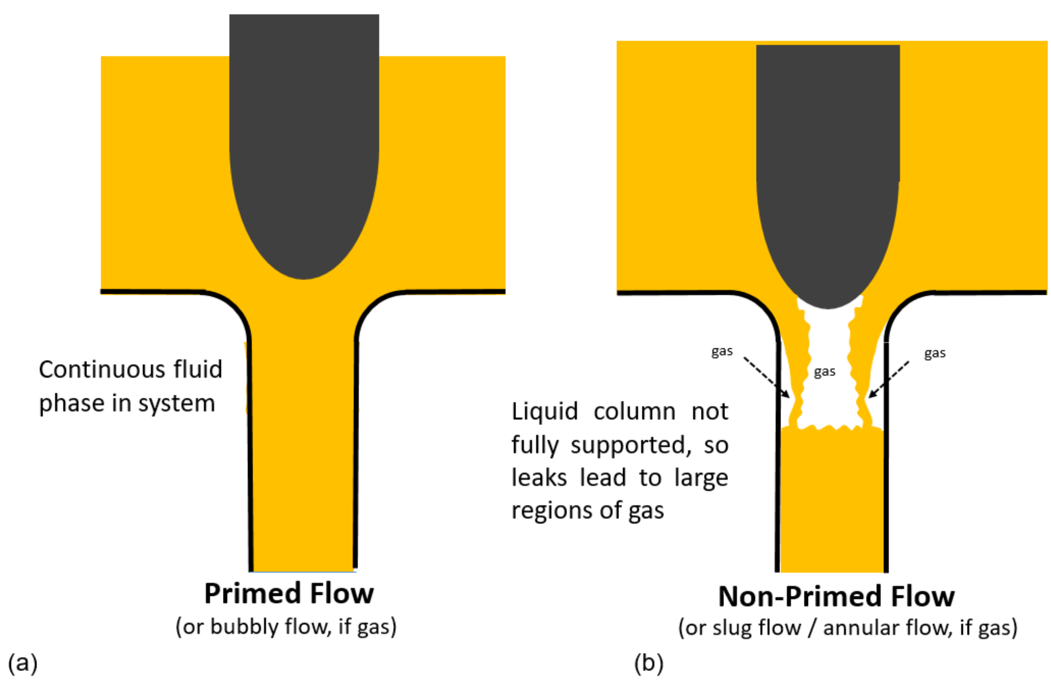

Figure 4.13 Schematic of (a) primed and (b) non-primed flow in stopper-rod systems.

4.4.2 Cavitation

A second possible explanation for the unphysically low-pressure predictions is neglecting the phenomenon of gas cavitation. As the local pressure decreases to become very low, dissolved gases in a liquid will exceed their solubility limits [74, 80] to nucleate bubbles in the lowest pressure regions of a flow system [74]. In molten steel, dissolved gases, such as nitrogen, hydrogen, and carbon monoxide, may form gas bubbles near the stopper-rod (point 3 in Figure 4.16) if their solubility limits are exceeded. This may occur in the lowest pressure regions, such as the lower portion of the narrow gap between the stopper-rod and the tundish floor. These evolved gas bubbles then may expand in these low-pressure regions, to take up space, causing the stopper-rod opening to increase, (such as observed in Figure 4.12). The cavitated bubbles likely re-dissolve lower inside the UTN or SEN, where the pressure increases. This re-dissolution step often occurs as a sudden collapse, which may cause erosion of adjacent surfaces [80], but this behavior was not investigated here.

4.4.2.1 Solubility of Gases in Liquid Steel

Solubility of the gasses like nitrogen, hydrogen, and carbon monoxide in molten steel is governed by Sieverts' law [81], which is expressed as:

$$k = \frac{C_g^2}{P_g} \tag{4.55}$$

where C_g is the concentration of atomic gas dissolved in the molten metal $[\frac{g_{solute}}{g_{solution}}]$, and P_g is partial pressure of that gas inside the bubble in equilibrium with the adjacent solution $[Pa]$. The equilibrium constant for the reaction from dissolved gas to nucleated gas bubble, k, depends on temperature and activation energy according to the classic Arehnius relation [82]:

$$k = A\exp(-\frac{E_a}{RT}) \tag{4.56}$$

where A is a fitted constant, E_a is the activation energy $[J/mole]$, R is the universal gas constant $[8.314\frac{J}{moleK}]$ [83], and T is the absolute temperature $[K]$. Combining Equation 4.55 into Equation 4.56 and rearranging gives:

$$\log C_g = -\frac{A^{'}}{T} + B + \frac{1}{2}\log P_g \tag{4.57}$$

where $A^{'}$ and B are empirical constants for a given gas dissolved in a given medium [84–86]. For the case of nitrogen gas dissolved in molten steel, Equation 4.56 is [84]:

$$\log(C_N) = -\frac{255.6}{T} - 1.26 + \frac{1}{2}\log P_{N_2} \tag{4.58}$$

where C_N is dissolved atomic nitrogen concentration given in the molten steel $[ppm]$, and P_{N_2} is the partial pressure of nitrogen $[Pa]$.

Similarly, for hydrogen [87]:

$$\log C_H = -\frac{1905}{T} - 1.591 + \frac{1}{2}\log P_{H_2} \tag{4.59}$$

where C_H is hydrogen dissolved concentration in $[ppm]$, and P_{H_2} is partial pressure of hydrogen in $[Pa]$. Figure 4.14 shows how the maximum concentrations of nitrogen and hydrogen that can dissolve in the molten steel varies with the partial pressure of the gases at different temperatures.

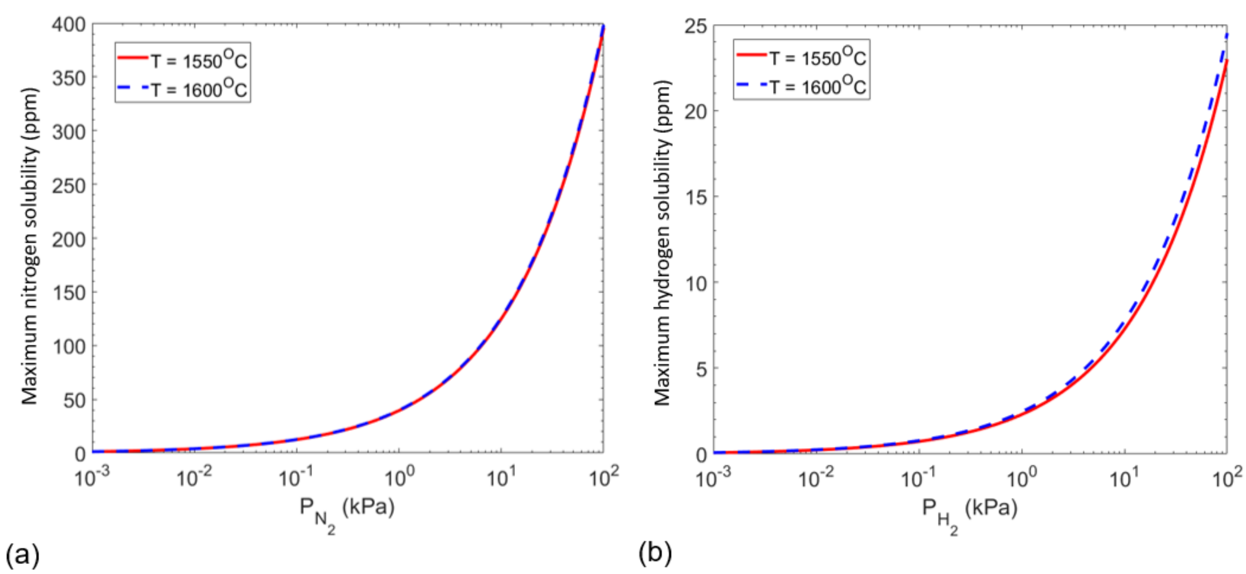

Figure 4.14 Gas solubility in molten steel at different temperatures of (a) Nitrogen (b) Hydrogen [84, 87].

4.4.2.2 Variation of Gas/Steel Flow Rate with Pressure at Different Gas Contents

Knowing the solubility equations in the previous section and the local pressure, the amount of gas cavitated into bubbles, $C_{g,cav}$, can be calculated from the total (original) dissolved gas content of the steel ($C_{g,total}$), and the remaining (equilibrium) dissolved gas ($C_{g,diss}$), from the mass balance:

$$C_{g,cav} = C_{g,total} - C_{g,diss} \tag{4.60}$$

The cavitated gas, $C_{g,cav}$, can become nonzero only upon super saturation, when the pressure drops sufficiently that the total dissolved gas content exceeds the equilibrium content from Equation 4.56, so $P_{g,diss} = P_{g,cav} = P_3$ $[Pa]$, (assuming only one supersaturated gas in the system). The above equations also require the neglect of nucleation kinetics.

The volumetric flow rate of cavitated gas, $\dot{V}_g$, is then calculated from the ideal gas law [83]:

$$\dot{V}_g = \frac{RT\dot{m}_g}{M_g P_{g,diss}} \tag{4.61}$$

where $\dot{m}_g$ is cavitated gas flow rate in $[\frac{kg}{s}]$, and M_g is the cavitated gas molar mass $[\frac{kg}{mole}]$, found from:

$$\dot{m}_g = \dot{m}_{steel} C_{g,cav} \tag{4.62}$$

in which:

$$\dot{m}_{steel} = \rho_{steel} \dot{V}_{steel} \tag{4.63}$$

where $\dot{m}_{steel}$ is molten steel mass flow rate in $[\frac{kg}{s}]$, ρ_{steel} molten steel density in $[\frac{kg}{m^3}]$, and $\dot{V}_{steel}$ molten steel volumetric flow rate in $[\frac{m^3}{s}]$. Substituting Equation 4.62 and 4.63 into Equation 4.61:

$$\dot{V}_g = \frac{RT\rho_{steel}\dot{V}_{steel}C_{g,cav}}{M_g P_{g,diss}} \tag{4.64}$$

Finally the flow rate ratio, r, of cavitated gas and total flow rate in the system, is:

$$r = \frac{\dot{V}_g}{\dot{V}_g + \dot{V}_{steel}} \tag{4.65}$$

The flow rate ratios calculated with Equation 4.65 for both nitrogen and hydrogen are plotted in Figure 4.15 as a function of local pressure at 1550^{o}C for different initial gas contents.

Figure 4.15 shows that above the critical pressure, cavitation flow rate is naturally zero for all curves (scenarios) plotted. As an example for 10 *ppm* nitrogen, the absolute pressure in Figure 4.15(a) must drop below the small value of 0.06 kPa to allow any cavitation. This figure also suggests that flow rate likely becomes unstable near the critical pressure, owing to the significant increase in gas flow over a very narrow pressure range. In all six scenarios, as soon as the pressure drops below the critical pressure, the flow rate ratio approaches 100 pct, so almost all of the gap area is filled with nitrogen or hydrogen. This would require the stopper-rod to lift suddenly to maintain the liquid steel flow rate, with accompanying unstable flow and quality problems.

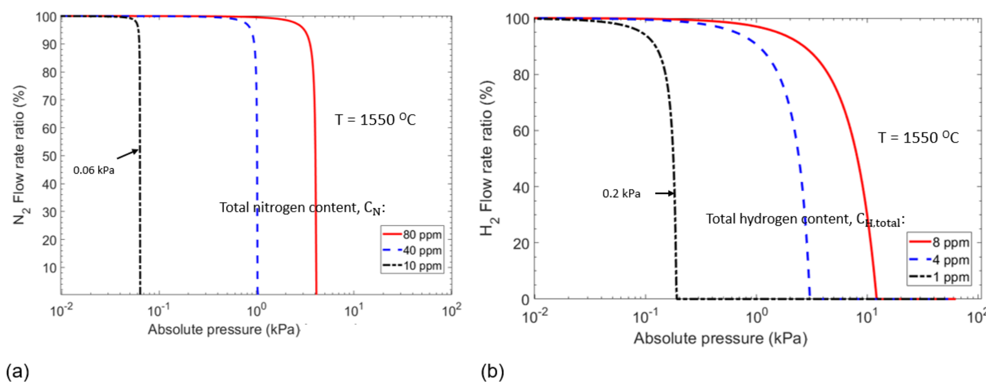

Figure 4.15 Variation of the cavitated gas flow rate with the pressure at different total gas contents at 1550^{o}C for (a)nitrogen (b)hydrogen.

4.4.3 Non-primed Flow/Cavitation Methodology

To incorporate the non-primed flow and cavitation phenomena described in the previous section (assuming only nitrogen as a cavitated gas in the system), a new version of the model, PFSR V.3.0, is introduced. Thus, in cases where PFSR V.2.1 predicts pressure at point 3 below -101.325 kPa, steps are taken to correct the problem, by introducing cavitation, non-primed flow, or both.

First, to introduce cavitation, Equation 4.58 is applied to calculate the equilibrium critical partial pressure of the given gas (e.g. nitrogen) at the given initial gas content in the steel:

$$P_{N_2} = (\frac{C_{N,total}}{10^{(-1.26-\frac{255.6}{T})}})^2 \tag{4.66}$$

where $C_{N,total}$ is the total dissolved content of nitrogen in molten steel before cavitation $[ppm]$.

Next, a small amount of cavitation is introduced by fixing the minimum pressure (point 3) to slightly below the critical pressure, and the new gas equilibrium pressure, cavitated gas pressure or P_{cav} in $[Pa]$, is calculated:

$$P_{cav} = P_{N_2} - p_x[Pa] \tag{4.67}$$

where "p_x" $[Pa]$ is the small pressure increase from the actual cavitated pressure to the critical pressure where the dissolved gas is at equilibrium and starts to evolve.

Having the cavitation pressure, the still-dissolved content of the nitrogen with the new pressure, P_{cav}, is calculated using Equation 4.58 replacing C_N with $C_{N,diss}$, still-dissolved content of nitrogen in molten steel, and also replacing P_{N_2} with P_{cav} in the equation.

Now the cavitated amount of gas can be calculated using Equation 4.60. Then using Equation 4.64 and Equation 4.65, the cavitated gas flow rate, $\dot{V_{N_2}}$, and the flow rate ratio, r, are determined.

The two variables estimated so far from the calculations are P_{cav} and r. P_{cav} is used to ensure the pressure at minimum gap, P_3, does not reach below its value. The flow rate ratio is used to make sure the area increases in the minimum gap due to cavitated gas that ultimately causes the stopper-rod to lift up and maintain the flow rate.

Now, the simplified non-primed/cavitation methodology can describe the pressure distribution in annular/slug flow conditions, as shown in Figure 4.13(b) in the stopper-rod system. The governing equations, the Bernoulli energy-balance approach, is almost the same as PFSR V.2.1 (Equation 4.2 to 4.11) and is developed for the 10 points shown in Figure 4.16.

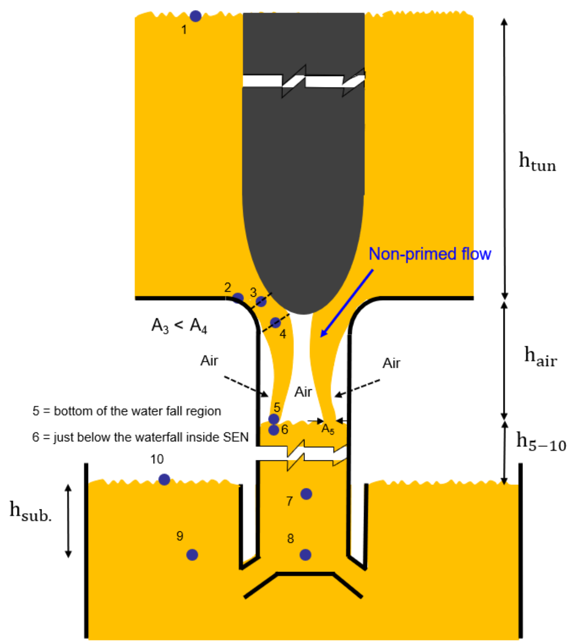

Figure 4.16 Schematic of the non-primed flow methodology.

There are, however several changes: 1) liquid density is used everywhere except in the gap, where due to cavitation and no argon gas injection, it is a mixture density, 2) at point 4 the maximum expansion of the flow occurs, 3) the pressure at point 5 is equal to the pressure at point 4 for the non-primed/cavitation methodology, due to the continuous gas phase in this region, which can quickly maintain a uniform pressure, and 4) since the pressure at point 5 and 4 must be equal and using the Bernoulli's equation, V_5 is calculated as:

$$V_5 = \sqrt{V_4^2 + 2gh_{air}} \tag{4.68}$$

in which h_{air} is the air pocket height in $[m]$ formed due to gas leakage (in the current work, although bubble coalescence is another mechanism in systems with argon injection) in the system and is calculated as an output along with the velocity at point 4, cavitation pressure, and other 10 pressures using the non-primed/cavitation flow model. All the 13 equations are solved simultaneously using FSOLVE with the two constraint equations, error of which must be very close to zero. The First one is the same as Equation 4.52 (which assures the pressure at point 1, P_1, is zero). The second one ensures that the minimum pressure in the gap at point 3, P_3, is the same as P_{cav} of the cavitated gas, and is define as follows:

$$F_2 = P_4 - \frac{1}{2}\rho_m V_3^2 + \frac{1}{2}\rho_m V_{UTNa}^2 + \Delta P_{L,exp} - P_{cav} \tag{4.69}$$

4.4.4 Solution procedure

Now that the non-primed/cavitation methodology is introduced, the solution procedure is explained for a general case and in the following section the application of PFSR V.3.0 is investigated for two special cases. FSOLVE for a general case, simultaneously solves 12 equations, which include 10 pressure equations (one for each of the 10 points) and two constraint equations: F(1) and F(2) = 0, involving 14 unknowns (the usual one missing casting condition, 10 pressure values for the 10 points, air pocket height, fluid velocity at point 4, and the cavitation pressure). To start the solution procedure, initial guesses are provided for the air pocket height, the velocity at point 4, and the cavitation pressure, which is achieved by making an initial guess for p_x and evaluating Equation 4.67. Having 14 unknowns and 12 equations means that to find a unique solution, there are two extra degrees of freedom to specify. Thus, the user must also provide any two from the following list of choices: the missing casting condition (so that all casting conditions are provided), air pocket height, velocity at point 4, cavitation pressure, or any other pressure in the system (ie. Pressure at points 2,5-9, such as from plant measurements).

4.4.5 Application of Non-primed Flow/Cavitation Model

The new PFSR V.3.0 with non-primed flow and cavitation was tested with plant measurements for the conditions of Nozzle 3 and 4, given in Table 4.1. Also, based on previous literature [88], a reasonable total nitrogen concentration in molten steel of 40 ppm is assumed for the initial dissolved concentration of nitrogen in the simulations.

Figure 4.17 shows the pressure distribution prediction of PFSR V.3.0 for Nozzle 3 conditions. Based on the real caster measurements [36] the back pressure is known to be -79 kPa, which is most likely to be measured in the air pocket region where pressure is relatively uniform. This provides one of the two extra equations required in this model. In order to force the pressure at point 4 to have the above value, the error in the following constraint equation must be very close to zero, in addition to constraint Equation 4.52 and 4.69, and is defined as follows:

$$F_3 = P_4 + 79000 \tag{4.70}$$

Additionally, the second extra equation needed is the stopper-rod opening distance, which was also measured at the plant. Knowing this parameter, the Nozzle 3 case has a unique solution, 14 equations and 14 unknowns, which is shown in Figure 4.17 for 3 different stopper-rod openings. In this way, the model is calibrated to match the stopper rod opening distance measured at the plant.

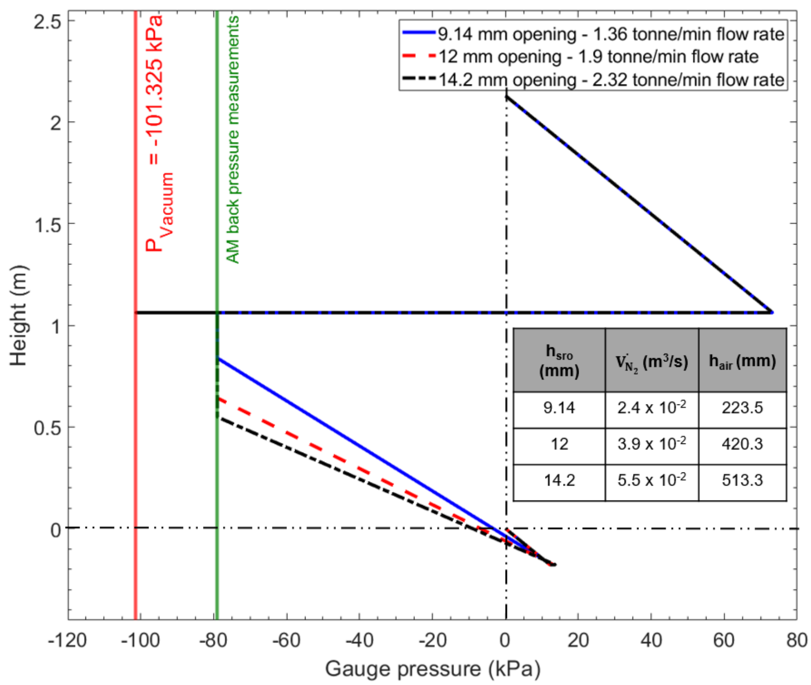

Figure 4.17 Pressure distribution for different openings using non-primed flow/cavitation methodology (PFSR V.3.0 Nozzle 3 conditions).

Furthermore, flow rate relation with stopper-rod opening for nozzle 3 using PFSR V.3.0 is shown in Figure 4.18. It can be seen from the figure that using the combination method seems to capture additional physics, specifically the cavitation and the air pocket height.

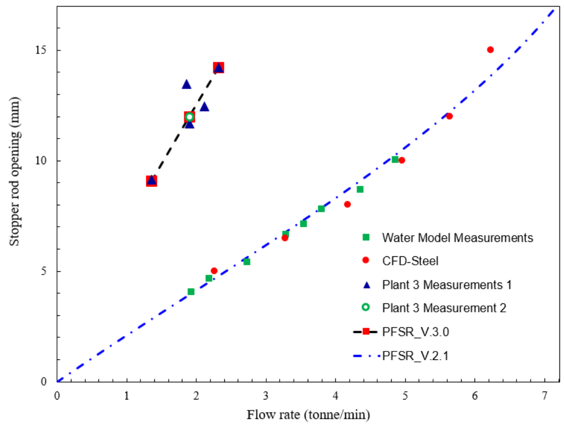

Figure 4.18 Flow rate-stopper-rod relation prediction of non-primed/cavitation methodology -Nozzle 3.

In the case of Nozzle 4, we have measurements to satisfy only one of two extra equations needed, which are the measured stopper rod openings for each flow rate (giving 13 equations and 14 unknowns). So, there is still one degree of freedom needed for the solution. As an example for the stopper rod opening of 1 mm (and 0.28 tonne/min), the air pocket height is treated as a known parameter to generate unique solutions, while calculating the other unknowns: velocity at point 4, cavitation pressure, and the 10 pressures. Four possible pressure distributions are shown in Figure 4.19.

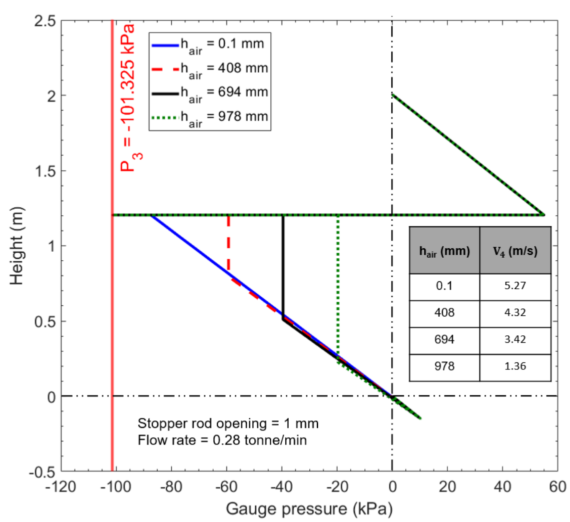

h_{air} (mm)	V_4 (m/s)
0.1	5.27
408	4.32
694	3.42
978	1.36

Figure 4.19 Pressure distribution comparison of different solutions for [1 mm stopper-rod opening, 0.28 tonne/min flow rate] using non-primed/cavitation flow methodology (PFSR V.3.0) -Nozzle 4 conditions.

According to Figure 4.19, there is a potential solution with virtually zero air pocket height (i.e. only cavitation). At the other extreme, the maximum air pocket height possible is 978 mm. Finally, for all four cases the amount of cavitation (and the minimum pressure, P_3) is constant, which are $6.38\times10^{-4}\ m^3/s$, and -101.201 kPa, respectively. Again, due to calibration of PFSR V.3.0, the predicted stopper-rod openings along with their flow rate exactly match with experimental data (measured stopper-rod opening and flow rate) as shown in Figure 4.20.

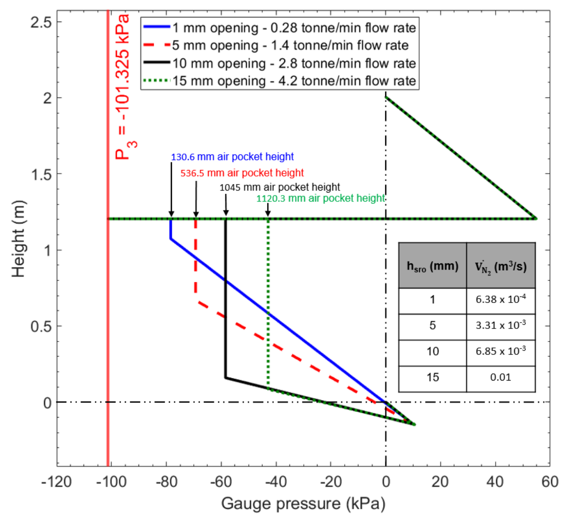

Figure 4.20 Pressure distribution comparison for different stopper-rod openings using non-primed/cavitation Flow methodology (PFSR V.3.0) -Nozzle 4.

Similar to nozzle 3, Figure 4.21 illustrates flow rate stopper-rod relation comparison of PFSR V.3.0 with the calibrated stopper-rod opening with flow rate measurements based on casting speed and section size in a commercial caster for nozzle 4. It is shown that an exact match can be reached using the combined model.

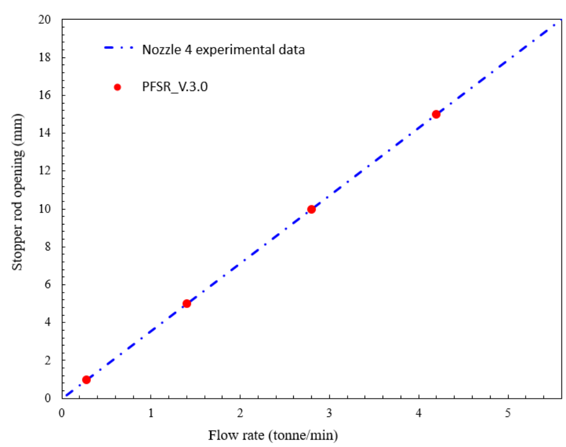

Figure 4.21 Flow rate-stopper-rod relation validation non-primed/cavitation methodology (PFSR V.3.0) -Nozzle 4.

Based on the results illustrated in this section, it seems obvious to conclude that there is certainly cavitation in the gap region of commercial casters. In addition, there is likely a significant air pocket, for most casting conditions. This is a significant finding emphasizing on the importance of the PFSR V.3.0 application to understand the behavior of the fluid flow in commercial casters.

4.5 Conclusion

This chapter presents a new, standalone, user-friendly MATLAB-based graphical user interface program, Pressure-drop and Flow-rate in stopper-rod systems (PFSR). The new model solves a one-dimensional system of Bernoulli equations for the pressure distribution and flow rate in stopper-rod nozzle systems for argon-molten steel flow systems including argon gas expansion (varies locally with pressure). The PFSR V.2.1 model has been verified with CFD simulations and validated with measurements in both water models and commercial plant data for steel continuous casters. The maximum error associated with the validation cases is approximately 8 pct.

To overcome non-physical predictions for some situations in real steel casters, an improved version of PFSR, V.3.0, is introduced, which includes the phenomena of non-primed flow and cavitation. This methodology introduces two degrees of freedom and in order to get a solution, two other variables must be fixed. The two variables can be chosen from the list below However if two of the below choices are given PFSR V.3.0 is able to yield to a unique solution:

- Air pocket height
- Velocity at maximum expansion point after minimum gap area
- Cavitation pressure
- Any measured (in the plant) pressure
- Any one of the casting conditions

Fixing one (or more) variable according to a plant measurements and running parametric studies on the other variable (if needed) to explore the solution space is a reasonable way to apply the current model, as demonstrated here. As for two special cases, PFSR V.3.0 is applied to capture the real physics in the plant. It is observed that in one of the cases (Nozzle 3) a unique solution is possible. However for Nozzle 4 case, still there is one degree of freedom for the solution.

Finally, cavitation is proven to be a phenomena that is certainly happening in commercial casters along with the possibility of the air pocket formation in some portion of the nozzle. This model system is ready to apply in future work to investigate pressure drops and flow rates in many real continuous casting systems with stopper-rod flow control systems. Further work is needed when cavitation and/or non-primed flow are present.

CHAPTER 5

THERMO-MECHANICAL BEHAVIOR OF SOLIDIFYING SHELL INSIDE THE MOLD AND THE EFFECT OF TURBULENT FLOW ON THE GROWTH

Modified from a paper to be submitted to The Journal of Materials Processing Technology.

Hamed Olia[15,16], Seong-Mook Cho[17], B. G. Thomas[18,19]

In this chapter, a transient two-dimensional (pseudo 1-D) model is introduced to include the effect of turbulent flow on the thermo-mechanical behavior of the solidifying shell inside the mold in the continuous casting of steel. The new model is able to predict the temperature distribution, shell growth, and mechanical properties of the solidifying shell while the effect of superheat flux, which is delivered to the solidification front from the mold fluid flow, is considered for the steel with different carbon contents. The new method using which the thermo-mechanical properties are calculated is Enhanced Latent Heat of fusion, ELH, and is applied as a subroutine to ABAQUS. After developing the model, the model is verified and validated by the existing models and the experiments. Finally, a case study is conducted to investigate the effect of the turbulent flow passing through clogged and non-clogged ports on the thermo-mechanical behavior of the solidifying shell inside the mold. It is concluded that the mold heat flux plays a more important role compared with the superheat flux on determining the thermo-mechanical behavior of solidifying shell.

5.1 Introduction

One of the most exciting areas of the research has been solidification modeling in continuous casting of steel. Characterization of the fluid flow and heat transfer, which are coupled phenomena is very important in continuous casting of steel. The significance of the process is laid in the momentum of the flow leaving the nozzle into the liquid steel mixed with the turbulent re-circulation zone caused by the thermal buoyancy. The combined effect may influence the process by changing the solidification rate, slag entrainment, shell thinning, etc. The earlier studies have been conducted on mathematical modelling of simultaneous fluid flow and heat transfer in continuous casting. Szekely et al. [89] investigated the interaction of heat and fluid flow in the continuous casting of steel in the mold. Based on the results, the solidus line is not the function of the flow pattern in the molten steel, although the superheat effect is

[15]Graduate student at the Colorado School of Mines
[16]Primary researcher and author
[17]Assistant Professor at Department of Metallurgical Engineering, Pukyong National University
[18]Full Professor at the Colorado School of Mines
[19]Author for correspondence

sensitive to the former. Szekely et al. [90] also developed a stream function-vorticity based model procedure along with a simplified model of turbulence to calculate heat transfer and fluid flow in continuous casting of steel. The results when compared with water model experiments showed good quantitative agreement between the theory and experiments. On the other hand, there are some early studies conducting only heat transfer analysis which included the effect of the turbulent flow. For example Lait et al. [91] and Brimacombe [92], incorporated conduction-only heat transfer with a relatively larger and effective thermal conductivity to account for the fluid flow inside the mold with which temperature profiles and shell thickness are computed. However, later, it is shown that the assumption of the effective conductivity is not accurate enough, at least not always. This is discussed and confirmed first by Mazumdar et al. [93]. Additionally, Choudhari et al.[94] concluded that if the range of effective conductivity exceeds a certain value, then the shell prediction is no longer accurate. If the value gets even bigger in some cases the simulation does not even yield to any solidification formation inside the mold. The mentioned problem caused the studies to be more focused toward the coupled simulation of fluid flow and heat transfer. Lee et al. [95] using a fully coupled analysis of fluid flow, heat transfer, and deformation behavior of a solidifying shell, tried to predict the crack formation in a continuously cast beam blank. Through coupling Finite Volume Method (FVM) with Finite Element Analysis (FEA), they calculated the heat flow between strand and the mold wall and could predict the shell development retardation (thinning) due to the jet impingement which was matched by the experiment. Another similar study was conducted by Tekeredzic et al. [96] to simultaneously predict the phase change, heat transfer, deformation, and stress determination in solid, and liquid parts of the domain. The results also were verified and validated using the existing analytical and experimental data, respectively. The similar investigations to the former two studies, can still be both timely and costly challenging for the researchers. To address the mentioned problem easier there are some studies aiming at solving for the thermal-fluid simulation first and then applying the stress analysis [97–100]. Although, the literature is comprehensive, many researchers actually did not consider the heat transfer shrinkage effect [101–105]. More recently, the issue is addressed in studies done by Koric et al. [106] and Zappulla et al. [107]. The fluid flow simulation can be reasonably decoupled from the thermal-stress analysis if one can estimate the liquid pool shape in advance [108]. Koric et al. [109] developed a user-defined thermal subroutine in ABAQUS [110] to account for the effect of superheat flux on the heat transfer behavior of solidifying shell. The model can calculate the excess of latent heat of fusion caused by the superheat flux for both low and high-velocity jet of the molten steel flow inside the mold. However, the model is not able to evaluate the effect of superheat flux on the thermal stress behavior of the solidifying shell. The model is only capable of handling constant heat transfer properties and the effect of different carbon content is not considered in the model.

This chapter investigates computational methods for solving heat conduction problems with solidification that can include the effect of the fluid flow by a “superheat flux”. This work is the continuation of the previous study [109]. The new model, built on the previous model [108], is able to use temperature-dependent thermal and mechanical properties as well as the ability to study the grade effect.

The model presents a new FORTRAN-based ABAQUS subroutine to calculate the effect of the superheat flux on heat transfer and thermo-mechanical stress and strain for both low and high-velocity jet of the flow inside the mold and near the solidifying shell for the steel with temperature-dependent thermal and mechanical properties. It is, then, verified with the existing models and validated with the experimental data. Finally, a case study is conducted in which the effect of the asymmetric turbulent flow caused by clogging in the port region is investigated on the thermo-mechanical behavior of a solidifying shell.

5.2 Model Description

In this section the computational domain, heat transfer, fluid flow, and stress governing equations, along with the solution procedures are described. To start with, the domain is assumed as a thin slice of solidifying steel through the shell thickness inside the mold, similar to what is introduced in Zappulla et al. [108], and is shown in Figure 5.1. The domain is considered to be far from the corners of the mold, ensuring the accurate contact against the wall and uniform solidification [108].

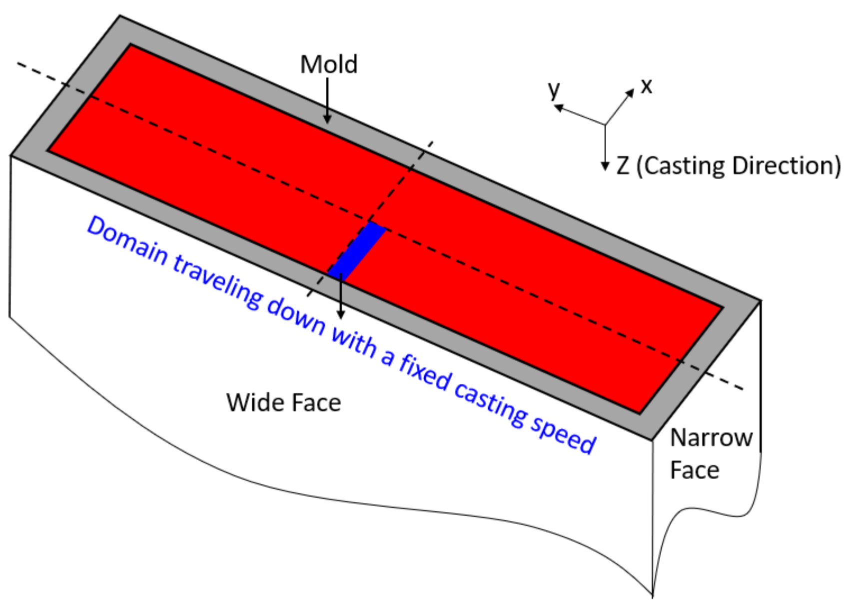

Figure 5.1 Thin slice of solidifying steel representing the simulation domain.

The Lagrangian approach is employed to the slice moving down the mold with a constant casting speed, since the advection force is more dominant with respect to the axial heat conduction (Péclet number) [108]. The simulation is a 2-D (2 dimensional) transient (one-way) coupled heat transfer-stress analysis and in the next subsections the governing equations along with the Enhanced Latent Heat, ELH, methodology are explained in details.

5.2.1 Heat Transfer Model

A transient 2-D energy equation is solved in the heat transfer section of the model to determine the temperature field of the domain as follows [108]:

$$\rho \frac{\partial H}{\partial t} = \nabla.(k \nabla T) \tag{5.1}$$

where ρ is the temperature-dependent density, H is temperature-dependent specific enthalpy in $[\frac{J}{kg}]$, t is time in $[s]$, k is isotropic temperature-dependent heat conductivity in $[\frac{J}{sKm}]$, and T is temperature in K.

5.2.1.1 Specific Enthalpy and Heat Capacity

The model utilizes the temperature-dependent function for calculating the specific enthalpy and heat capacity, C_p, for each phase based on the study done by K. Harste [111]. For the liquid phase:

$$H_L = 824.6157T - 104642.3 + \Delta H^L_{mix} \tag{5.2}$$

where:

$$\Delta H^L_{mix} = 18125(pctC) + 1966120 \frac{(pctC)^2}{43.839(pctC) + 1201.1} \tag{5.3}$$

where $pctC$ is the carbon weight percent for a specific steel. For δ-ferrite phase:

$$H_\delta = 0.08872T^2 + 441.3942T + 50882.26 \tag{5.4}$$

Finally, for γ-austenite phase:

$$H_\gamma = 0.0748901T^2 + 429.8495T + 93453.72 + \Delta H^\gamma_{mix} \tag{5.5}$$

where

$$\Delta H^\gamma_{mix} = 36601(pctC) + 1907930 \frac{(pctC)^2}{43.839(pctC) + 1201.1} \tag{5.6}$$

For the cases the phase is mixed, a weighted average is used according to the phase fractions [108]:

$$\Delta H = f_L H_L + f_\delta H_\delta + f_\gamma H_\gamma \tag{5.7}$$

where f_L,f_δ, and f_γ are liquid, δ-ferrite, and γ-austenite phase fractions, respectively. The specific enthalpy for a low carbon grade (0.045 pct) is plotted in Figure 5.2.

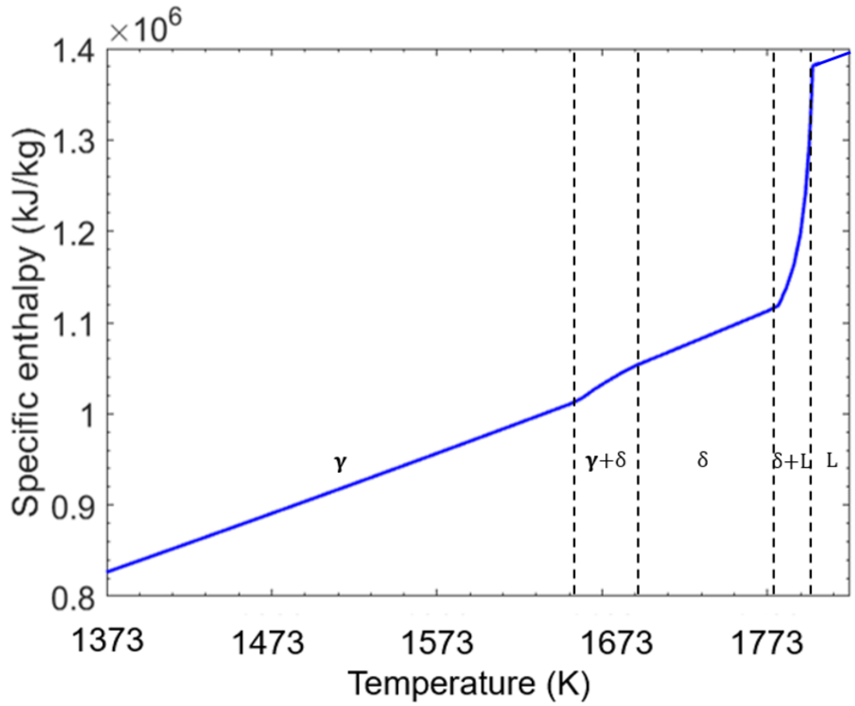

Figure 5.2 Variation of the specific enthalpy with temperature for low carbon (0.045 pct) steel.

It should be noted for specific heat, based on the definition, the equation for each phase is obtained by making the derivation of the specific enthalpy with respect to temperature [108], and the rule of mixture is also applied.

5.2.1.2 Thermal Conductivity

A thermal conductivity, k, graph which is a function of both temperature and carbon content is used in the model [108]. For the liquid phase:

$$k_L = 39 \tag{5.8}$$

For δ-ferrite phase:

$$k_\delta = (21.6 + 0.00835T(^OC))(1 - (F_1(pctC^{F_2}))) \tag{5.9}$$

where:

$$F_1 = 0.425 - 0.0004385T(^OC) \tag{5.10}$$

$$F_2 = 0.209 + 0.00109T(^OC) \tag{5.11}$$

For γ-austenite phase:

$$k_\gamma = 20.14 + 0.00931T(^OC) \tag{5.12}$$

Similar to specific enthalpy case for the mixture phase case, a rule of mixture is used to calculate the thermal conductivity. Figure 5.3 shows the variation of thermal conductivity with regard to the temperature for a low carbon grade (0.045 pct) steel.

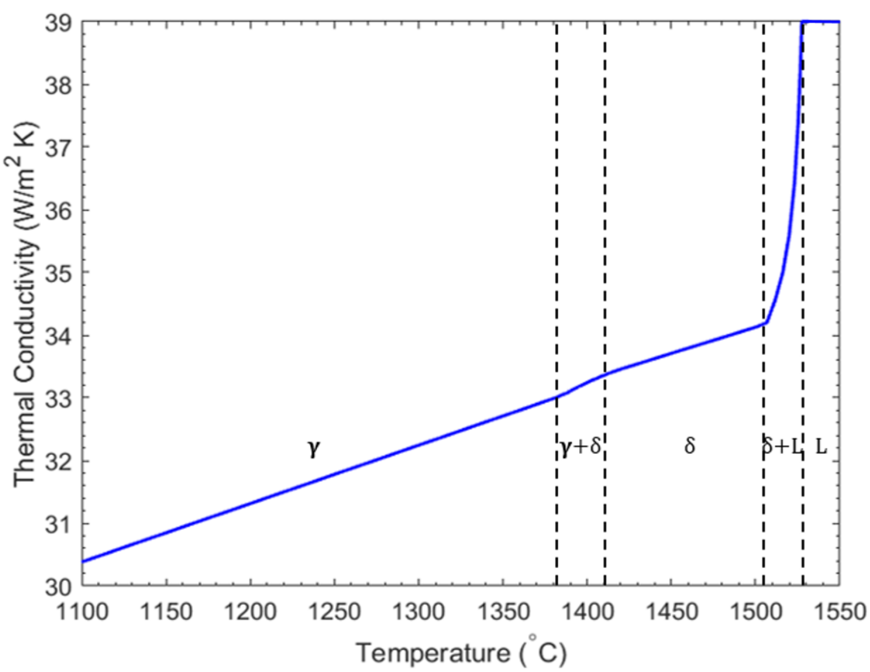

Figure 5.3 Variation of the thermal conductivity with temperature for low carbon (0.045 pct) steel.

5.2.1.3 Density

Like the cases for specific enthalpy and thermal conductivity, density in $[\frac{kg}{m^3}]$, is temperature and carbon-content dependent [108]. For the liquid phase:

$$\rho_L = 7100 - 73.2(pctC) - (0.828 - 0.0874(pctC))(T(^OC) - 1550) \tag{5.13}$$

For δ-ferrite phase:

$$\rho_{\delta} = \frac{-0.4724T(^{O}C) + 8010.71}{(1 - 0.01(pctC))(1 + 0.01343(pctC))^{3}} \tag{5.14}$$

For γ-austenite phase:

$$\rho_{\gamma} = \frac{-0.5091T(^{O}C) + 8105.91}{(1 - 0.01(pctC))(1 + 0.008317(pctC))^{3}} \tag{5.15}$$

similarly, for the mixture phase, the rule of mixture is used to calculate the density of the mixture and Figure 5.4 shows its variation as a function of temperature for low carbon steel.

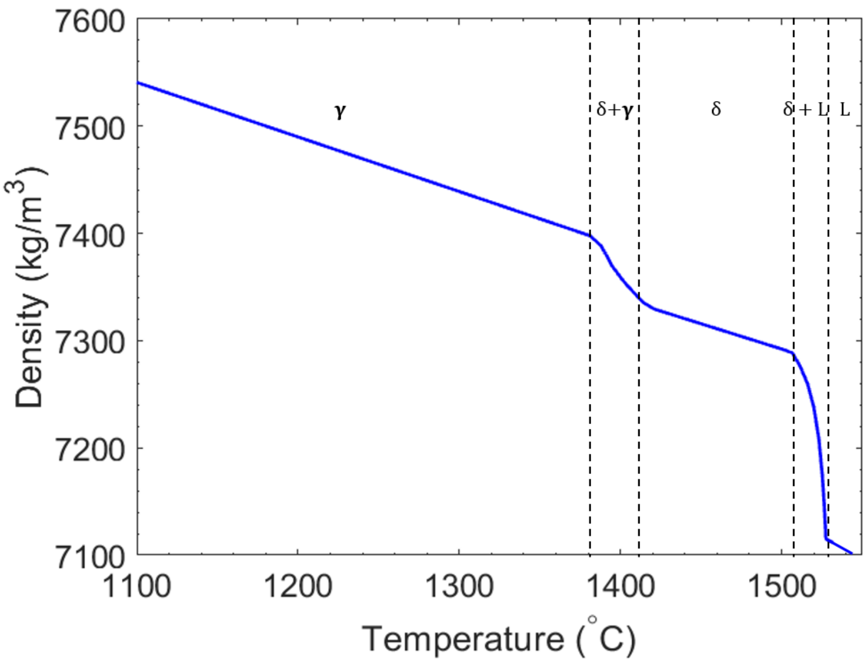

Figure 5.4 Variation of the steel density with temperature for low carbon (0.045 pct) steel.

5.2.1.4 Thermal Linear Expansion

Next, the isotropic thermal linear expansion (TLE) is a function of density (which in turn is both temperature and carbon content dependent) and is defined as [108]:

$$TLE = \sqrt[3]{\frac{\rho(T_0)}{\rho(T)}} - 1 \tag{5.16}$$

where $\rho(T_0)$ in the model is the density at reference temperature of 1780 K (1507 ^{O}C), and $\rho(T)$ is evaluated based on the phase (or mixture of phases) defined above [108]. The variation of TLE with temperature is plotted for a low carbon steel and is depicted in Figure 5.5.

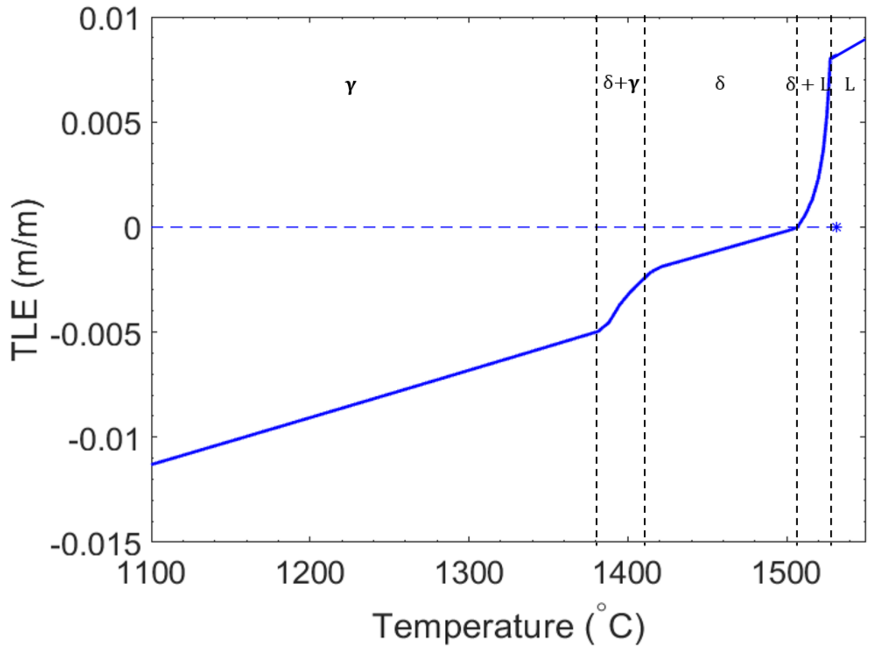

Figure 5.5 Variation of the steel TLE with temperature for low carbon (0.045 pct) steel.

5.2.2 Enhanced Latent Heat Method

In case there is superheat flux (whether a low or high-velocity jet, such as jet impingement case [109]) applied on the solidification front, its effect must be included to calculate the specific enthalpy of the domain and the following steps must be taken [109]:

- Estimating the proportionality constant, ϕ, to find the location of the solidification front in the domain using the following transcendental equation [109]:

$$\frac{(T_{liq} - T_{surf})C_{p,s}}{\sqrt{\pi}(H_f + (\frac{q^{"}}{\rho_s \sqrt{\alpha_s} \phi \frac{1}{\sqrt{t}}}))} = \phi \exp \phi^2 erf(\phi) \tag{5.17}$$

where T_{liq} is liquidus temperature and T_{surf} chilled surface temperature in K, $C_{p,s}$ is solid steel specific heat capacity in $[\frac{J}{kgK}]$, H_f is latent heat of fusion in $[\frac{J}{kg}]$ (will be explained later), $q^{"}$ is superheat flux in $[\frac{J}{sm^2}]$ (can be calculated for the low-velocity jet or be input for the high-velocity jet as the result of the previous fluid flow simulation), ρ_s is solid steel density in $[\frac{kg}{m^3}]$, α_s is solid steel heat diffusivity in $[\frac{m^2}{s}]$, and ϕ is proportionality constant. It is important to note that all the "solid steel" properties are evaluated around the solidus temperature, T_{sol}. By solving the above equation for ϕ, the next step is:

- Estimating solidification front velocity using [109]:

$$v = \sqrt{\alpha_s}\phi\frac{1}{\sqrt{t}} \tag{5.18}$$

having that, the model calculates the excess of the latent heat of fusion caused by the superheat flux [109]:

$$\Delta H_f = \frac{q^{"}}{\rho_s v} \tag{5.19}$$

Next is:

- Updating the old latent heat of fusion, H_f, due to superheat flux [109]:

$$H_{f,new} = H_f + \Delta H_f \tag{5.20}$$

where $H_{f,new}$ is the new updated latent heat of fusion.

- Calculating the enthalpy change with temperature using [109]:

$$(\frac{dH}{dT})^{t+\Delta t} = C_p(T) + H_{f,new}\frac{df_L(T)}{dT} \tag{5.21}$$

where $C_p(T)$ is the temperature-dependent specific heat capacity, and $f_L(T)$ is the temperature-dependent liquid phase fraction which is defined as [109]:

$$f_L(T) = \frac{T - T_{sol}}{T_{liq} - T_{sol}} \tag{5.22}$$

- Updating the specific enthalpy at the end of the time step [109]:

$$H^{t+\Delta t} = H^t + (\frac{dH}{dT})^{t+\Delta t}\Delta T \tag{5.23}$$

5.2.2.1 Latent Heat of Fusion Calculation

For the case there is superheat flux, latent heat of fusion, which is the heat released in the mushy zone (mixture of liquid and δ-ferrite), is calculated based on the following equation:

$$H_f = H_L(T_{liq}) - H_\delta(T_{sol}) - \int_{T_{sol}}^{T_{liq}} C_p(T)\, dT \tag{5.24}$$

It is important to note that $C_p(T)$ is calculated using Equation 5.2 through 5.5 by derivation of the enthalpy with respect to temperature.

5.2.2.2 Superheat Flux Calculation

The superheat flux can be calculated based on either a low-velocity jet of the flow or the high-velocity jet of the flow (caused by jet impingement). For the case of high-velocity jet, superheat flux is obtained using CFD simulation and is given as an input to the model. For the case of the a low-velocity jet of the flow, superheat flux can be calculated as a close form solution. To obtain the equation of superheat flux for this case, it is important to calculate first the temperature distribution inside the a low-velocity jet of the flow in the molten steel.

For a classical 1-D solid-controlled solidification the analytical temperature field as a function of distance and time is expressed as [112]:

$$T(x,t) = C_1 + C_2 erf(\frac{x}{2\sqrt{\alpha_s t}}) \tag{5.25}$$

Imposing the boundary conditions of $T = T_{surf}$ at $x = 0$ and $T = T_{liq}$ at $x = \delta(t) = 2\phi\sqrt{\alpha_s t}$ [112]:

$$\frac{T(x,t) - T_{surf}}{T_{liq} - T_{surf}} = \frac{erf(\frac{x}{2\sqrt{\alpha_s t}})}{erf(\phi)} \tag{5.26}$$

Finally, the temperature in the liquid ($T > T_{liq}$) is obtained then as [112]:

$$T(x,t) = \frac{1}{erf(\phi\sqrt{\frac{\alpha_s}{\alpha_l}}) - 1}[T_{init} erf(\phi\sqrt{\frac{\alpha_s}{\alpha_l}}) - T_{ref} + (T_{ref} - T_{init}) erf(\frac{x}{2\sqrt{\alpha_s t}})] \tag{5.27}$$

where T_{init} and T_{ref} are the initial temperature and the temperature at 90 percent of liquid phase fraction, respectively, in K, and α_l is liquid heat diffusivity in $[\frac{m^2}{s}]$. Finally, by derivation with respect to distance the superheat flux is calculated as [112]:

$$q^{"}(x,t) = -\frac{(T_{ref} - T_{init})\sqrt{k_L \alpha_L c_{pl}} \exp(-\phi^2 \sqrt{\frac{\alpha_s}{\alpha_l}})}{(erf(\phi\sqrt{\frac{\alpha_s}{\alpha_l}}) - 1)(\sqrt{\pi t})} \tag{5.28}$$

where k_L is thermal conductivity of the liquid in $[\frac{J}{sm^2k}]$ and c_{pl} is liquid specific heat capacity in $[\frac{J}{kgK}]$.

5.2.3 Fluid Flow Model

A three-dimensional (3D) turbulent finite-volume CFD and thermal model with an Eulerian frame of reference domain is used to determine the velocity and temperature field as well as superheat flux variation through casting direction for a bifurcated nozzle with the left port clogged and the right one non-clogged

[113]. The domain consists of the SEN nozzle interiors, ports, and the mold. The momentum and continuity equations governing the turbulent flow were solved with a Reynolds-Averaged Navier-Stokes (RANS) standard $k - \epsilon$ model for a coupled turbulent thermal fluid flow. The continuity equation for mass conservation is:

$$\frac{\partial}{\partial x_i}(\rho u_i) = 0 \tag{5.29}$$

where ρ is fluid density $[\frac{kg}{m^3}]$ and u_i is velocity in the 3 coordinate directions $[\frac{m}{s}]$. The Navier-Stokes equation for momentum conservation is:

$$\frac{\partial}{\partial t}(\rho u_i) + \frac{\partial}{\partial x_j}(\rho u_i u_j) = -\frac{\partial p^*}{\partial x_i} + \frac{\partial}{\partial x_j}[(\mu + \mu_t)(\frac{\partial u_i}{\partial x_j} + \frac{\partial u_j}{\partial x_i})] \tag{5.30}$$

where p^* is modified pressure ($p^* = p + \frac{2}{3}\rho k_r$) $[Pa]$, p is gauge static pressure $[Pa]$, k_r is an unknown residual kinetic energy, μ is dynamic viscosity of the fluid $[Pa.s]$, and μ_t is turbulent viscosity $[Pa.s]$. The details on the calculations of turbulent viscosity, turbulent kinetic energy (k), turbulent dissipation rate (ϵ) and the boundary condition assignments are explained elsewhere [113]. The initial condition, element type and size, solver, and convergence criteria are similar to those used in previous work [113].

5.2.3.1 Velocity and Temperature Contours

The velocity and the temperature contours as the result of coupled turbulent thermal fluid flow is shown in Figure 5.6.

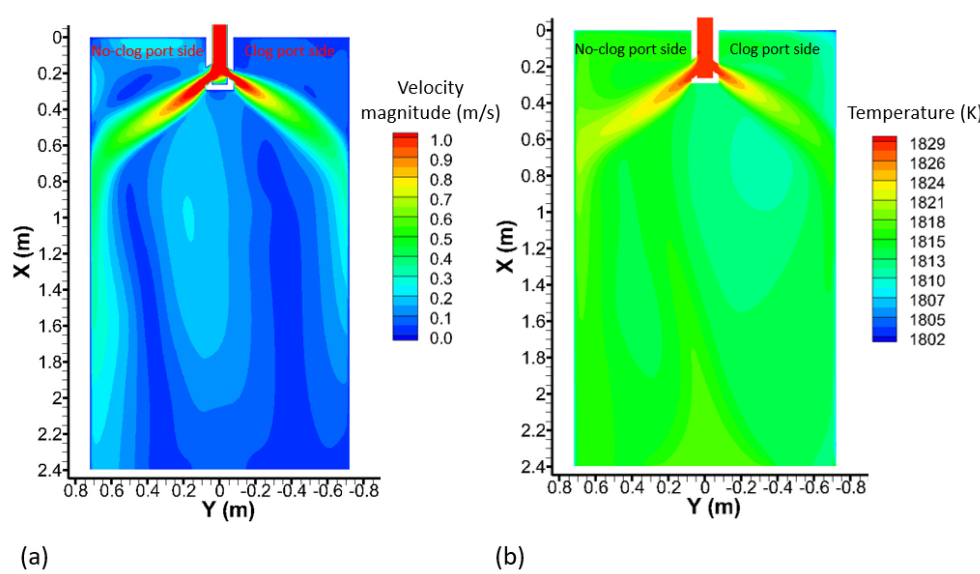

Figure 5.6 CFD simulation results, contours of a) velocity and b) temperature [113].

5.2.3.2 Mold Interface and Superheat Flux

The prescribed mold heat flux along with the superheat flux is shown in Figure 5.7.

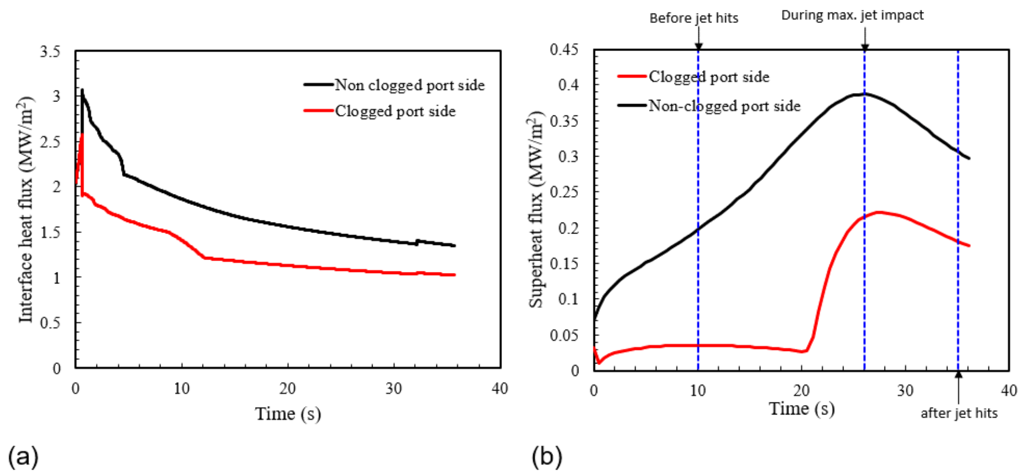

Figure 5.7 Prescribed a) interface heat flux and b) superheat flux for case study [113].

It is important to note that the results for temperature and stress distributions are studied for 3 different times (before, during, and after jet max. impact).

5.2.4 Phase Fraction

In the model the phase fraction is the function of temperature and the composition of steel. The specifics and details of how the phase fractions for a binary or three-phase region is calculated is discussed elsewhere [108]. For a low carbon grade (0.045 percent carbon) steel, the phase evolution with temperature is plotted in Figure 5.8.

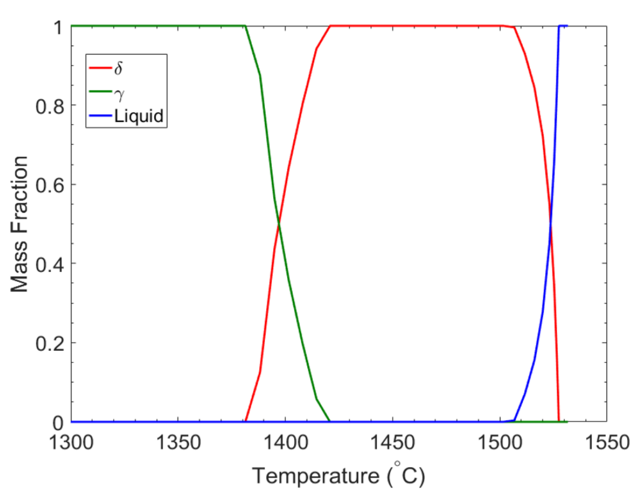

Figure 5.8 Variation of the phase fraction with temperature for low carbon (0.045 pct) steel.

5.2.5 Stress Model

Since it is reasonable to account for a small strain through the initial solidification, the mechanical governing equation of the solidifying strand can be expressed as [108]:

$$\nabla.\sigma + b = 0 \tag{5.31}$$

where σ is the second-order Causchy stress tensor, and b is the applied volumetric body force. It is important to note that for the current model the applied force is assumed to be zero. Also, the total strain rate, $\dot{\epsilon}$, in the model includes thermal, $\dot{\epsilon}_{th}$, inelastic, $\dot{\epsilon}_{ie}$, and elastic, $\dot{\epsilon}_{el}$, all in $[\frac{1}{s}]$, components such that [108]:

$$\dot{\epsilon} = \dot{\epsilon}_{th} + \dot{\epsilon}_{ie} + \dot{\epsilon}_{el} \tag{5.32}$$

5.2.5.1 Young's Modulus

For steel, Young's modulus is a temperature-dependent property. Figure 5.9 shows the relationship between Young's modulus used in the model and the temperature variation, which is independent of carbon contents in the steel [108].

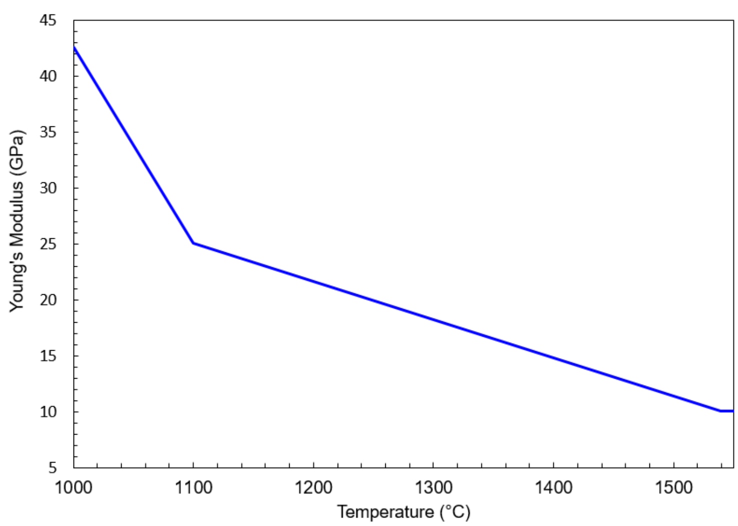

Figure 5.9 Variation of Young's modulus with temperature for steel.

5.2.5.2 Constitutive Equations

The stress and strain are related through the unified constitutive equation. In this model a visco-plastic constitutive model is used, which includes both strain-rate-independent plasticity as well as time-dependent creep [108]. It is worth mentioning that at high temperatures creep and inelastic strains can not be distinguished from one another [103]. The current model assumes an isotropic behavior for all the phases of the solidifying shell. As for the molten steel a very small and non-zero yield strength of 10 kPa is assumed. Although assuming a non-zero strength for the liquid phase might cause a small error to the model but it is necessary to avoid numerical singularity in the model [108]. For the δ-ferrite, Zhu modified power law [108] is used:

$$\dot{\epsilon}_{ie-\delta} = 0.1F_{\delta}|F_{\delta}|^{n-1} \tag{5.33}$$

where

$$F_{\delta} = \frac{C\bar{\sigma}}{f_C(\frac{T}{300})^{-5.52}(1+1000|\epsilon_{ie-\delta}|)^m} \tag{5.34}$$

in which

$$f_C = 1.3678 \times 10^4 (pctC)^{-5.56\times10^{-2}} \tag{5.35}$$

$$m = -9.4156 \times 10^{-5}T + 0.349501 \tag{5.36}$$

$$n = (1.617 \times 10^{-4}T - 0.06166)^{-1} \tag{5.37}$$

where C can take either 1 or -1 [108]. As an example, stress-inelastic strain relation is plotted for different temperature and $\dot{\epsilon}_{ie} = 10^{-4}\frac{1}{s}$ and low carbon content and is shown in Figure 5.10.

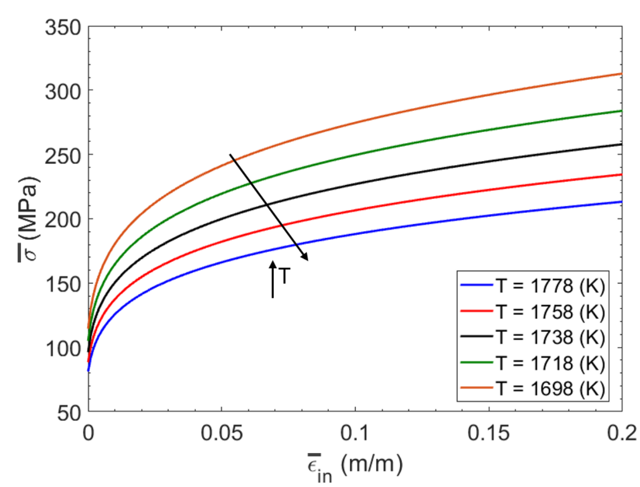

Figure 5.10 Stress-inelastic strain relation with temperature for low carbon content (0.045 pct) steel.

For the γ-austenite Kozlowski's III model is used [108]:

$$\dot{\epsilon}_{ie-\gamma} = f_{pctC}|F_\gamma|^{f_3-1}F_\gamma \exp(\frac{-4.465 \times 10^4}{T}) \tag{5.38}$$

where

$$F_\gamma = C\bar{\sigma} - f_1\bar{\epsilon_{ie}}|\bar{\epsilon_{ie}}|^{f_2-1} \tag{5.39}$$

$$f_1 = 130.5 - 5.128 \times 10^{-3}T \tag{5.40}$$

$$f_2 = -0.6289 + 1.114 \times 10^{-3}T \tag{5.41}$$

$$f_3 = 8.132 - 1.54 \times 10^{-3}T \tag{5.42}$$

$$f_{pctC} = 4.655 \times 10^4 + 7.14 \times 10^4(pctC) + 1.2 \times 10^5(pctC)^2 \tag{5.43}$$

Further details about the above equations are discussed elsewhere [114, 115]. In addition, for the regions with the mixture of δ-ferrite and γ-austenite, the rule of mixture cannot be applied. Instead, δ-ferrite mechanical properties are used anywhere the fraction of δ-ferrite is greater than 10 percent [108].

5.2.6 Solution Procedure

The governing equations of the one-way coupled thermo-mechanical analysis is solved through finite element method [116] using ABAQUS/Standard (implicit) [110]. First, the transient model resolves the temperature field in the whole domain and then with the obtained information of this step, the stress is solved in the second step which seems correct for the case of heat transfer, since the assumption in the model is the uniform heat transfer with ideal mold contact condition [108, 111]. The time of the analysis could be specified in the model. The transient heat conduction equation is solved using the implicit Euler method, and is followed by Newton's method to solve incrementally a time dependent stress field. Further details of the model is discussed elsewhere [108, 110, 114]. DC2D4 4-node linear diffusive heat transfer quadrilateral elements were used for the thermal analysis and CPEG4H 4-node hybrid bi-linear elements were used for a coupled temperature-displacement generalized plane strain analysis [108].

5.3 Model Verification and Validation

In order to verify and validate the model, the temperature and normal to solidification direction (hoop) stress distribution as well as shell thickness through distance below meniscus is compared with analytical solutions and shell growth measurements. The information on material properties for verification and validation cases are given in Table 5.1.

Table 5.1 Simulation conditions and material properties for the verification and validation cases

Condition/Material Properties	Weiner and Boley [117]	Case 1	Case 2	Case 3
Conductivity [$\frac{J}{sm^2K}$]	33	35	26	Varying
Density [$\frac{kg}{m^3}$]	7500	7860	7000	Varying
Young's Modulus [MPa]	4000 (solid) and 1400 (liquid)	-	Varying	Varying
Poisson's Ratio	0.3-0.5	-	0.3-0.5	0.3-0.5
Thermal Expansion [$\frac{1}{s}$]	2×10^{-5}	-	Varying	Varying
Pour Temperature [K]	1769	1735	1775.24	1806
Fixed Wall Temperature [K]	1273	1473	1473	1473
Liquidus Temperature [K]	1768.1	1685.8	1775.2	1801
Solidus Temperature [K]	1767.9	1684.8	1750	1778
Latent Heat [$\frac{kJ}{kg}$]	272	247	243	Varying
Specific Heat Capacity [$\frac{J}{kgK}$]	661	620	680	Varying
Carbon Content [wt pct]	-	-	0.3	0.045
Casting Speed [$\frac{m}{min}$]	-	-	1.35	2
Simulation time [s]	30	40	47.2	30

5.3.1 Weiner and Boley Verification Case

An analytical solution obtained from the work done by Weiner and Boley [117] is used to verify the model. The problem consists of a transient 2-D (Pseudo 1-D) thermo-mechanical analysis of a semi-infinite plate solidification for 30 seconds with a fixed-temperature boundary condition of an elastic-perfectly-plastic material which is initially in liquid phase. The plate is constrained against bending but otherwise free to shrink. The parameters used in this study are listed in Table 5.1.

A thin slice of 400 elements (40 mm×0.1 mm) through the thickness is used for the study along with thermal and stress BC's shown in Figure 5.11.

It is important to note that there are 3 isolated surfaces and only one surface with a constant temperature of cooling. As for the Mechanical BC's, by imposing generalized plane strain for the plane of the domain ($x-y$ plane and about z axis), bending is restricted through forcing all nodes in bottom surface of the slice to move together in $y-y$ direction. Additionally, Perpendicular to $x-y$ plane, all planer sections must remain planer (generalized plane strain about both x and y) [108].

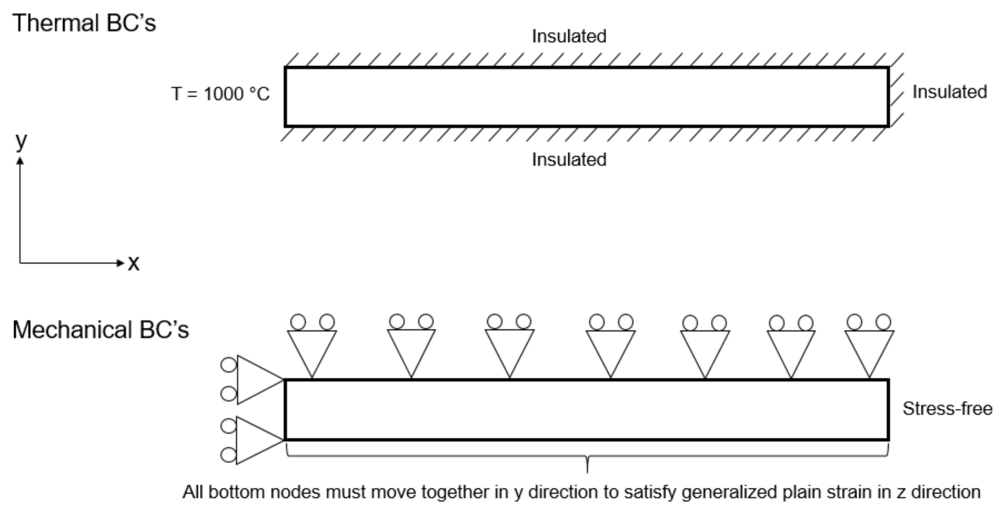

Figure 5.11 Verification domain with thermal and mechanical BC's [118].

The temperature and hoop stress results of the model for different temperature is plotted and compared with the analytical solution shown in Figure 5.12.

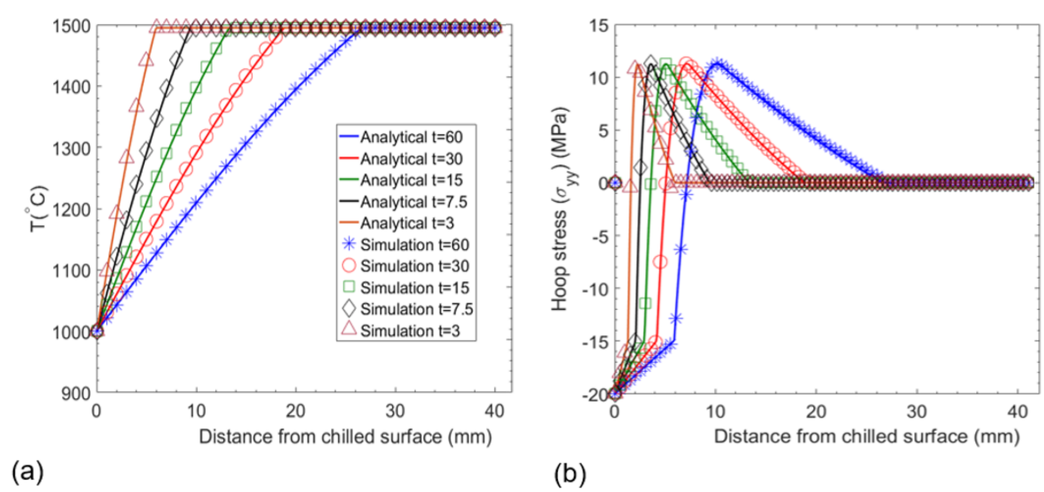

Figure 5.12 Verification of the model with analytical solution at different times of solidification for (a) Temperature (b) Hoop Stress.

For the temperature results, illustrated in Figure 5.12(a), at earlier times, solidified region is small and later due to solidification of domain, this region gets larger. There is a very good match between the exact solution and the simulation results. Similar to temperature results, the exact solution and the simulation results of the hoop stress are in complete agreement (shown in Figure 5.12(b)). The trend in stress with respect to distance is very similar to what was expected: a compression region, followed by a tension region, and finally leading to a decreasing trend in liquid region. The length of compression region increases as time goes by since the solidified regions gets larger [108].

5.3.2 Verification Case 1

This case is a transient 1-D thermal analysis of solidifying shell inside the mold for a 40-second dwell time. It is also, the verification of the model with the enhanced latent heat method and comparing it with a numerical analysis of a solidifying semi-infinite slab, an analytical solution, and the standard heat transfer analysis in ABAQUS. The mechanical BC's are exactly the same as Weiner and Boley verification case, and the only difference is in thermal BC's in which the quench temperature here is 1200 ^{o}C. The meshed domain along with the element used for the analysis is shown in Figure 5.13.

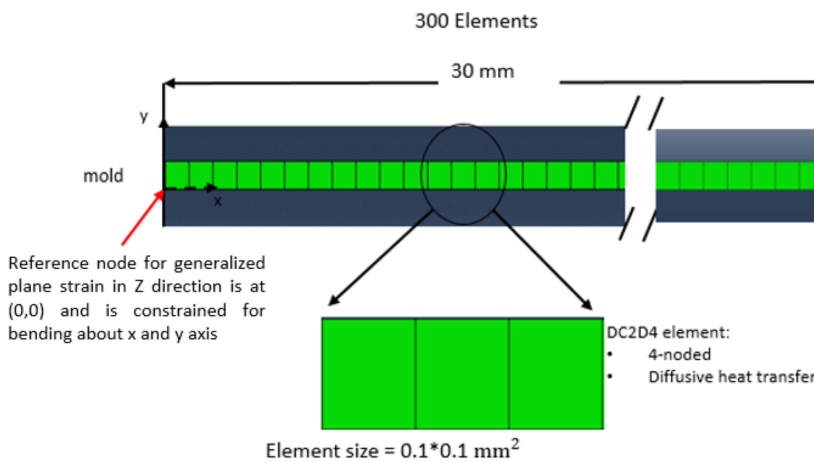

Figure 5.13 Verification case 1 meshed domain.

The superheat flux variation with time is obtained using Equation 5.28 for a low-velocity jet of the liquid flow, and the simulation conditions and material properties for this specific verification case are summarized in Table 5.1. It is shown in Figure 5.14 that the temperature distribution is plotted for 5 different cases: 1) Analytical temperature solution with superheat temperature (solid line), 2) Analytical solution with no superheat (dotted line), 3) Square symbols representing the standard ABAQUS solution ($T_{init} = 1462^{o}C$), 4) Diamond symbols representing ELH method using ABAQUS ($T_{init} = T_{liq} = 1412.79^{o}C$), and 5) Circle symbols representing the standard ABAQUS solution with no superheat ($T_{init} = T_{liq} = 1412.79^{o}C$).

It is clear that methods with superheat are almost identical in the solid, indicating ELH method accurately represents superheat effects in solid and mushy zones. Above the melting temperature, ELH method expectedly deviates, since $T_{init} = T_{liq}$, (adding superheat to latent heat only).

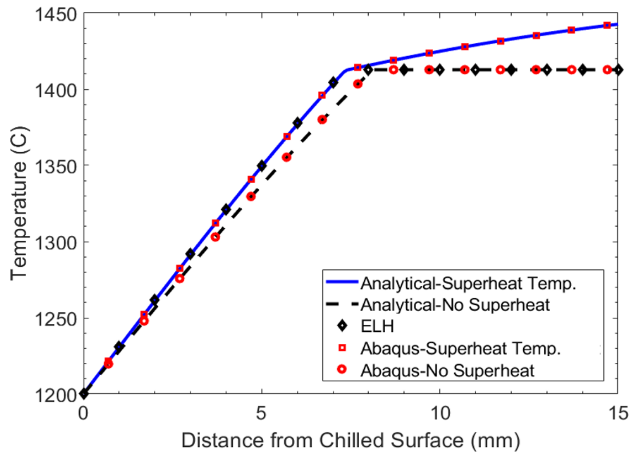

Figure 5.14 Temperature distribution comparison for verification case 1.

5.3.3 Verification Case 2

Verification case 2 is a transient 2-D (Pseudo 1-D) thermo-mechanical analysis of solidifying shell inside the mold (far from corners) for a 47.2-second dwell time with time-varying instantaneous heat flux and superheat flux (jet impingement case), as well as temperature-dependent, mechanical and thermal properties, phase fraction, and Young's modulus. The simulation domain along with the element type is shown in Figure 5.15.

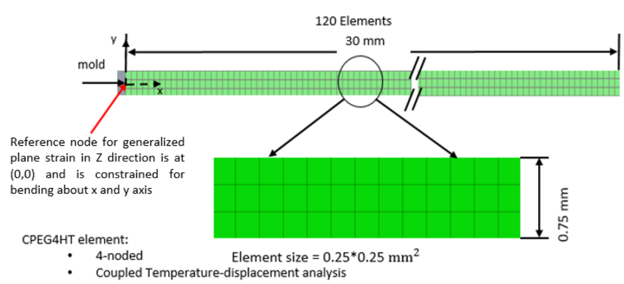

Figure 5.15 Verification case 2 meshed domain.

The mechanical BC's are exactly the same as Weiner and Boley verification case and the only difference is in thermal BC's in which the quench surface is substituted with varying mold heat flux. Also, it is important to note that the superheat flux is obtained from CFD simulation [109]. The prescribed mold heat flux along with the superheat flux [109] is shown in Figure 5.16.

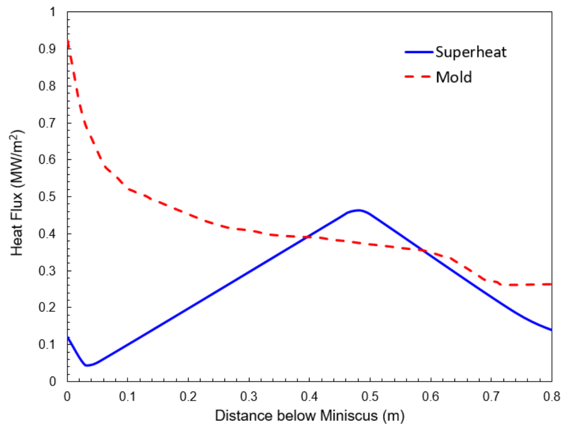

Figure 5.16 Verification case 2 prescribed mold heat flux and superheat flux variation with distance below meniscus.

Shell thickness comparison obtained from the model is compared with CON1D [119] results, experimental data [109], and the case using no superheat flux (but with superheat temperature) and shown in Figure 5.17.

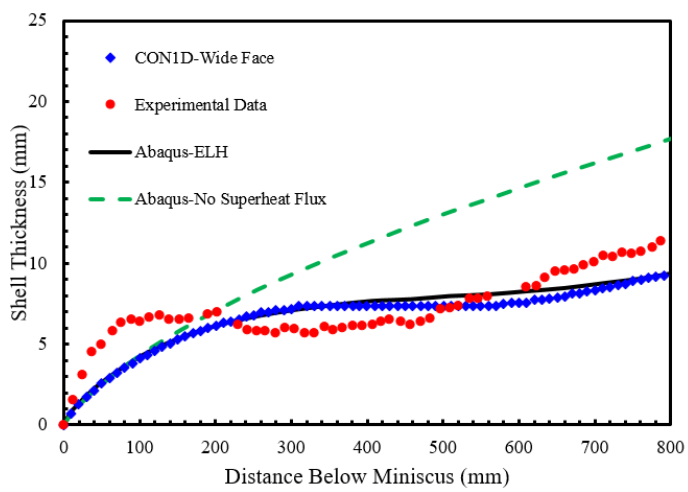

Figure 5.17 Shell thickness comparison for verification case 2.

It shows CON1D and ELH methods match and are able to capture localized shell thinning effect caused at the maximum value in superheat flux where jet hits the shell. Because breakout shell has a transient nature, there is a small displacement with the plant measurements. When ELH method is compared with the case with zero superheat, one can see a huge difference in shell thickness behavior. Having observed it, it seems very important to account for the effect of superheat while modeling the thermo-mechanical behavior of the process. Also to show the effect of superheat on the temperature and stress distribution, a comparison is shown in Figure 5.18 for the case with and without superheat.

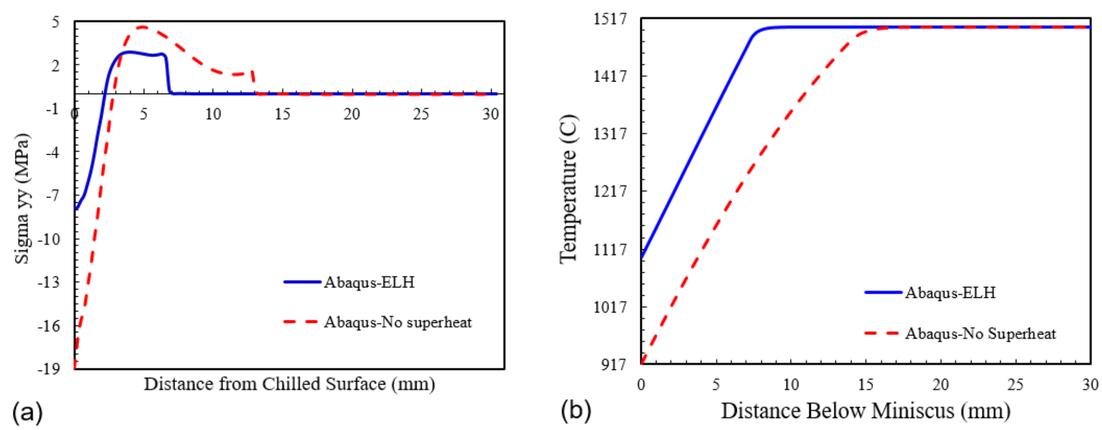

Figure 5.18 Temperature and hoop stress distribution comparison for verification case 2.

It is clear from the figure that at any specific time and location from chilled surface, due to superheat effect, ELH method temperature distribution expectedly is higher than no superheat case. Additionally, the stress distribution shows less compression near chilled surface, less tension at solidification front, and smaller solidifying length when superheat method is applied.

5.3.4 Validation Case 3

Validation case 3 is a transient 2-D (Pseudo 1-D) thermo-mechanical analysis of solidifying shell inside the mold of a low carbon steel grade (0.045 pct) for a 30-second dwell time (far from corners) with time-varying instantaneous heat flux and superheat flux (for a low-velocity jet case), along with the temperature-dependent, mechanical and thermal properties, phase fraction, specific heat, thermal conductivity, density, thermal linear expansion, and Young's modulus. The simulation domain with the element type is shown in Figure 5.19.

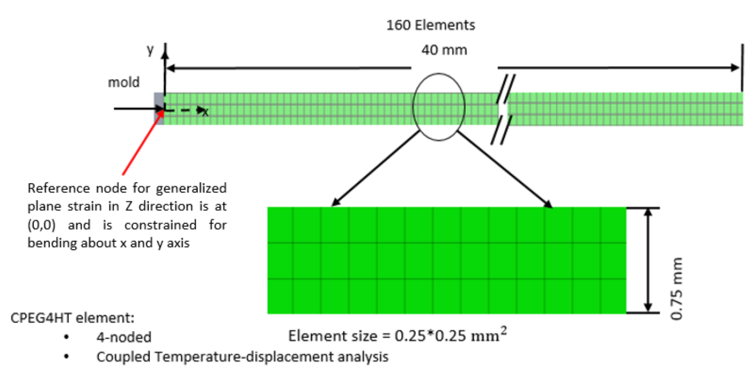

Figure 5.19 Validation case 3 meshed domain.

The mechanical BC's are exactly the same as Weiner and Boley verification case and the only difference is in thermal BC's in which the quench surface is substituted with varying mold heat flux [108]. Also, it is important to note that the superheat flux is obtained from Equation 5.28 for a low-velocity jet of the flow. The prescribed mold heat flux along with the superheat flux is shown in Figure 5.20.

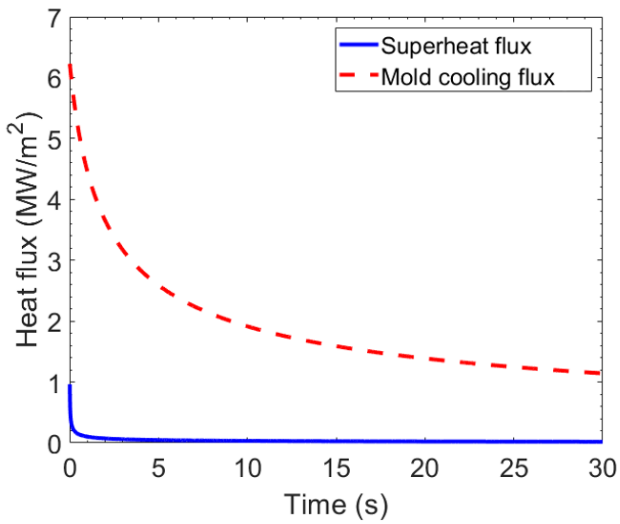

Figure 5.20 Validation case 3 prescribed heat flux [108] and superheat flux variation with distance below meniscus.

The temperature and stress distributions results at 3 different dwell times for ELH model and the standard ABAQUS with superheat temperature are plotted and compared in Figure 5.21 and Figure 5.22.

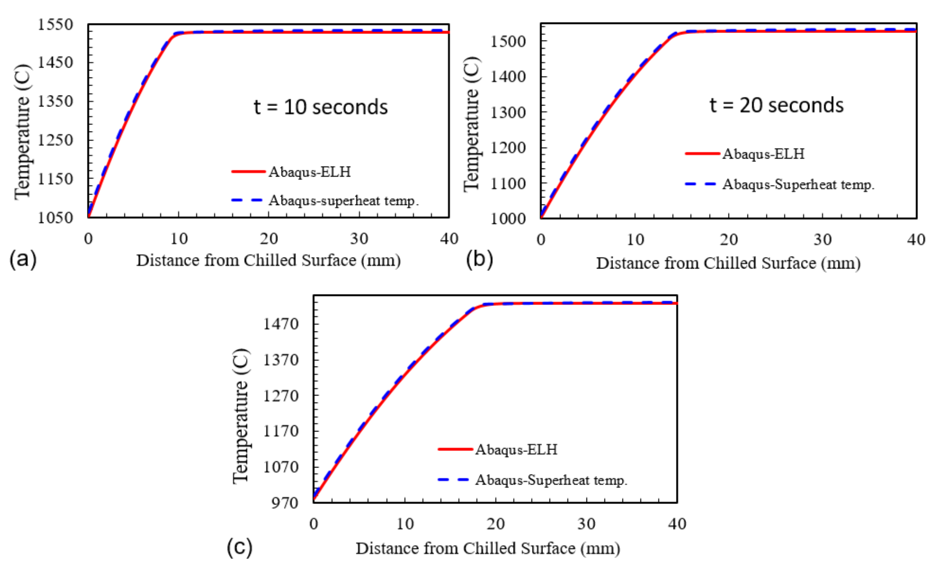

Figure 5.21 Validation case 3 temperature distribution comparison.

As shown in Figure 5.21 and Figure 5.22, ELH method and the standard ABAQUS with superheat temperature at different dwell times inside the mold match well with one another for temperature and stress distribution. For the temperature distribution, there is a slight mismatch (which was expected) mostly in liquid region, owing to the fact that for the original ABAQUS with superheat temperature the initial (pour) temperature is 5 K higher than the ELH method which only works with liquidus temperature.

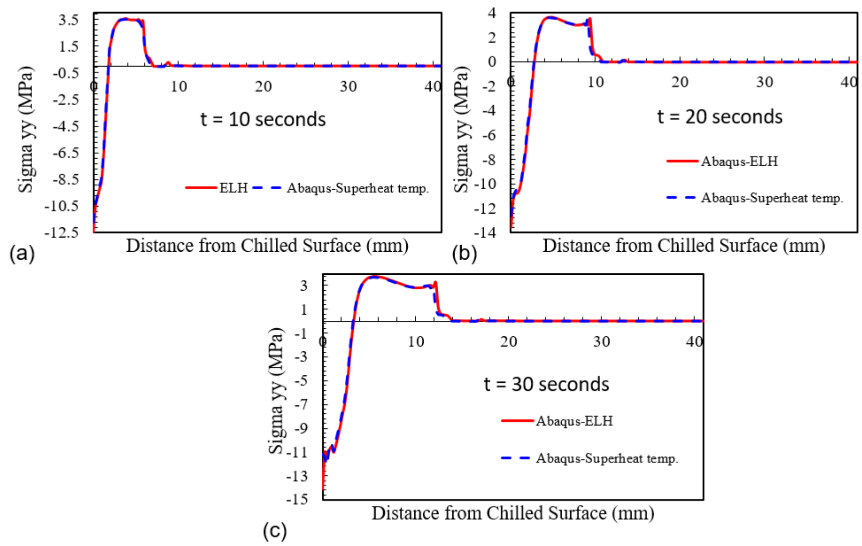

Figure 5.22 Validation case 3 hoop stress distribution comparison.

5.4 Case Study Investigating the Effect of Jet Impingement on Thermo-mechanical Behavior of the Shell

After the model is validated with the experimental data and verified with CON1D and FEA simulations, it is used to study the effect of a high-velocity jet (jet impingement) caused by the asymmetric clogging of the ports on the thermo-mechanical behavior of solidifying shell. To achieve that, a transient 2-D (Pseudo 1-D) thermo-mechanical analysis of solidifying shell inside the mold (far from corners) for an ultra low carbon steel grade (0.003 pct) is conducted for 35.7-second dwell time, with time-varying instantaneous heat flux and superheat flux (jet impingement case 2), as well as temperature-dependent, mechanical and thermal properties, phase fraction, and Young's modulus. The material properties for the case is summarized in Table 5.2.

Please note that since many mechanical and thermal properties of the domain vary with temperature, they are not addressed in Table 5.2. The simulation domain, the element type, and mechanical and thermal BC's are exactly the same as the validation case 3. Also, the superheat flux is obtained from CFD simulation for a high-velocity jet of the turbulent flow (shown in Figure 5.7).

Table 5.2 Conditions and material properties for the verification and validation cases

Condition/Material Properties	Case study
Poisson's Ratio	0.3-0.5
Pour Temperature $[K]$	1829
Fixed Wall Temperature $[K]$	1473
Liquidus Temperature $[K]$	1805
Solidus Temperature $[K]$	1794
Casting Speed $[\frac{m}{min}]$	1.51
Carbon Content [wt %]	0.003

Figure 5.23 shows the comparison of shell thickness prediction by CON1D [113], ELH method, and standard ABAQUS with no superheat for clogged and non-clogged ports. Shell thickness predictions of CON1D [113] with ELH method roughly match with maximum error of 1.1 mm. It seems that shell thinning effect is more evident in ELH method. Also, thickness of shell depends on 1) superheat flux and 2) interface (mold) heat flux. Furthermore, the shell on the clogged port side is thinner due to the less interface heat flux and in spite of less superheat flux and on the non-clogged side is thicker because of the shallower meniscus hooks and in spite of higher jet impingement. Finally, in cases of zero superheat, shell is thicker for both clogged and non-clogged ports comparing with CON1D and ELH.

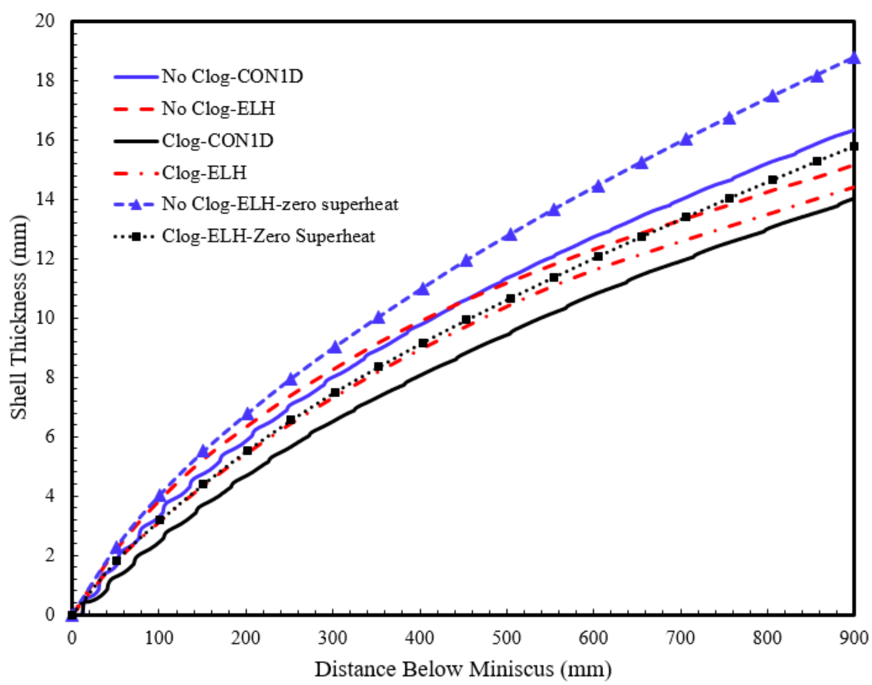

Figure 5.23 Comparison of shell thickness prediction of CON1D [113] with ELH method for the case study.

Next, temperature distribution at different times (before, during and after maximum jet impact) is shown in Figure 5.24.

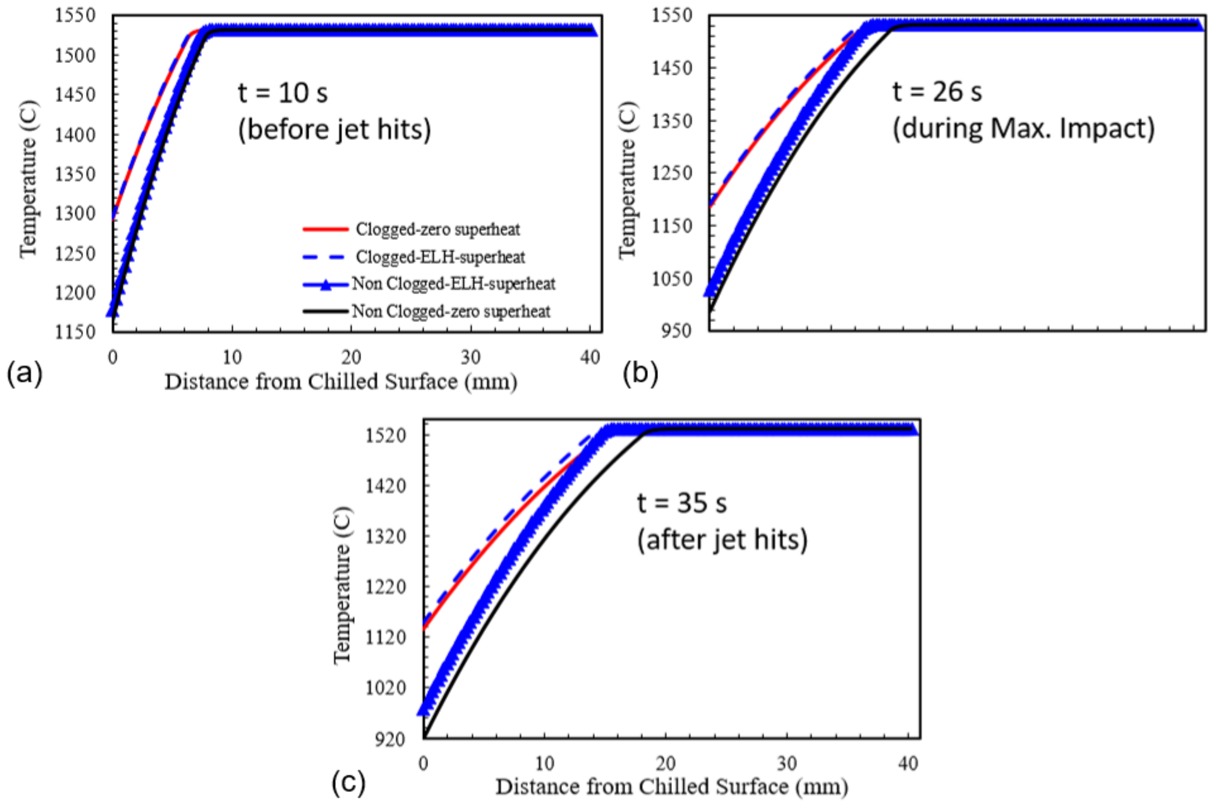

Figure 5.24 Temperature distributions at different times (before, during and after maximum jet impact).

It can be seen that before jet hits almost identical temperature distribution and solidifying front in both clogged and non-clogged sides are observed. During maximum impact, however, larger temperature differences and smaller solidifying front length is observed between in cases with superheat comparing to the one without superheat. Also, surface temperature is intermediate between before and after jet hits, so jet has little effect on surface temperature. Finally, after jet hits with no superheat, the shell is even thicker and the temperature is lower.

Furthermore, Hoop stress distribution at different times (before, during and after maximum jet impact) is shown in Figure 5.25. It can be seen that before (above where) jet hits almost identical stress distribution in both clogged and non-clogged sides is observed. Also, during maximum impact more surface compression is seen with non-clogged side and internal tension peak extends deeper for non-clogged side. Finally, after (below where) jet hits the trends simply continue, with more stress developed in the non-clogged side, owing to the colder shell.

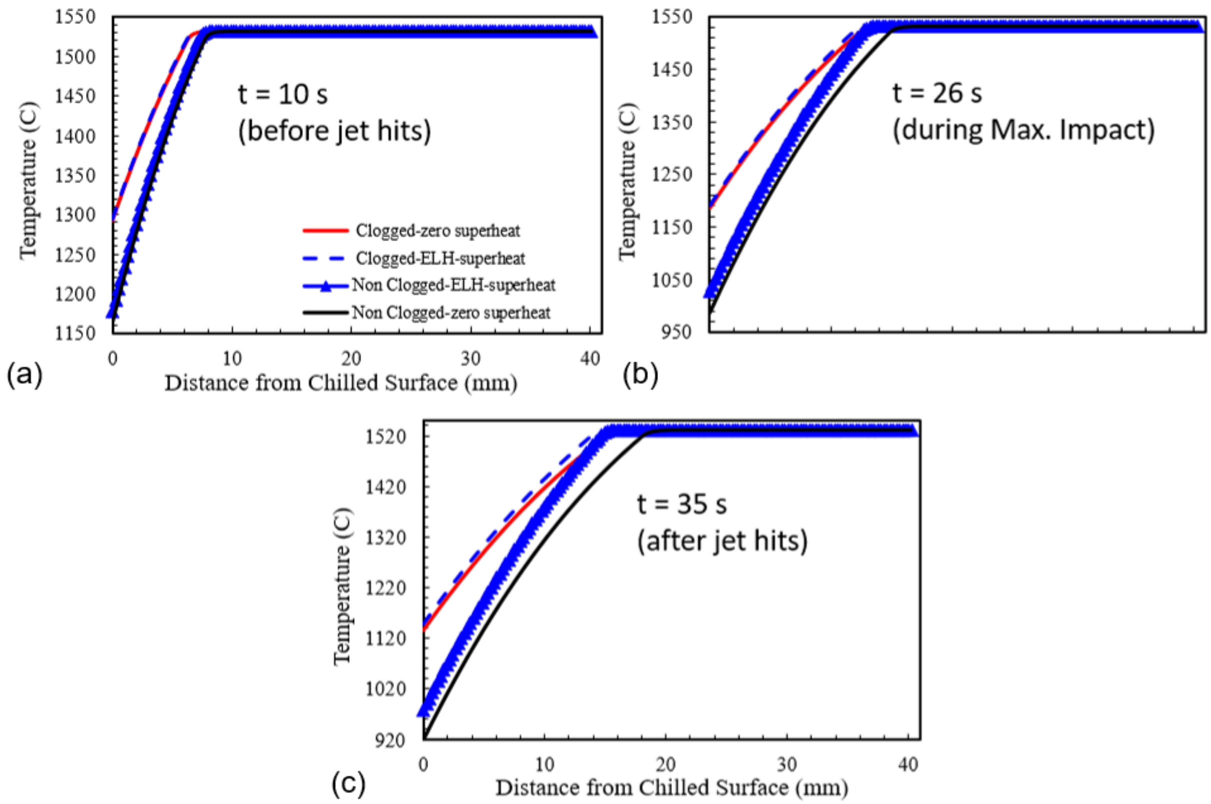

Figure 5.25 Hoop stress distributions at different times (before, during and after maximum jet impact).

Now, in order to fully understand the effect of interface heat flux and superheat flux on hoop stress contour as well as other surface strain components, it seems to be very appropriate to consider 4 possible cases and compare their results with one another. The four cases are shown in Table 5.3 below.

Table 5.3 Four possible cases to study the combined effect of mold and superheat flux

Case number	Description
1	Clogged port superheat with clogged port mold heat flux
2	Non-clogged port superheat with Non-clogged port mold heat flux
3	Clogged port superheat with Non-clogged port mold heat flux
4	Non-clogged port superheat with clogged port mold heat flux

the hoop stress contours of the solidifying shell for the mentioned four cases is plotted in Figure 5.26. Stress contour shows compression at surface, increasing to tension near the solidification front, and down to zero in the liquid. Also, subsurface tension region (associated with δ ferrite-γ austenite transformation) is larger in cases 2 and 3 comparing with cases 1 and 4, owing to their lower temperature (due to the higher interface heat flux). It is also evident that increasing mold heat flux increases shell thickness, however, mold heat flux increases shell thickness, which shows the effect of mold heat flux is larger than superheat flux.

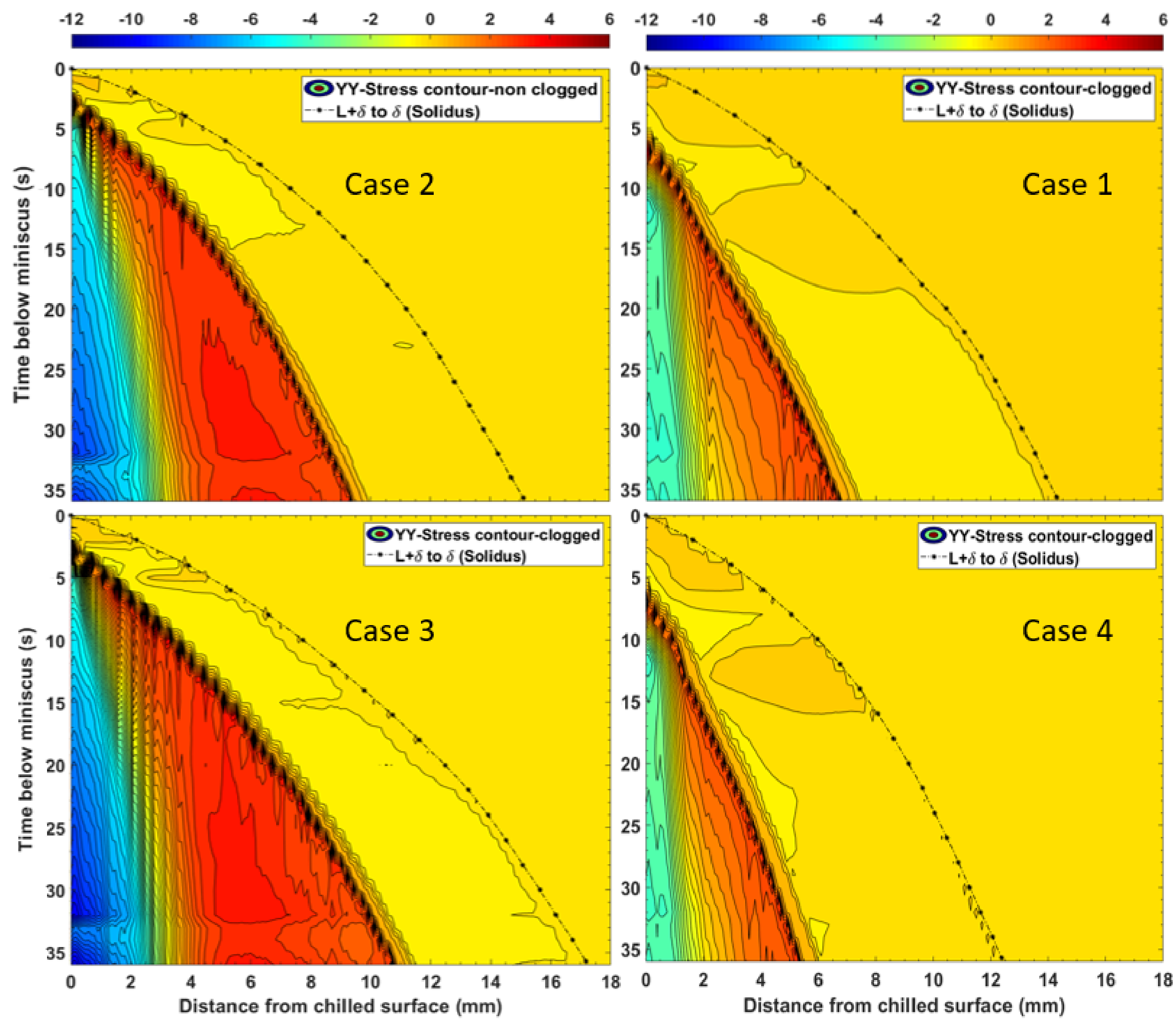

Figure 5.26 Hoop stress contours of the solidifying shell for different cases.

Next, the surface profile of hoop stress and inelastic strain through time below meniscus is plotted in Figure 5.27. It is concluded from the figure that the rapid surface cooling leads to shrinkage, and high initial inelastic strain in weak δ-ferrite phase [108]. This happens earlier in case 2 and 3 (higher interface heat flux) comparing with case 1 and 4 (lower interface heat flux), owing to their faster cooling. This causes tensile–stress peaks to arise at surface just below meniscus at $t = 2.85s$ for cases 2 and 3, and $t = 6.9s$ and $t = 7.2s$ for cases 1 and 4. Furthermore, due to the slower shell growth, the inelastic strain jumps and the tensile peaks are delayed in the shell for cases 1 and 4. Finally, peaks are higher and occur sooner for cases 2 and 3. Again, it is observed that changing superheat flux has little effect comparing with the mold heat flux.

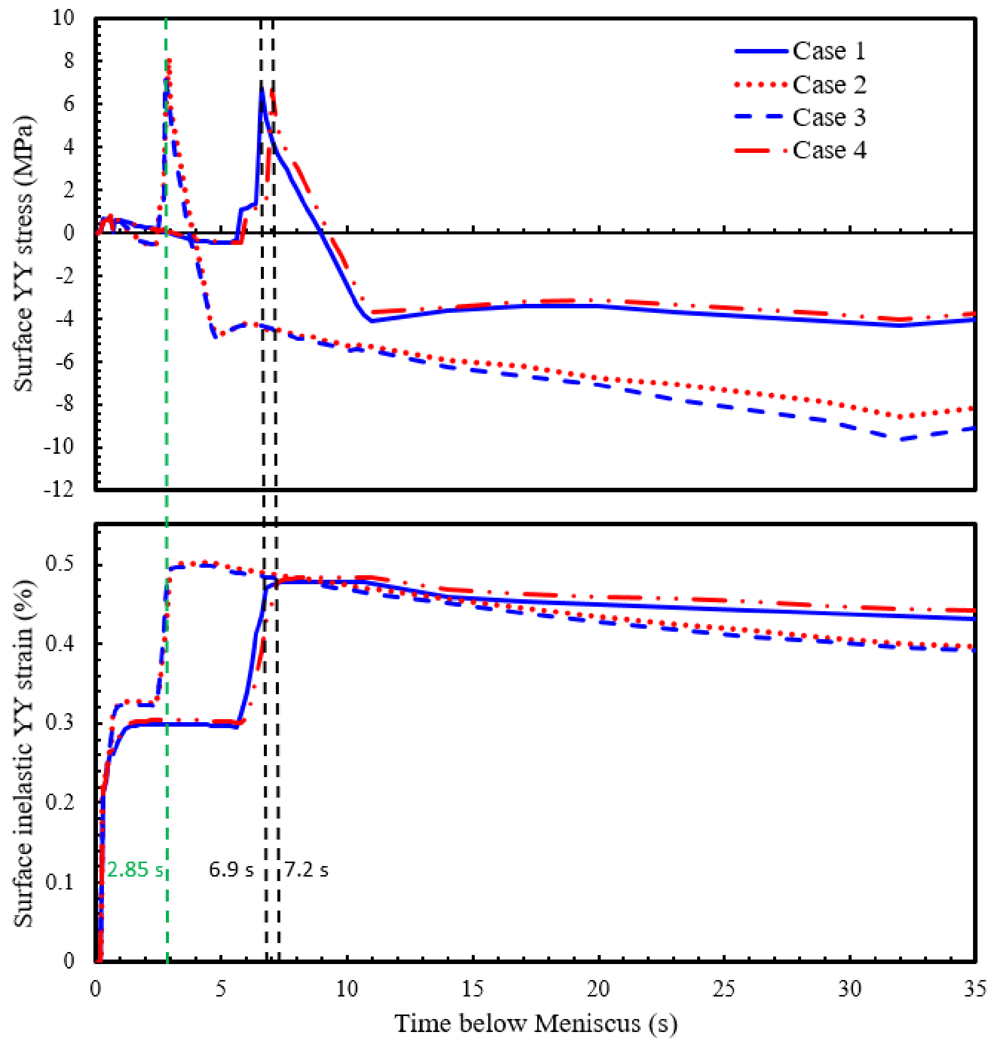

Figure 5.27 Surface profile of hoop stress and inelastic strain through time below meniscus.

Finally, Figure 5.28 shows the surface inelastic and thermal strain variation of four cases with respect to the time below meniscus. Similar to previous results, increasing the mold heat flux (i.e. cases 2 and 3) causes earlier surface elastic strain peaks and higher (in magnitude) surface thermal strain comparing to cases with lower mold heat flux. Changing superheat flux has little effect on both strains.

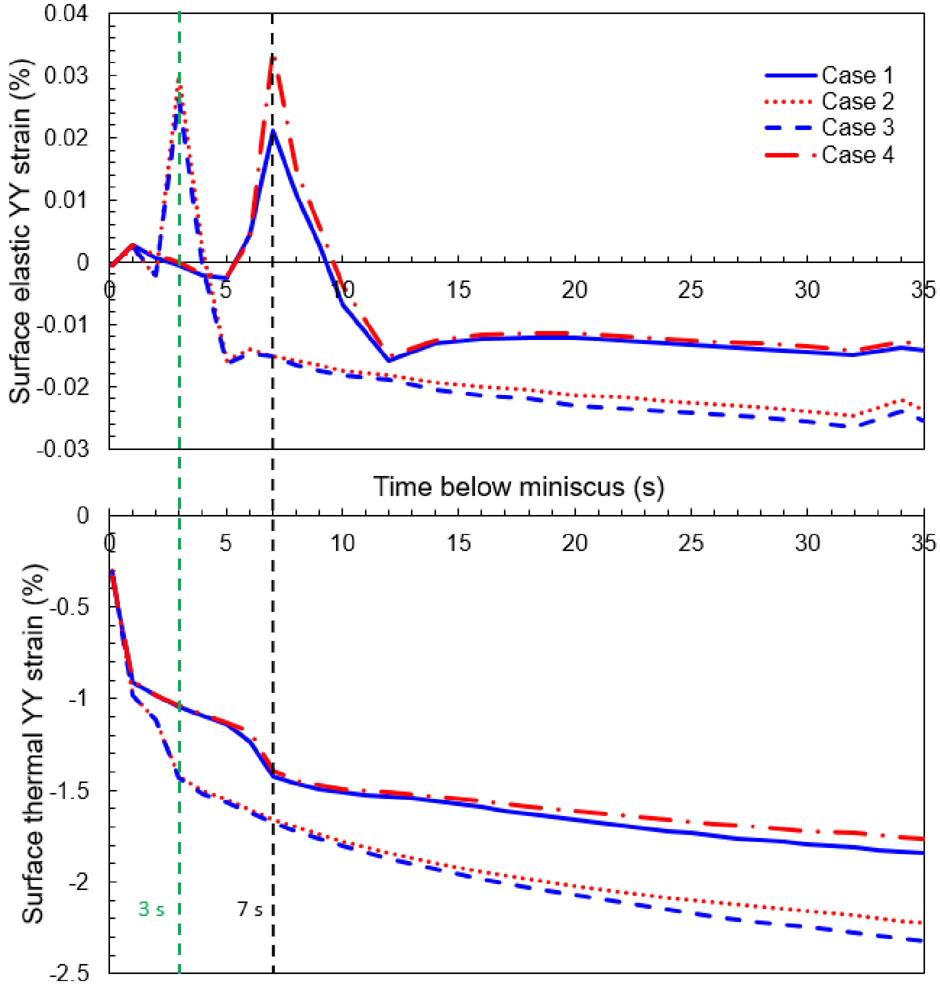

Figure 5.28 Surface profile of elastic and thermal strain through time below meniscus.

5.5 Conclusion

A new thermo-mechanical model equipped with Enhanced Latent Heat of fusion (ELH) method is introduced to include the effect of superheat on temperature, shell thickness, stress, and strain distribution in the solidifying shell. The material dependent thermal and mechanical properties added to the method to enhance the capability to investigate effect of fluid flow on solidification. It is observed that ELH results are able to match very well with existing model and plant measurements. Jet impingement of the high-velocity superheat flux on temperature, stress, and strain is less important than the effect of interface heat transfer. Net effect is a thinner shell for cases with lower mold heat flux, which causes higher temperature and smaller compression near chilled surface and smaller tension near solidifying front. Finally, for cases with higher superheat flux, colder shell causes faster-starting elastic and inelastic strain peaks, higher-magnitude stresses, and a surface tension peak.

CHAPTER 6
SUMMARY AND FUTURE WORK

The current thesis develops three computational multi-physics models that predict the effect of different casting conditions on pressure distribution, flow rate in the slide-gate and/or stopper-rod flow delivery systems, and thermo-mechanical behavior of solidifying shell while subjecting to low and/or high-velocity jet of molten steel in the mold, all in continuous casting of steel.

For the fluid flow section of the project, the current work implements Bernoulli's principle to develop two one-dimensional pressure energy models to predict pressure distribution and flow rate in slide-gate, PFSG, and stopper-rod, PFSR, controlled metal delivery systems. The models are standalone, user-friendly MATLAB-based graphical user interface programs capable of inverse solutions that enable users to conduct parametric studies in seconds. Although they are simple 1-D models, they include the effect of two-phase flow (argon gas-molten steel), mixture density, clogging at different places, and complex turbulent pressure loss terms. Both models were verified and validated against the CFD simulations and experimental data, respectively, with the maximum error of 6-8 pct. There were also, quite number of parametric studies on the effect of different casting conditions on pressure distribution (especially minimum pressure in the system) and flow rate in the system. Several interesting finds are observed: 1) increasing the pressure head height, governed by the distance between the liquid levels in the tundish and mold, increases the system flow rate, 2) increasing SEN length, and decreasing nozzle submergence depth, for a given slide-gate or stopper-rod opening can lead to a flow rate increase 3) increasing argon gas injection requires increasing the slide-gate or stopper-rod opening to maintain the flow rate.

More specifically for PFSG, it is concluded that increasing SEN diameter requires decreasing the slide-gate opening (and opening fraction) to maintain flow rate. Additionally, increasing argon injection causes increasing gate opening, which lowers the minimum pressure and aggravates the air aspiration problem. The minimum pressure tends to decrease (gets worse) with increasing tundish level height, and increasing nozzle bore diameter. Finally, it was concluded that to avoid near-vacuum minimum pressure in the system it is better to operate in either small slide-gate openings or near 100 pct openings.

For stopper-rod model, two new physical phenomena, cavitation and non-primed flow near the gap region, are also introduced to enhance the capability of the model to correctly predict the real physics occurring in the plant and is proven to match very well with the real plant experiments. This reveals new insights into the pressure / flow behavior in these casters.

As for the thermo-mechanical part of the thesis, a new model is introduced, developed, verified with CON1D and existing FEA simulations, and validated with experimental data. The model can successfully predict the effect of superheat flux, which is a heat flux delivered to the solidification front from the molten steel, on thermo-mechanical behavior of solidifying shell inside the continuous casting of steel mold. The model is able to predict shell thickness, temperature, hoop stress, and strain (including elastic, inelastic, thermal, and fluid components) distribution for a thin domain with temperature and composition varying thermo-mechanical properties. The model can also efficiently operate for both low and high-velocity jet of the molten steel flow. It is shown that the effect of hot mold heat flux is larger than a turbulent (high-velocity jet) superheat flux. Hence, mold heat flux dictates the shell thickness, temperature, surface hoop stress, and surface strain components distribution.

As for further applications of this work, the following is suggested:

- As shown for the PFSR (Chapter 4), there are still some degrees of freedom that prevent from yielding to one single solution when considering both cavitation and non-primed flow methodology. There needs to be more work on this to possibly include new physics/equations. Additionally, it seems there should be more parametric studies to understand the effect of asymmetric clogging and argon gas injection on flow rate and pressure distributions by improving both PFSG and PFSR.

- Clogging index needs to be developed properly in both PFSG and PFSR. There needs to be a formulation using which the clogging is estimated and output, based on the difference between the predicted flow-rate / opening relationship (with the clogging) relative to the non-clogged case (which should match plant measurements at beginning of the casting when there is no clogging).

- The different gas flow rates together in the min gap region must be also added to determine the actual cavitation pressure (i.e. sum of the partial pressure of CO, N, H).

- Argon gas injection capability must be incorporated into PFSR to be added with cavitation gas flow rate in the min pressure region.

- Also, it is important to consider different mold heat flux and/or superheat flux distributions and their effect on thermo-mechanical behavior of the solidifying shell inside the mold.

- Finally, to develop a comprehensive fluid flow-thermal stress model, it is crucial to run PFSR and/or PFSG with clogging inclusion along with CFD simulations and the stress model to investigate other flow-related issues on the thermal-stress behavior of the solidifying shell inside the mold.

REFERENCES

[1] World steel in figures 2015, World Steel Association, 2015.

[2] Brian G. Thomas. Introduction to continuous casting, 2022. URL http://ccc.illinois.edu/introduction/concast.html.

[3] H. Bai and B. G. Thomas. Effects of clogging, argon injection, and continuous casting conditions on flow and air aspiration in submerged entry nozzles. *Metallurgical and Materials Transactions B*, 32(4), 08 2001.

[4] H. Yang, H. Olia, and B. G. Thomas. Modeling air aspiration in steel continuous casting slide-gate nozzles. *Metals*, 11, 01 2021.

[5] L. Zhang, Y. Wang, and X. Zuo. Flow transport and inclusion motion in steel continuous-casting mold under submerged entry nozzle clogging condition. *Metallurgical and Materials Transactions B*, 39(4), 01 2008.

[6] K. G. Rackers and B. G. Thomas. Clogging in continuous casting nozzles. *Proc. of 78th Steelmaking Conf., The Iron and Steel Society, Warrendale, PA*, 78, 04 1995.

[7] S. M. Cho, S. H. Kim, R. Chaudhary, B. G. Thomas, H. J. Shin, W. R. Choi, and S. K. Kim. Effect of nozzle clogging on surface flow and vortex formation in the continuous casting mold. *AISTech - Iron and Steel Technology Conference Proceedings, Indianapolis, IN, AIST, Warrendale, PA*, 2, 05 2011.

[8] S. M. Cho and B. G. Thomas. Effects of clogging on fluid flow, solidification, and defects in slab casting, 2021.

[9] S. Yokoya, S. Takagi, H. Souma, M. Iguchi, Y. Asako, and S. Hara. a steel jet deep into the mold and trapped in the steel product. *ISIJ International*, 38, 1998.

[10] Y. Murakami, S. Kodama, and S. Konuma. Quantitative evaluation of effects of non-metallic inclusions on fatigue strength of high strength steels. i: Basic fatigue mechanism and evaluation of correlation between the fatigue fracture stress and the size and location of non-metallic inclusions. *International Journal of Fatigue*, 11, 09 1989.

[11] A. D. Wilson. The influence of inclusions on the toughness and fatigue properties of a516-70 steel. *Journal of Engineering Materials Technology*, 101(3), 07 1979.

[12] L. Zhang, J. Aoki, and B. G. Thomas. Inclusion removal by bubble flotation in a continuous casting mold. *Metallurgical and Materials Transactions B*, 37(3), 06 2006.

[13] S.R. Cameron. The reduction of tundish nozzle clogging during continuous casting at dofasco. *Steelmaking Conference Proceedings, Toronto, Canada*, 75, 1992.

[14] N.V. Sidmar, F. Haers, R. Bauwens, and R. de Croock. First experience in using the caster tube change device (tcd90). *Fourth International Conference on Continuous Casting*, 1988.

[15] A. Jaffuel and J. P. Robyns. Flo con slide nozzles. *Continuous Casting of Steel, Biarritz, France*, 1976.

[16] E. S. Szekeres. Review of strand casting factors affecting steel product cleanliness. *Fourth International Conference on Clean Steel, Balatonszéplak, Hungary*, 1992.

[17] United States Steel. The making,shaping, and treating of steel. *The Physical Chemistry of Iron and Steelmaking*, 1985.

[18] B. Bergmann, N. Bannenberg, and R. Piepenbrock. Castability assurance of aluminum-killed silicon-free steel by calcium cored wire treatment. *European Conference on Continuous Casting*, 1991.

[19] H.H. Bauer. Effect of deoxidation on the castability of steel. *International Conference on Continuous Casting, Biarritz, France*, 1976.

[20] J.R. Bourguignon, J.M. Dixmier, and J.M. Henry. Different types of calcium treatment as contribution to development of continuous casting process. *Steel Times, Biarritz, France*, 1986.

[21] D. Bolger. Stopper rod and submerged nozzle design and operation in continuous casting. *77th Steelmaking Conference, Chicago, IL*, 1994.

[22] Z. Chen, H. Olia, B. Petrus, M. Rembold, J. Bentsman, and B. G. Thomas. Dynamic modeling of unsteady bulging in continuous casting of steel. *The Minerals, Metals Materials Society (TMS)*, 02 2019.

[23] POSCO, Korean patent application 10-2012-0026720, 2012.

[24] J. Savolainen, A. Rousu, T. Fabritius, O. Mattila, and P. Sulasalmi. Modelling of pressure distribution inside the sen in a stopper-rod controlled system. *Steel Research International*, 81, 11 2010.

[25] R. Liu and B. G Thomas. Measurements of molten steel surface velocity and effect of stopper-rod movement on transient multiphase fluid flow in continuous casting. *ISIJ International*, 54, 2014.

[26] M. Javurek and M. Thumfart. Low pressure effects in sen-stopper region in continuous casting. *Steel Research International*, 86, 2015.

[27] H. Yang, S. P. Vanka, and B. G. Thomas. Modeling argon gas behavior in continuous casting of steel. *The Journal of The Minerals, Metals Materials Society (TMS)*, 70, 07 2018.

[28] R. Liu and B. G. Thomas. Model of gas flow through porous refractory applied to an upper tundish nozzle. *Metallurgical and Materials Transactions B*, 46(1), 02 2015.

[29] L. Zhang, S. Yang, K. Cai, J. Li, X. Wan, and B. G. Thomas. Investigation of fluid flow and steel cleanliness in the continuous casting strand. *Metallurgical and Materials Transactions B*, 38B, 02 2007.

[30] Y. Wang and L. Zhang. Fluid flow-related transport phenomena in steel slab continuous casting strands under electromagnetic brake. *Metallurgical and Materials Transactions B*, 42B, 12 2011.

[31] W. Chen, Y. Ren, and L. Zhang. Large eddy simulation on the two-phase flow in a water model of continuous casting strand with gas injection. *Steel Research International*, 90(4), 08 2019.

[32] B. G. Thomas. Review on modeling and simulation of continuous casting. *Steel Research International*, 2017.

[33] H. Yang, S. P. Vanka, and B. G. Thomas. Mathematical modeling of multiphase flow in steel continuous casting. *ISIJ International*, 59, 2019.

[34] S. M. Cho, M. Liang, H. Olia, L. Das, and B. G. Thomas. Multiphase flow-related defects in continuous casting of steel slabs. *TMS Annual Meeting, Pittsburgh, PA, Warrendale, PA*, 2020.

[35] H. Olia, H. Yang, S. M. Cho, M. Zappulla, and B. G. Thomas. Pressure-drop and flow rate model of slide gate metal delivery systems: PFSG. *AISTech - Iron and Steel Technology Conference Proceedings, Warrendale, PA*, 2020.

[36] R. Liu, B. Forman, H. Yin, and Y. Lee. Understanding fluid flow in the stopper rod control system. *AISTech - Iron and Steel Technology Conference Proceedings, Philadelphia, PA*, 2018.

[37] H. Yang, S. Vanka, and B. G. Thomas. A hybrid eulerian–eulerian discrete-phase model of turbulent bubbly flow. *Journal of Fluid Engineering*, 140, 05 2018.

[38] R. Liu and B. G. Thomas. Model of gas flow through porous refractory applied to an upper tundish nozzle. *Metallurgical and Materials Transactions B*, 4, 02 2014.

[39] fsolve. URL https://www.mathworks.com/help/optim/ug/fsolve.html?s_tid=doc_ta.

[40] Eric W Weisstein. Circle-circle intersection, . URL http://mathworld.wolfram.com/Circle-CircleIntersection.html.

[41] F. M. White. *Fluid Mechanics*. Mc Graw Hill, 1221 Avenue of the Americas, New York, NY 10020, USA, 2007.

[42] *Flow of fluids through valves fittings and pipes*. Crane Co., 300 Park Avenue, New York, NY, 10022, USA, 1999.

[43] H. Oertel. *Prandtl-Essentials of Fluid Mechanics*. Springer-Verlag, 175 Fifth Avenue, New York, NY 10010, USA, 2004.

[44] G. J. O. Jameson. The perimeter of an ellipse. *The Mathematical Gazette*, 98, 03 2014.

[45] B. G. Thomas, X. Huang, and R.C. Sussman. Simulation of argon gas flow effects in a continuous slab caster. *Metallurgical and Materials Transactions B*, 25B, 08 1994.

[46] B. E. Launder and D. B. Spalding. *Lectures in mathematical models of turbulence*. Academic Press London, 1972.

[47] D.K. Lilly. A proposed modification of the german0 subgrid-scale closure method. *Physics of Fluids A: Fluid Dynamics*, 4, 03 1992.

[48] *ANSYS FLUENT 18.1-Theory Guide*. ANSYS. Inc., 2017.

[49] S.-M. Cho, S.-H. Kim, and B.G. Thomas. Transient fluid flow during steady continuous casting of steel slabs: Part i. measurements and modeling of two-phase flow. *ISIJ International*, 54, 2014.

[50] F. Durst, R. Friedrich, B. E. Launder, F. W. Schmidt, U. Schumann, and J. H. Whitelaw. *Turbulent Shear Flows 8*. Springer-Verlag, 1991.

[51] L. Das and B. G. Thomas. *CCC Annual Meeting, Continuous Casting Center, Colorado School of Mines, Golden, CO, USA*, 2018.

[52] S.-M. Cho and B. G. Thomas. Effects of m-ems on turbulent thermal fluid flow and initial solidification in large-section bloom casting. *CCC Annual Meeting, Continuous Casting Center, Colorado School of Mines, Golden, CO, USA*, 2019.

[53] M. Javurek and M. Thumfart. Multiphase flow and low pressure effects in the sen. *8th ECCC Conference Proceedings*, 2015.

[54] U. Sjostrom, M. BUl'ty, A. Gaggioli, and J.P. Rador. An experimental study of argon injection and aspiration of air into stopper rods in continuous casters. *Steelmaking Conference Proceedings*, pages 63–71, 1998.

[55] S. Dawson. Tundish nozzle blockage during the continuous casting of aluminum-killed steel. *Steelmaking Conference Proceedings*, 73, 1990.

[56] I.V. Samarasekera, D.L. Anderson, and J.K Brimacombe. The thermal distortion of continuous casting billet molds. *Metallurgical and Materials Transactions B*, 13B:91–104, 1982.

[57] S. Mahmood. *Modeling Of Flow Asymmetries And Particle Entrapment In Nozzle And Mold During Continuous Casting Of Steel Slabs*. PhD thesis, University of Illinois at Urbana-Champaign, 2006.

[58] M.L. Zappulla. *Mechanisms Of Longitudenal Depression Formation In Steel Continuous Casting*. PhD thesis, Colorado School of Mines, 2020.

[59] H. Olia, H. Yang, S.-M. Cho, M. Liang, L. Das, and B.G. Thomas. Pressure distribution and flow rate behavior in continuous-casting slide-gate systems: PFSG. *Metallurgical and Materials Transactions B*, 53B:1661–80, 2022.

[60] K. G. Rackers. Mechanism and mitigation of clogging in continuous casting nozzles. Master's thesis, University of Missouri, 1989.

[61] S. Ogibayashi. Mechanism and countermeasure of alumina buildup on submerged nozzle in continuous casting (in japanese), Apr 1994.

[62] E. Marino. Use of calcium oxide as refractory material in steel making processes. *Refractories for the Steel Industry, Elsevier Applied Science*, 1994.

[63] P.M. Benson, Q.K. Robinson, and H.K. Park. Evaluation of lime-containing sub-entry shroud liners to prevent alumina clogging. *76 th Steelmaking Conference, Dallas, Texas*, 73, 1993.

[64] E. Luhrsen, A. Ott, W. Parbel, J. Piret, and R. Ruddlestone. Boron nitride enrichment of the submerged entry nozzles: A solution to avoid clogging. *1st European Conference on Continuous Casting*, 1991.

[65] N.A. McPherson and A. McLean. Continuous casting: Tundish to mold transfer operations. *Iron and Steel Society*, 6, 1992.

[66] E. Hoffken, H. Lax, and G. Pietzko. Development of improved immersion nozzles for continuos slab casting. *4th. International Conference Continuous Casting*, 1988.

[67] R. Liu, J. Sengupta, D. Crosbie, M.M. Yavuz, and B.G. Thomas. Effects of stopper rod movement on mold fluid flow at arcelormittal dofasco's no. 1 continuous caster. *AISTech - Iron and Steel Technology Conference Proceedings, Indianapolis, IN*, 2011.

[68] S.-M. Cho and B.G. Thomas. Effect of bubble behavior for a stopper rod with multiple side-channel injection on bubble size distributions in nozzle and mold during continuous casting of steel. *AISTech - Iron and Steel Technology Conference Proceedings, Pittsburgh, PA.*, 2019.

[69] K. A. Gürsoy. Quantifying the effect of flow rate controllers on liquid steel flow in continuous casting mold using cfd modeling. Master's thesis, Middle East Technical University, Turkey, 2014.

[70] R. Liu, B.G. Thomas, J. Sengupta, S. D. Chung, and M. Trinh. Measurements of molten steel surface velocity and effect of stopper-rod movement on transient multiphase fluid flow in continuous casting. *ISIJ International*, 54:2314–23, 2014.

[71] R. Chudhary, G.-G. Lee, B.G. Thomas, S.-M. Cho, S.-H Kim, and O.-D. Kwon. Effect of stopper-rod misalignment on fluid flow in continuous casting of steel. *Metallurgical and Materials Transactions B*, 42 (B):300–15, 2011.

[72] P. Ni, L. T. I. Jonsson, M. Ersson, and P. G. Jönsson. Application of a swirling flow producer in a conventional tundish during continuous casting of steel. *ISIJ International*, 57:2175–2184, 2017.

[73] R. Chudhary, G.-G. Lee, B.G. Thomas, and S.-H Kim. Transient mold fluid flow with well- and mountain-bottom nozzles in continuous casting of steel. *Metallurgical and Materials Transactions B*, 39 (B):870–884, 2008.

[74] J. Eck. Development of systematic measurement on liquid metal. Master's thesis, Luleå University of Technology, Sweden, 2019.

[75] R. Wang, H. Li, F. Guerra, C. Cathcart, and K. Chattopadhyay. Development of quantitative indices and machine learning-based predictive models for sen clogging. *AISTech - Iron and Steel Technology Conference Proceedings, Nashville, TN.*, 2021.

[76] Eric W Weisstein. Conical frustum, . URL https://mathworld.wolfram.com/ConicalFrustum.html.

[77] B. Massey and J. Ward-Smith. *Mechanics of Fluids*. Taylor Francis, New York, NY, USA, 2006.

[78] L. Zhang, S. Yang, K. Cai, J. Li, X. Wan, and B. G. Thomas. Investigation of fluid flow and steel cleanliness in the continuous casting strand. *Metallurgical and Materials Transactions B*, 38(B), 02 2007.

[79] M. Burty, C. Pussé, M. Alvarez, P. Gaujé, and G. Grehan. Fundamental study of gas-liquid flows in cc machine. *84th Steelmaking Conference, Warrendale, PA*, 84:89–98, 2001.

[80] C. E. Brennen. *Cavitation and bubble dynamics*. Cambridge University Press, 32 Avenue of Americas, New York, NY 10013-2473, USA, 2014.

[81] C. K. Gupta. *Chemical Metallurgy: Principles and Practice*. WILEY-VCH Verlag GmbH Co. KGaA, Weinheim, 2003.

[82] K. J. Laidler. *Chemical kinetics*. Harper Row, 1987.

[83] M. J. Moran and H. N. Shapiro. *Fundamentals of Engineering Thermodynamics*. John Wiley Sons, Inc, The Atrium, Southern Gate, Chichester, West Sussex PO19 8SQ, England, 2006.

[84] B. Deo and R. Boom. *Fundamentals of steelmaking metallurgy*. Prentice Hall, 1993.

[85] E. T. Turkdogan. *Fundamentals of steelmaking*. Institute of Materials, 1996.

[86] F. Oeters. *Metallurgy of steelmaking.* Dusseldorf: Verlag Stahleisen, 1994.

[87] J. Szekely, G. Carlsson, and L. Helle. *Ladle metallurgy.* Springer-Verlagn, 1989.

[88] B. Mintz. The influence of composition on the hot ducility of steels and to the problem of transverse cracking. *ISIJ International*, 39, 06 1999.

[89] J. Szekely and V. Stanek. On heat transfer and liquid mixing in the continuous casting of steel. *Metallurgical Transactions*, 1:119–126, 1970.

[90] J. Szekely and R. T. Yadoya. The physical and mathematical modelling of the flow field in the mold region in continuous casting systems: Part ii. the mathematical representation of the turbulent flow field. *Metallurgical Transactions*, 4:1379–1388, 05 1973.

[91] J.E. Lait, J.K. Brimacombe, and F. Weinberg. Pool profile, liquid mixing and cast structure in steel, continuously cast in curved moulds. *Ironmaking and Seelmaking*, 1:35–42, 1974.

[92] JK. Brimacombe. Design of continuous casting machines based on a heat-flow analysis: state-of-the-art review. *Canadian Metallurgical Quarterly*, 15(2):163–175, 1976.

[93] D. Mazumdar. A consideration about the concept of effective thermal conductivity in continuous casting. *ISIJ international*, 29(6):524–528, 1989.

[94] S. K. Choudhary, D. Mazumdar, and A. Ghosh. Mathematical modelling of heat transfer phenomena in continuous casting of steel. *ISIJ international*, 33:764–774, 1993.

[95] J.-E. Lee, T.-J. Yeo, K. H. Oh, J.-K. Yoon, and U.-S. Yoon. Prediction of cracks in continuously cast steel beam blank through fully coupled analysis of fluid flow, heat transfer, and deformation behavior of a solidifying shell. *Metallurgical and Materials Transactions A*, 31A:225–237, 2000.

[96] A. Teskeredžić, I. Demirdžić, and S. Muzaferija. Numerical method for heat transfer, fluid flow, and stress analysis in phase-change problems. *Numerical Heat Transfer, Part B: Fundamentals*, 42, 2002.

[97] A. Chatterjee, V. Prasad, and D. Sun. A full 3-dimensional adaptive finite volume scheme for transport and phase-change processes, part ii: Application to crystal growth. *Numerical Heat Transfer, Part B: Fundamentals*, 37, 2000.

[98] C. Del Borrello and E. Lacoste. Numerical simulation of the liquid flow into a porous medium with phase change: Application to metal matrix composites processing. *Numerical Heat Transfer, Part B: Fundamentals*, 44, 2003.

[99] Y.-P. Du, R. Shi, J.-W. Yang and X.-C. Cui. Fluid flow and solidification simulation in beam blank continuous casting process with 3d coupled model. *JOURNAL OF IRON AND STEEL RESEARCH, INTERNATIONAL*, 13(4):17–21, 2006.

[100] M. R. R. I. Shamsi and S. K. Ajmani. Three dimensional turbulent fluid flow and heat transfer mathematical model for the analysis of a continuous slab caster. *ISIJ International*, 47:433–442, 2007.

[101] K. Ho and D. Pehlke. Metal-mold interfacial heat transfer. *Metallurgical and Materials Transactions B*, 16(B):585–594, 1985.

[102] J.E. Kelly, K.P. Michalek, T.G. O'Connor, B.G. Thomas, and J.A. Dantzig. Initial development of thermal and stress fields in continuously cast steel billets. *Metallurgical and Materials Transactions A*, 19(A):2589–2602, 1988.

[103] B.G. Thomas and M. Bellet. Modeling of stress, distortion and hot tearing. *ASM Handbook*, 15: 449–461, 2008.

[104] S. Koric and B.G. Thomas. Efficient thermo-mechanical model for solidification processes. *International journal for numerical methods in engineering*, 66(12):1955–1989, 2006.

[105] S. Koric, L. C. Hibbeler, and B.G. Thomas. Explicit coupled thermo-mechanical finite element model of steel solidification. *International journal for numerical methods in engineering*, 78:1–31, 2009.

[106] S. Koric, L. C. Hibbeler, R. Liu, and B.G. Thomas. Multiphysics model of metal solidification on the continuum level. *Numerical Heat Transfer, Part B: Fundamentals*, 58:371–392, 2010.

[107] M. L. S. Zappulla, S.-M. Cho, S. Koric, H.-J. Lee, S.-H. Kim, and B.G. Thomas. Multiphysics modeling of continuous casting of stainless steel. *Journal of Materials Processing Technology*, 278, 2020.

[108] M. L. S. Zappulla, L. C. Hibbeler, and B. G. Thomas. Effect of grade on thermal–mechanical behavior of steel during initial solidification. *Metallurgical and Materials Transactions A*, 48(A), 08 2017.

[109] S. Koric, B.G. Thomas, and V.R. Voller. Enhanced latent heat method to incorporate superheat effects into fixed-grid multiphysics simulations. *Numerical Heat Transfer, Part B: Fundamentals*, 57: 396–413, 2010.

[110] Michael Smith. *ABAQUS/Standard User's Manual, Version 6.9*. Dassault Systèmes Simulia Corp, United States, 2009.

[111] K. Harste. *Investigations into the Shrinkage and the Development of Mechanical Stresses During the Solidification and Subsequent Cooling of Cylindrical Blocks Made of Fe-C Alloys (in German)*. PhD thesis, Technischen Universita¨t Clausthal, 1989.

[112] J. A. Dantzig and C. L. Tucker III. *Modeling in Material Processing*. Cambridge University Press, 40 west 20th Street, New York, NY 10011-4211, USA, 2001.

[113] S.-M. Cho and B. G. Thomas. Effect of clogging on fluid flow, solidification, and defects in slab casting, 2021.

[114] C. Li and B.G. Thomas. Thermomechanical finite-element model of shell behavior in continuous casting of steel. *Metallurgical and Materials Transactions B*, 35(B), 12 2004.

[115] S. Koric and B.G. Thomas. Thermo-mechanical models of steel solidification based on two elastic visco-plastic constitutive laws. *Journal of Material Processing Technology*, 197, 12 2008.

[116] R.D. Cook, D.S. Malkus, and M.E. Plesha. *Concepts and Applications of Finite Element Analysis*. John Wiley Sons, INC, 605 Third Avenue,New York,NY 10158-0012,USA, 1989.

[117] J.H. Weiner and B.A. Boley. Elasto-plastic thermal stresses in a solidifying body. *Journal of the Mechanics and Physics of Solids*, 1, 1963.

[118] C. Koric. Solidification stress model in abaqus. *Continuous Casting Consortium Presentation*, 2004.

[119] Y. Meng and B. G. Thomas. Heat-transfer and solidification model of continuous slab casting:con1d. *Metallurgical and Materials Transactions B*, 34(B), 10 2003.

APPENDIX A

WALL FRICTION CALCULATION FOR TAPERED PIPE

Wall friction equation for a pipe with constant diameter (i.e. no tapered), discussed in fluid mechanics reference book [41], is defined as:

$$h = \frac{1}{2} f \frac{L}{D} \frac{V^2}{g} \tag{A.1}$$

where h is pressure head loss due to wall friction $[m]$, f friction factor, L pipe length $[m]$, D pipe diameter $[m]$, V fluid velocity $[\frac{m}{s}]$, and g Earth's gravitation acceleration $[\frac{m}{s^2}]$.

Now, consider a tapered pipe as shown in Figure A.1.

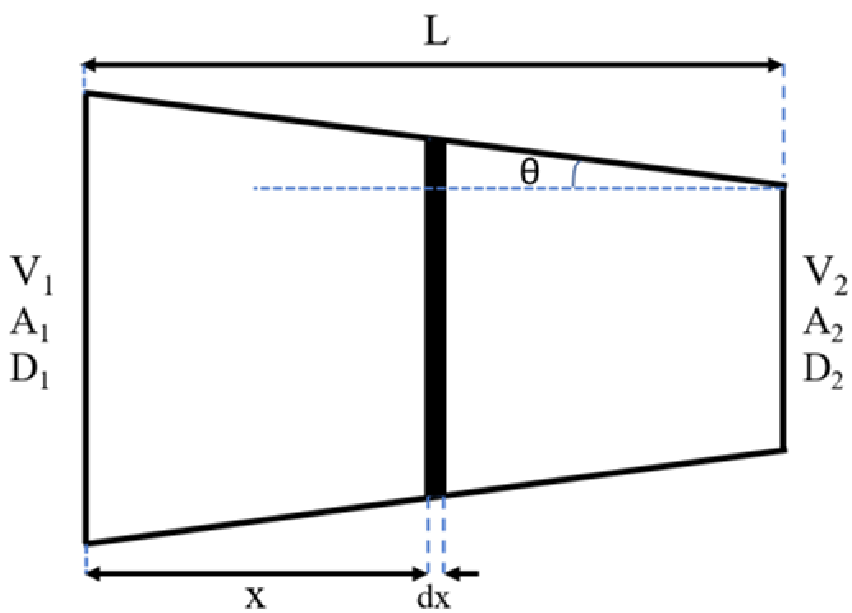

Figure A.1 Schematic of tapered length of nozzle (pipe).

For a very small portion of pipe with the length of dx, it is true to say:

$$dh = \frac{1}{2} f \frac{dx}{D} \frac{V^2}{g} \tag{A.2}$$

Consider the continuity equation:

$$V = \frac{V_1 {D_1}^2}{D^2} \tag{A.3}$$

where V_1 and D_1 are velocity and diameter of the entry section (1) $[\frac{m}{s}]$ and $[m]$, respectively.

Also from Figure A.1:

$$x = \frac{D_1 - D}{2\tan(\theta)} \tag{A.4}$$

where θ is the taper angle $[rad]$.

Therefore:

$$dx = \frac{-dD}{2\tan(\theta)} \tag{A.5}$$

Substituting Equation A.3 and Equation A.5 into Equation A.2 gives:

$$dh = \frac{1}{2}\frac{f}{g}\frac{{V_1}^2{D_1}^4}{D^5}\frac{-dD}{2\tan(\theta)} \tag{A.6}$$

Integrating Equation A.6 over the whole domain (from D_1 to D_2) and simplifying gives:

$$h = \frac{1}{16}\frac{f}{g}\frac{{V_1}^2}{{D_2}^4}\frac{({D_1}^4 - {D_2}^4)}{\tan(\theta)} \tag{A.7}$$

Insert into Figure A.1:

$$\tan(\theta) = \frac{D_1 - D_2}{2L} \tag{A.8}$$

Finally, substituting Equation A.8 into Equation A.7 gives the pressure loss in a tapered pipe due to wall friction:

$$h = \frac{1}{8}f\frac{L}{g}\frac{{V_1}^2}{{D_2}^4}(D_1 + D_2)({D_1}^2 + {D_2}^2) \tag{A.9}$$

APPENDIX B

COPYRIGHT PERMISSIONS

The article entitled: Pressure Distribution and Flow Rate Behavior in Continuous-Casting Slide-Gate Systems: PFSG [59] is reprinted with modifications in the Chapter 3 of the current thesis. Figure B.1 shows the permission obtained from the journal's web site.

SPRINGER NATURE LICENSE
TERMS AND CONDITIONS

Jun 06, 2022

This Agreement between Colorado School of Mines -- Hamed Olia ("You") and Springer Nature ("Springer Nature") consists of your license details and the terms and conditions provided by Springer Nature and Copyright Clearance Center.

License Number	5319550359141
License date	May 31, 2022
Licensed Content Publisher	Springer Nature
Licensed Content Publication	Metallurgical and Materials Transactions B
Licensed Content Title	Pressure Distribution and Flow Rate Behavior in Continuous-Casting Slide-Gate Systems: PFSG
Licensed Content Author	Hamed Olia et al
Licensed Content Date	Mar 17, 2022
Type of Use	Thesis/Dissertation
Requestor type	academic/university or research institute
Format	print and electronic
Portion	full article/chapter
Will you be translating?	no
Circulation/distribution	1 - 29

Figure B.1 Permission obtained for PFSG paper.

Furthermore, written permissions are obtained from the co-authors to include this paper in the current work (S1.PDF in the Supplementary documents).